Risk-Based Life-Cycle Cost-Benefit Analysis of Seismic Retrofitting Steel Moment-Resisting Frames in Canada using Friction Devices

by

Xiaowen Han

A Thesis Submitted in Partial Fulfillment of the
Requirements for the Degree of
Master of Engineering

in the

Department of Civil Engineering
McGill University
Montreal, Canada

Abstract

Many existing steel moment-resisting frames (MRFs) in Canada constructed between the 1960s and 1980s were not seismically designed. Friction devices have shown promise to reduce the seismic damage of early-designed steel buildings by supplementing additional force, stiffness, and energy dissipation mechanisms to resist earthquake loading. However, installing friction devices for seismic retrofitting is often subjected to limited financial resources. The seismic vulnerability of early-designed buildings in Canada's seismic zones might cause significant repair losses after future earthquakes, while the upfront retrofit cost would prevent building owners from making preventive, yet somewhat intangible, investments at present. Such a decision-making dilemma can be solved by developing a risk-based life-cycle cost-benefit (LCCB) analysis approach that assesses the economic trade-off between upfront retrofit expenses and risk-based lifetime benefits. This study conducts the LCCB analysis based on case studies to retrofit two six-story steel MRF office buildings located in Montreal and Vancouver. The steel MRFs were initially designed only for wind loads per the 1965 National Building Code of Canada (NBCC) and cannot satisfy the seismic design provisions in NBCC 2020. As such, steel MRFs are retrofitted with friction devices using the equivalent static design procedure, whereas the essential design parameters are identified and varied to cover different design scenarios. The LCCB analysis is performed for each design scenario based on a multi-step procedure consisting of seismic hazard modeling, ground motion selection, non-linear response history analyses, seismic fragility development, and life-cycle seismic loss analysis. The

life-cycle benefit from each design is quantified as the reduction in seismic losses between as-built and retrofitted buildings, from which (1) the benefit-cost ratio is computed between life-cycle benefit and upfront retrofit cost and (2) the anticipated net benefit over time is developed to pinpoint the payback year where the net present value equals zero. This study systematically compares to what extent different retrofit design parameters (e.g., brace stiffness ratio, force modification factors for ductility and overstrength) would affect the life-cycle benefit-cost performance of the steel MRFs in both Montreal and Vancouver. This study provides decision-makers with a risk-based, transparent tool to assess the economic feasibility and identify the most cost-effective solution for seismic retrofitting steel MRF buildings in eastern and western Canada.

Resumé

De nombreux cadres en acier à résistance aux moments existants (MRF) au Canada, construits entre les années 1960 et 1980, n'ont pas été conçus pour résister aux séismes. Les dispositifs de friction ont montré leur efficacité pour réduire les dommages sismiques des bâtiments en acier conçus avant cette période, en ajoutant des mécanismes supplémentaires de force, de rigidité et de dissipation d'énergie pour résister aux charges sismiques. Cependant, l'installation de dispositifs de friction pour le renforcement sismique est souvent soumise à des ressources financières limitées. La vulnérabilité sismique des bâtiments conçus avant les normes actuelles dans les zones sismiques du Canada pourrait entraîner des pertes importantes en cas de futurs tremblements de terre, tandis que le coût initial du renforcement empêche les propriétaires de bâtiments de faire des investissements préventifs, mais quelque peu intangibles, à l'heure actuelle. Ce dilemme décisionnel peut être résolu en développant une approche d'analyse coûts-avantages basée sur le cycle de vie (LCCB) qui évalue le compromis économique entre les dépenses initiales de renforcement et les bénéfices basés sur les risques à long terme. Cette étude réalise l'analyse LCCB basée sur des études de cas pour le renforcement de deux bâtiments de bureaux en acier MRF de six étages situés à Montréal et Vancouver. Les MRF en acier ont été initialement conçus uniquement pour les charges de vent selon le Code national du bâtiment du Canada (NBCC) de 1965 et ne peuvent pas satisfaire aux dispositions de conception sismique du NBCC 2020. En conséquence, les MRF en acier sont renforcés avec des dispositifs de friction en utilisant la procédure de

conception statique équivalente, tandis que les paramètres de conception essentiels sont identifiés et variés pour couvrir différents scénarios de conception. L'analyse LCCB est réalisée pour chaque scénario de conception selon une procédure en plusieurs étapes consistant en la modélisation des risques sismiques, la sélection des mouvements de terrain, des analyses de l'historique de réponse non linéaire, le développement de la fragilité sismique et l'analyse des pertes sismiques sur le cycle de vie. Le bénéfice du cycle de vie de chaque conception est quantifié comme la réduction des pertes sismiques entre les bâtiments construits et les bâtiments renforcés, à partir de laquelle (1) le ratio coûts-avantages est calculé entre le bénéfice du cycle de vie et le coût initial du renforcement et (2) le bénéfice net anticipé au fil du temps est développé pour déterminer l'année de rentabilisation où la valeur actuelle nette est égale à zéro. Cette étude compare systématiquement dans quelle mesure différents paramètres de conception de renforcement (par exemple, le ratio de rigidité des contreventements, les facteurs de modification de la force pour la ductilité et la sur-résistance) affecteraient la performance coûts-avantages du cycle de vie des MRF en acier à la fois à Montréal et à Vancouver. Cette étude fournit aux décideurs un outil transparent basé sur les risques pour évaluer la faisabilité économique et identifier la solution la plus rentable pour le renforcement sismique des bâtiments en acier MRF dans l'est et l'ouest du Canada.

Acknowledgements

I would like to extend my deepest gratitude to Prof. Yazhou Xie, my thesis supervisor, for his invaluable guidance, insightful advice, and inspiration. His dedication has fostered an enriching research environment, allowing me to thrive and explore. I am particularly grateful for our weekly meetings and his dedicated time, especially during moments of uncertainty.

Additionally, I am profoundly thankful to Oscar Galindo for his exceptional mentorship and unwavering support, which have seamlessly bridged theoretical research with real-world applications and laid a robust foundation for my future endeavors in engineering.

I also wish to express my sincere thanks to my colleague, Chunxiao Ning, for his generous assistance with the seismic disaggregation results.

I sincerely appreciate my parents and fiancé for their encouragement and support, which have been constant sources of strength and motivation. Their belief in me has been a driving force behind my accomplishments. Lastly, I would like to thank all my friends and colleagues at McGill University for their steadfast support and companionship throughout this journey.

Table of Contents

List of Tables

List of Figures

List of Acronyms

ASD	allowable stress design
BCPI	Building construction price index
BCR	benefit-cost ratio
BRC	building replacement cost
BSA	backtracking search algorithm
CAS	casualties
CD	contents damage ratio
CISC	Canadian Institute of Steel Construction
CJP	complete joint penetration
CMS	conditional mean spectrum
CON	contents losses
CPI	Consumer price index
CRSP	Commercial rent services price index
CRV	contents replacement value
CSRN	Canadian Seismic Research Network
DC	distribution cost
DC	distribution cost
DCR	demand to yielding capacity ratio
DS	damage state
EAL	expected annual losses
ESFP	equivalent static force procedure
FA	floor area
FEMA	Federal Emergency Management Agency
FMC	flexible moment connection
FO	percentage of floor area occupied by the owner
GA	genetic algorithm
IDR	inter-story drift ratio
IM	intensity measure
INC	income losses
INCM	business income
LCCB	life-cycle cost-benefit
LFRS	lateral force resisting system
LRFD	load-and-resistance-factor design
MRF	moment-resisting frame
MSC	Monte Carlo simulation
NBCC	National Building Code of Canada
NPV	net present value
NSA	non-structural acceleration-sensitive repair cost
NSD	non-structural drift-sensitive repair cost
PBEE	performance-based earthquake engineering
PFA	peak floor acceleration
PPER	Pacific Earthquake Research Center

PSDA	probabilistic seismic demand analysis
PSDM	probabilistic seismic demand model
RBS	reduced beam section
REL	relocation expenses
RENT	rental cost
RET	rental income losses
RT	recovery time
Sa	spectral accelerations
SGA	search group algorithm
SHM6	6th generation seismic hazard model
STR	structural repair cost
UHS	uniform hazard spectrum
WFP	welded flange plate
WQSZ	Western Quebec Seismic Zone

Chapter 1. Introduction

1.1. Problem Definition and Research Motivation

Many steel moment-resisting frame (MRF) structures in Canada were built prior to the incorporation of seismic design provisions. The lateral force resisting system (LFRS) of these buildings was predominately designed to resist wind loads, as the building codes imposed a larger design base shear induced by wind loads compared to earthquake forces (Gómez et al., 2015). Traditionally, steel structures are presumed to possess sufficient capability to withstand seismic events due to their ductile properties, energy dissipation potential, and high strength-to-weight ratio (Anastasiadis, 2024; Biddah & Heidebrecht, 1999). However, the structural failures observed after the 1994 Northridge and 1995 Kobe earthquakes have exposed their seismic vulnerability (Mahin, 1998; Nakashima et al., 1998; Tremblay et al., 1996). Many steel MRFs suffered extensive damage in the aftermath of these seismic events. In 2008, the Canadian Seismic Research Network (CSRN) was established with the objective of conducting research aimed at mitigating seismic risks of a large inventory of deficient structures in major urban centers in Canada. Within the steel structure division of the CSRN, the research activities were centered around the seismic assessment of concentrically braced frames and steel MRFs with semi-rigid beam-column connections that were constructed in Canada during the period from 1960 to 1990 (Tremblay, 2015). This era represents a time before the implementation of seismic design requirements. Several large-scale experimental programs were conducted to gather data on the cyclic inelastic response of critical members and connections in these steel framing systems (Balazadeh-Minouei et al., 2018; Kyriakopoulos & Christopoulos, 2013; Massarelli, 2010; Yan & Tremblay, 2012).

Steel MRFs with semi-rigid connections were found to experience excessive story drifts and rotation demands in their connections under seismic loading. The studies concluded that the steel buildings constructed in seismic active regions of Canada before 1990 generally lack sufficient lateral resistance compared to the minimum seismic load requirements specified in current codes.

Recognizing the seismic vulnerabilities inherent in out-of-code steel buildings and the potentially severe social and economic consequences of future seismic events, the owners of the buildings, particularly those located in seismically active and densely populated regions, require earthquake retrofit solutions capable of ensuring the required safety level and minimizing earthquake-induced loss. Among various seismic protective techniques, friction devices have emerged as a highly favored option for the seismic retrofit of steel structures due to their simplicity and reliability (Jaisee et al., 2021). The friction damper bracing system provides supplemental mechanical damping through sliding friction and additional stiffness from the connecting steel bracing. As seismic activity commences and buildings experience deformations, the friction dampers are triggered and start sliding to dissipate seismic energy by generating rectangular hysteretic loops. The effectiveness of seismic retrofit using fiction devices depends on several factors, including the mechanical parameters of the devices, the dynamic properties of the buildings, and the nature of seismic hazards. Earlier studies have been centered around the optimization of damper slip load to dissipate the maximum amount of energy or achieve the optimal seismic control using a deterministic approach (Filiatrault & Cherry, 1990; Moreschi & Singh, 2003; Nabid et al., 2018). The seismic performances of retrofitted buildings with various design parameters, including slip loads, bracing, and locations, were analyzed using a design spectrum or a limited number of earthquake ground motions. However, the drawback of such a deterministic approach is evident: it fails to incorporate the uncertainties associated with structural properties and seismic excitation into the design process. Consequently, recent studies have shifted their focus toward optimization methodologies that account for the inherent variability in structures and ground motions, thereby enhancing the robustness and reliability of seismic retrofit designs (Miguel et al., 2014, 2016a; Ontiveros-Pérez et al., 2019).

While numerous studies show promise of mitigating seismic responses of existing steel buildings using friction devices, many owners and stakeholders exhibit reluctance to adopt such measures. This reluctance is often attributed to the perceived excessive retrofit cost, which creates a significant financial burden (Egbelakin et al., 2014). Given the limited monetary resources and the pursuit of profit-making, owners often lack incentives to make initial investments in seismic retrofitting if the long-term benefits cannot be quantified and justified in monetary values. As such, the owners are confronted with a complex decision dilemma: whether to retain the old building as is, risking greater future losses, or to invest in retrofitting with initial upfront costs, leading to significantly reduced future expenses (Nuti & Vanzi, 2003). To address such a dilemma, a risk-based approach for evaluating and comparing the cost-effectiveness of retrofitting strategies becomes necessary (Padgett et al., 2010). The benefits of seismic upgrades can be quantified by comparing the seismic life-cycle costs and conducting a cost-benefit analysis between original and retrofitted structures. The emphasis on lifetime performance and benefits, rather than focusing solely on initial retrofit costs, facilitates risk-enabled investment decisions and maximizes net gains in dollar values. The performance-based earthquake engineering (PBEE) framework proposed by the Pacific Earthquake Research Center (PEER), along with the HAZUS program developed by the Federal Emergency Management Agency (FEMA), provides a feasible pathway for conducting life-cycle cost-benefit analyses of seismic retrofits in a fully probabilistic manner (FEMA, 2012; Günay & Mosalam, 2013; Moehle & Deierlein, 2004; Porter, 2003).

While such life-cycle cost-benefit assessments have been conducted on various structures in the US and globally (NourEldin et al., 2019; Padgett et al., 2010; Vitiello et al., 2017; Zhang et al., 2022), they remain largely unexplored for building structures in Canada. Previous seismic retrofit studies in Canada have predominantly concentrated on enhancing specific seismic responses without considering structures' lifetime performance. In response to these research gaps, this thesis deals with representative non-seismically designed steel structures in Canada and investigates the efficacy of seismic retrofitting measures through friction device-based bracing systems. A risk-based approach is presented to compare the upfront costs with the long-term monetary benefits of seismic retrofits under various design scenarios. This is achieved by devising a multi-step analysis framework that explicitly incorporates the probabilistic seismic hazard model, selects spectrum-matching ground motions, conducts numerical simulations and nonlinear response history analyses of benchmarked steel MRFs, fragility assessment of existing and retrofitted buildings, as well as the associated loss assessment for both structural and non-structural components under various seismic damage states.

1.2. Thesis Organization

The research is organized into subsequent eight chapters:

Chapter 2 provides a literature review on steel MRFs in Canada, seismic retrofit measures, and introduces the risk-based seismic life-cycle cost-benefit analysis framework.

Chapter 3 details the benchmark 1960s buildings, and related design processes and numerical modelling.

Chapter 4 introduces a displacement-based seismic retrofit design method concerning friction dampers and their connecting diagonal braces.

Chapter 5 conducts seismic hazard analysis and describes the steps in ground motion selection.

Chapter 6 performs nonlinear time history analyses and compares the responses of the pre-code and retrofitted buildings.

Chapter 7 develops seismic demand models and conducts seismic fragility assessment.

Chapter 8 conducts the life cycle cost-benefit analysis against friction dampers under various design scenarios.

Chapter 9 presents the conclusions drawn from the current research and recommendations for future works.

Chapter 2. Literature Review

2.1. Seismic Vulnerabilities of Early-Designed Steel Buildings in Canada

2.1.1. Historical Seismic Performances of Steel Moment-Resisting Frames and their Implication on Canadian Structures

Steel MRFs have been widely adopted as structural systems in buildings for over a century (Geschwindner & Disque, 2005). Steel structures are known for their high ductility capacity and exceptional strength-to-weight ratio, which theoretically, by nature, makes them one of the most effective earthquake-resistant structural systems against strong seismic events (Anastasiadis, 2024). However, the instances of failures occurring over the past four decades due to strong earthquakes indicate that relying solely on these characteristics may not always guarantee structural integrity. In contrast, the 1994 Northridge earthquake in the United States, the 1995 Kobe earthquake in Japan, and the 2010 and 2011 Christchurch earthquakes in New Zealand were pivotal historical events that contributed to the understanding of the seismic performance of steel building structures. These events also significantly influenced seismic design practices of modern steel building structures.

On January 17, 1994, an earthquake with a moment magnitude of 6.7 struck near Northridge, approximately 30 km northwest of downtown Los Angeles. This seismic event caused extensive damage to over 40,000 buildings, claimed 57 lives and over 10,000 injuries, and inflicted $20 billion in property damage, positioning it as the largest earthquake disaster in U.S. history (Tierney, 1997). Particularly, more than 150 steel MRFs, ranging from short to tall structures and comprising both new and old constructions, experienced widespread brittle damage. Figure 2-1 (a) depicts the typical flange welded-web bolted with shear tab connection of the steel frames, where the failure predominantly occurs at the beam-column joint region, particularly at the bottom flanges as shown in Figure 2-1 (b) and (c). Such a connection was extensively utilized in the US prior to the Northridge earthquake in 1994, and it was subsequently termed the pre-Northridge connection. Before the Northridge earthquake, steel frame buildings with pre-Northridge connections were expected to develop ductility through the yielding in beam-column assemblies and dissipate earthquake energy via plastic rotations within the beams and at their connections to columns (William McGuire, 1988). It was widely believed that the connections had adequate ductility capacity to withstand high seismic forces. Therefore, the occurrence of brittle damage in the connection, contrary to the intended behavior, came as a great surprise to the structural engineering community in the United States (Hamburger & Malley, 2019).

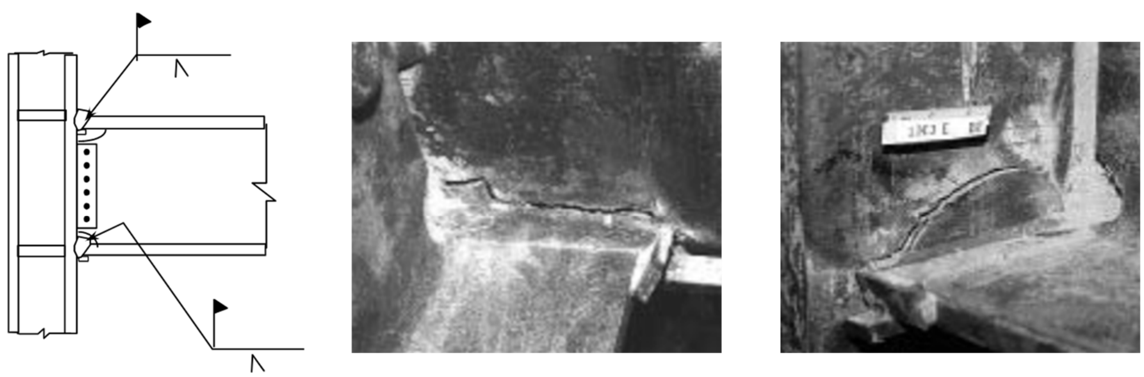

(a) (b) (c)

Figure 2-1 (a) Typical pre-Northridge connection and (b & c) its failure in the Northridge earthquake (Reis & Bonowitz, 2000; Roeder, 2000)

As the structural engineering community continued to scrutinize the design process of the pre-Northridge connection, another damaging earthquake with a moment magnitude of 6.9 hit Kobe City, Japan, on January 17, 1995. The epicenter of the earthquake was located on Awaji Island, approximately 20 km from the city of Kobe. This earthquake resulted in 6,433 deaths, injured over 27,000 individuals, and caused over $100 billion in damages (Horwich, 2000). In Japan, steel is the second most used construction material after wood (Nakashima et al., 1998). It was surprising to observe the same brittle damage at the beam-column connection in steel structures, resembling those during the Northridge earthquake. As shown in Figure 2-2, despite differences in the beam-column joint configurations between U.S. and Japanese practices, the failure modes at the welds, heat-affected zone, and base material fracture remain consistent.

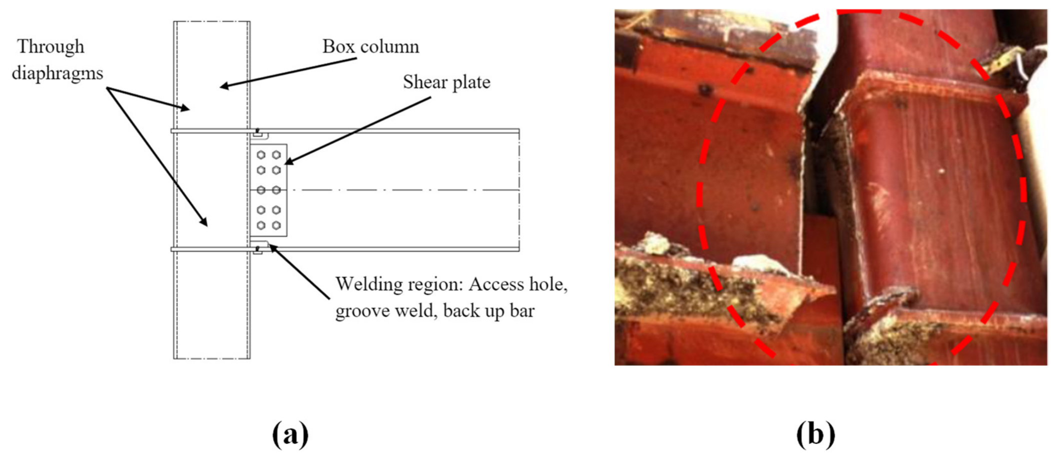

Figure 2-2 (a)Typical connection in Japan and (b) its failure in the Kobe earthquake (Reis & Bonowitz, 2000; Roeder, 2000)

The repeatability of damage witnessed during both Northridge and Kobe earthquakes highlighted the seismic vulnerability of welded beam-column connections in steel MRFs. In response to the alarming seismic performance of related buildings, the SAC Joint Venture was established with the objective of developing reliable, practical, and cost-effective guidelines and standards of practice for (1) repairing or upgrading damaged steel moment frame buildings, (2) designing new steel buildings, and (3) identifying and rehabilitating at-risk steel buildings (Ross, 1995). Upon investigation, the brittle failure was found to be caused by the mechanical properties of materials, poor workmanship, and inadequate construction practices related to configuration, detailing, welding, and design. To address those issues, updates were made to the design practices to ensure a safer connection. These updates included promoting proper detailing practices, improving steel material strength regulations, considering triaxial loading at moment-resisting connections in the design process, and introducing new design details such as reduced beam sections (Bruneau et al., 2005; Popov et al., 1998; Tsai et al., 1995).

Canadian researchers related the observations and lessons of the two earthquakes to the seismic design provisions in the Canadian building code and standards for steel structures (Tremblay et al., 1995, 1996). They have identified several issues that were not adequately addressed in the Canadian codes and standards at that time. To deal with these issues, their recommendations for the seismic design of steel MRFs include: 1. Adopt a capacity design approach for the entire lateral load-resisting system of the structure for all categories of steel MRFs. 2. Factor in the reduced redundancy observed in steel MRFs with only a few moment-resisting bays. 3. Minimize structural irregularities and extend the use of redundant, ductile detailing in design (Tremblay et al., 1995). In the years following the SAC Joint Venture project, both the National Building Code of Canada (NBCC) and the Canadian Standard Association (CSA) have updated their design standards to enhance the seismic safety of new steel structures. Furthermore, the fact that a large number of existing steel structures are situated in high seismic regions in Canada called for immediate attention to seismically retrofit these structures.

2.1.2. Non-seismically Designed Steel Moment-Resisting Frames in Canada

The Canadian economic boom after World War II marked a period of significant prosperity. During the eight years from 1946 to 1953, the population increased by 3.1 million and new investment in fixed capital exceeded 20% of the Gross National Product (Gibson, 1954). This substantial influx of residents and capital fueled strong growth and expansion of the construction sector in Canada. Figure 2-3 illustrates the trajectory of new construction expenditures, value of building permits, and structural steel production in Canada between 1920 and 1980. It shows a surge in construction activity starting from the mid-1940s. The most substantial increase is observed between the 1960s and late 1970s, aligning with the exponential growth of structural steel production in Canada during that period. While precise statistics regarding steel buildings in Canada are not available, it can be logically deduced from the above observation that a considerable number of steel MRFs were erected between 1960 and 1980. In Canada, seismic loads were introduced into building codes as early as 1941 (Mitchell et al., 2010). However, during the design of the LFRS, the base shear resulting from wind loads typically exceeded that from seismic loads (Gómez, 2014). Additionally, seismic design provisions were not incorporated into CSA S16 until 1989, making seismic design a rare practice during this period. As such, there exists a potential need for seismic retrofit of a typical 1960s non-seismically designed steel MRF in Canada. This structure is benchmarked to serves as a representative example of the numerous steel buildings constructed during the Canadian building boom.

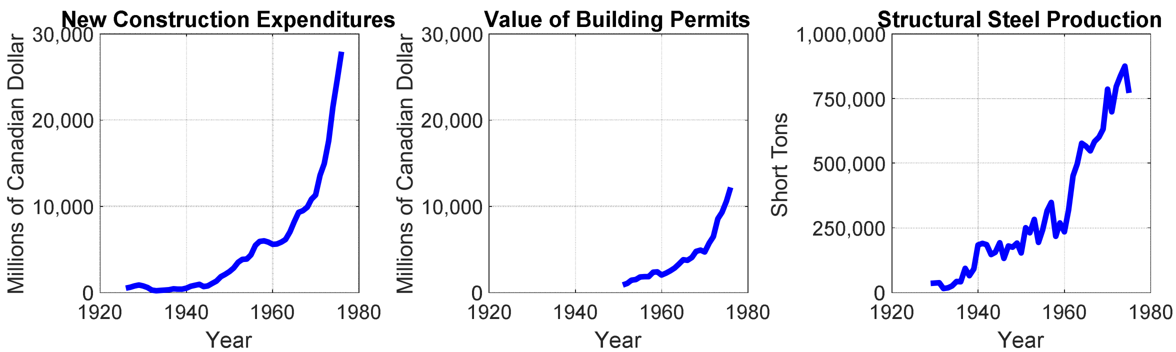

Figure 2-3 Trend of new construction expenditures, the value of building permits, and structural steel production in Canada between 1920 and 1980 (Statistics Canada, 2023)

The NBCC 1965 defined three types of constructions characterized by different levels of assumed rigidity in the beam design:

Type 1: Rigid-frame Construction. It assumes that structural members are generally continuous over supports, and that beam-to-column connections possess sufficient rigidity to maintain the original angles between intersecting members.

Type 2: Simple Construction. It assumes that the ends of beams and girders are connected solely for shear purposes and are allowed to rotate freely under load in the plane of loading.

Type 3: Semi-rigid Construction. It assumes that the connections of beams and girders are partially restrained against moment rotation, and these connections possess a reliable and predetermined moment capacity that lies between the complete rigidity assumed in rigid-frame construction and the complete flexibility assumed in simple construction.

The Type 2 construction was the design philosophy widely adopted in the 1960s (Gómez et al., 2015; Kyriakopoulos & Christopoulos, 2013; National Research Council of Canada, 1967), and it is further subject to the following provisions:

1. The connections and connected members must possess adequate capacity to withstand wind moments.
2. The girders must be able to carry the entire gravity load as simple beams.
3. Connections should exhibit sufficient inelastic rotation capacity to prevent overstressing of fasteners or welds under combined gravity and wind loads.

In the design of beam-column moment-resisting connections under Type 2 Construction, two forms of connection are suggested: the welded flange plate (WFP) connection and the typical pre-Northridge connection. Based on an interview with a senior engineer in Canada, Canadian engineers were more conservative and relied less on welding materials compared to the U.S. (Gómez, 2014). Consequently, while pre-Northridge connections were prevalent in the U.S. during that period, WFP connections were more commonly used in Canada. A schematic of the WFP connection is shown in Figure 2-4.

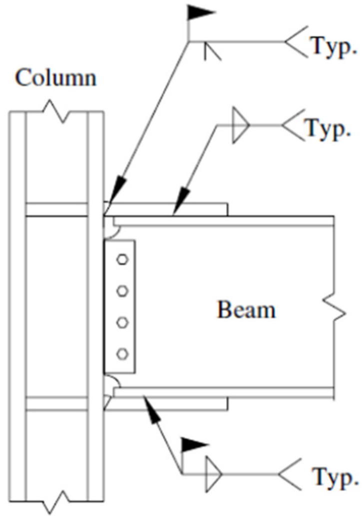

Figure 2-4 Typical wielded flange plate connection (Gómez, 2014)

The WFP connections were designed with the flexible moment connection (FMC) approach. This approach, dating back to the 1910s and authorized in the U.S. and globally, involves treating beams as simply supported members under gravity loads and as moment-connected members under lateral loads. Often termed “Type 2 with Wind”, this historical method has been extensively employed in numerous building designs (Geschwindner & Disque, 2005). In the design process of Type 2 with Wind connections, the beam is assumed symmetrical, uniformly loaded, connected to rigid supports, and behaves elastically. A relationship between the beam moment and rotation is established through the use of a classic slope deflection equation, forming what is known as a “beam line” as shown in Figure 2-5. Following this, a parabolic relationship between the connection moment and rotation is superimposed onto the beam line, where the connection reaches its plastic moment capacity and continues to maintain that level of the moment while undergoing plastic deformations. When considering only gravity load, equilibrium occurs at the intersection of these two lines. Upon the addition of lateral load, the windward connection unloads, resulting in a reduction of the moment in the connection as rotation decreases. Conversely, for the leeward connection, the moment increases as rotation increases. Further details and calculations are presented in previous studies (Geschwindner & Disque, 2005).

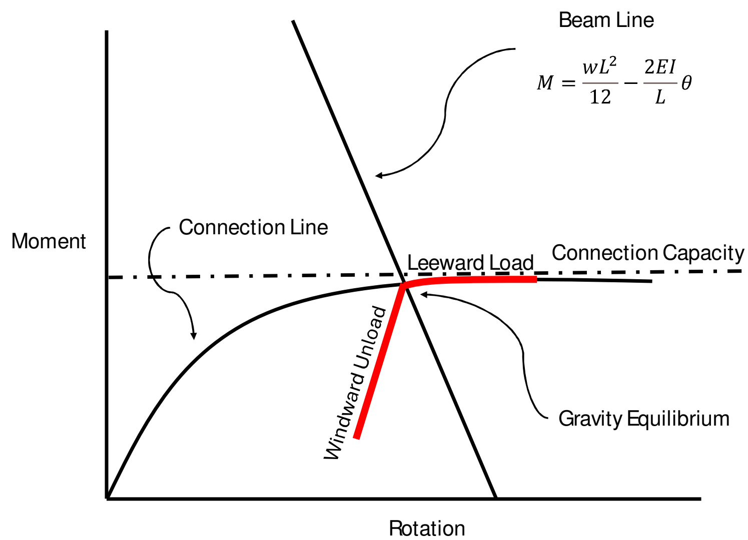

Figure 2-5 Behavior of a partially restrained connection under load

Type 2 with Wind connections were only designed to withstand wind loads without considering the combination with gravity force, resulting in a design for significantly lower demands compared to current seismic design codes. In this system, connections were pushed further into their plastic regime when subjected to lateral wind loading and were mandated to possess sufficient inherent ductility. However, the welding properties and construction craftsmanship during the 1960s were inadequate to ensure the designed inelastic capacity. Consequently, it is foreseeable that these connections may exhibit earlier yielding behavior compared to the beams under earthquake loads. One such example is shown in Figure 2-6, a Type 2 with Wind WFP connection has failed in the 2010 Chile earthquake. On the left-hand side, the weld joining the beam to the bottom cover plate has fractured entirely. This failure indicates that the structural detailing fell short of meeting the design demand for the plastic moment capacity, leading to excessive damage to buildings under earthquake loads.

Figure 2-6 Failure of Type 2 with Wind WFP connection in Chile Earthquake 2010 (Kyriakopoulos, 2012)

Kyriakopoulos (2012) conducted a comprehensive study on Type 2 with Wind connection through an experimental program that involved two typical connections extracted from a Type 2 Construction steel MRF of an existing hospital building in Quebec. These connections comprised one with an inclined top cover plate and another with a bent top cover plate. Both connections initially behaved in a ductile manner until reaching a connection rotation of approximately 0.02 radians or 2.6% column drift. At this point, the connection with the top cover plate failed in tension in a brittle manner at the interface of the plate and the complete joint penetration (CJP) groove weld connecting it to the column. On the other hand, the connection with the bent top cover plate, reinforced with small tack welds, exhibited additional resistance and endured a few more cycles before a tension failure at around 2.9% column drift. The failure occurred at the interface of the plate and the CJP weld and at the location of the apex of plate buckling. As the column drift increased, the top flange of the beam began to bear on the continuity plates of the column, and the shear tab buckled due to excessive deformation in the top cover plate when subjected to compression. The connection with the top cover plate eventually failed when the column drift reached 4%.

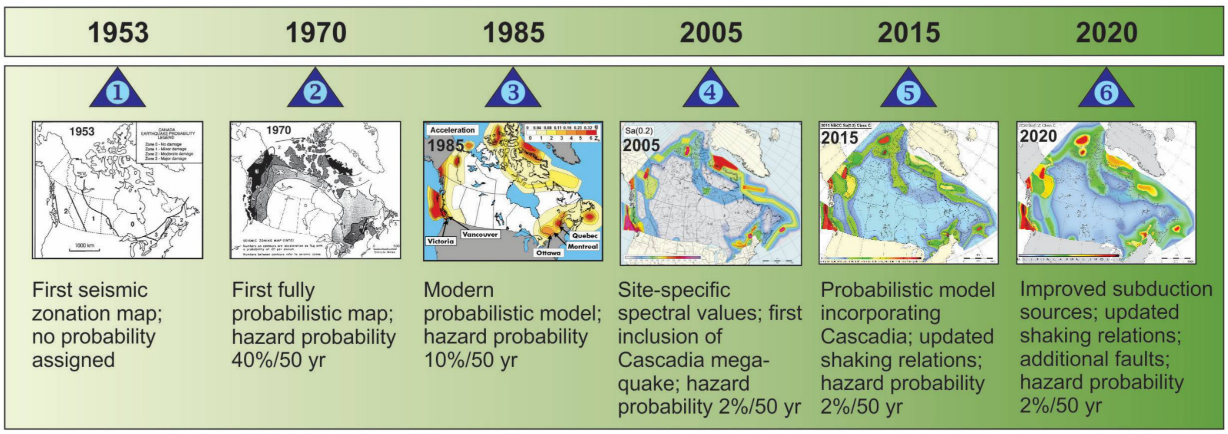

Figure 2-7 Six generations of seismic hazard models for Canada (Kolaj et al., 2020b)

Analysis of the design philosophy, coupled with observations from past seismic performance and experimental testing, proves the seismic vulnerability inherent in older steel buildings across Canada. Additionally, the evolution of the seismic hazard models, illustrated in Figure 2-7, emphasizes the updated knowledge on the substantially increased seismicity in densely populated regions. Consequently, effective retrofit measures are necessary to enhance the seismic performance of existing Type 2 Construction steel MFR buildings.

2.2. Seismic Retrofits Using Friction Devices

2.2.1. Damper Devices

In the pursuit of mitigating seismic responses of the buildings and preventing structural collapse, one of the most practical engineering solutions involves the installation of seismic energy dissipation devices (Priya et al., 2014; Soong & Spencer, 2002; Symans et al., 2008). Seismic energy dissipation devices fall into three main categories: passive, active, and semi-active. Apart from passive options, all other alternatives are predominantly technology-intensive and rely on external energy sources, such dependency makes them less favorable (Almajhali, 2023; Kerboua et al., 2014). Of those passive energy dissipation devices, hysteretic dampers, which dissipate energy through hysteretic behavior, are highly favored for their simplicity and reliability (De Domenico et al., 2019; Jaisee et al., 2021; Javanmardi et al., 2020; Shu et al., 2022). These devices include friction dampers, viscous fluid dampers, and viscoelastic dampers.

Friction dampers were initially developed by Canadian researchers in 1980, inspired by the analogy of automotive braking (Pall et al., 1980). During seismic events, these dampers start slipping prior to the yielding of the main structure and dissipating seismic energy by mechanical damping through sliding friction. Using the Lagrangian method, the equation governing the dynamic motion of a structure equipped with friction dampers can be expressed as follows (Armali et al., 2019; Min et al., 2010):

$$M\ddot{u}(t) + C\dot{u}(t) + \left[Ku(t) + k_0\Delta_y h(t)\right] = -M\ddot{u}_g(t) \qquad \text{2-1}$$

where M is the mass, C is the damping coefficient, K is the stiffness, k_0 is the stiffness of the damper bracing system, Δ_y is the displacement of the damper brace system, $h(t)$ is the hysteretic variable for the friction damper, u is the acceleration, $\dot{u}$ is the velocity, u is the displacement, and $\ddot{u}_g$ is the ground acceleration.

Fluid viscous dampers function by compelling a viscous fluid through orifices situated in and around a piston head as the structure oscillates. This movement of fluid generates heat, thereby dissipating seismic energy effectively in earthquake scenarios. The fluid viscous device possesses a velocity-dependent component and no apparent stiffness, as shown in its constitutive equation (De Domenico & Ricciardi, 2019; Xie & Zhang, 2017).

$$F = C_v \cdot \mathrm{sgn}[\dot{u}(t)] \cdot |\dot{u}(t)|^{\alpha} \qquad \text{2-2}$$

where $\mathrm{sgn}[\dot{u}(t)]$ is the signum function to damper velocity $\dot{u}(t)$, C_v is the viscous coefficient, and α is the velocity exponent, which controls the nonlinearity of fluid viscous damper. Nonlinear fluid viscous devices, with an α less than 1.0, have a greater energy dissipation potential than linear devices.

Viscoelastic dampers used in structural applications typically consist of copolymers or glassy substances and they are capable of dissipating energy through shear deformation (Aye et al., 2014). These dampers provide a resisting force that is proportional to displacement $u(t)$ and velocity $\dot{u}(t)$, and it has a stiffness component k, as shown in the equation (Whittle et al., 2010).

$$F = ku(t) + C_v \cdot \mathrm{sgn}[\dot{u}(t)] \cdot |\dot{u}(t)|^{\alpha} \qquad \text{2-3}$$

Figure 2-8 illustrates the schematic and force-displacement curves for three types of hysteretic devices. Among these, friction dampers stand out as the most preferable because they dissipate maximum energy due to the generation of the rectangular hysteretic loop (Pasquin et al., 2004; Roh et al., 2018). Furthermore, their performance is unaffected by ambient temperature variation, leakage, and deterioration over time, as well as amplitude, frequency, and number of cycles. However, one major drawback with friction dampers is their inability to re-center, which can result in permanent deformation in the structure. In contrast, viscoelastic dampers possess a restoring ability and activate at low displacements. Concerns regarding residual deformation following strong ground motion have prompted numerous studies on the self-centering capability of energy dissipation devices (Latour et al., 2019; Veismoradi et al., 2021; Wang et al., 2020; Westenenk et al., 2019; Xu et al., 2018; Zhu & Zhang, 2008). Nevertheless, the introduction of springs for self-centering in friction dampers, according to (Pall et al., 1980), adversely affects the damper's hysteretic loop, leading to reduced energy dissipation capability. Consequently, this necessitates the application of more devices to achieve the required energy dissipation, making self-centering friction dampers less efficient compared to non-self-centering devices.

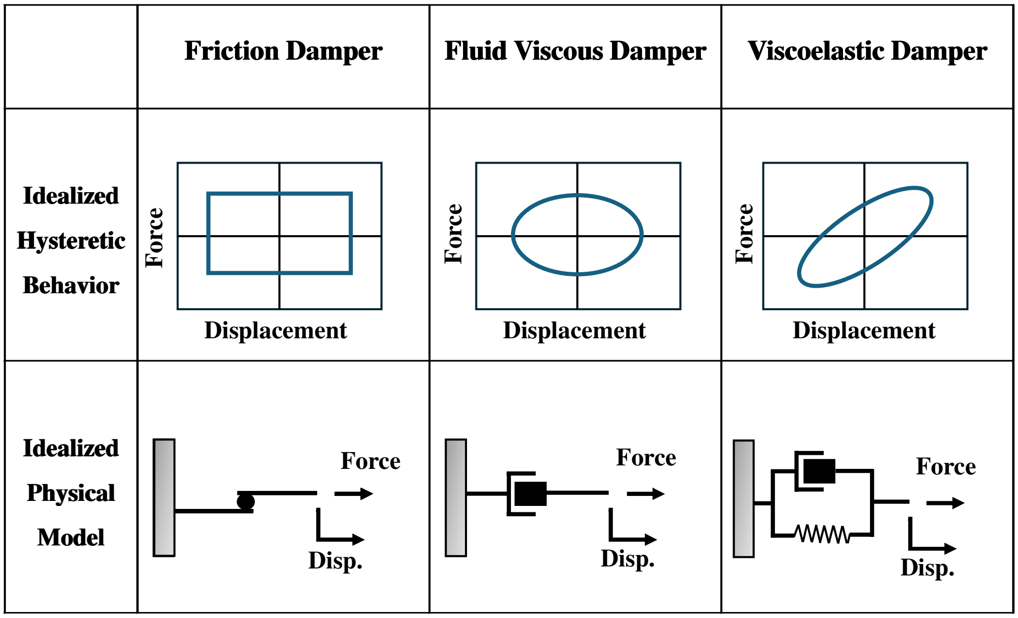

Figure 2-8 Schematic and force-displacement curves for friction damper, fluid viscous damper, and viscoelastic damper

Friction devices have been extensively tested on shake tables in both Canada and the United States (Pasquin et al., 2004). A three-story frame equipped with friction dampers was tested at the University of British Columbia, Vancouver (Filiatrault & Cherry, 1987). Remarkably, the friction-damped frame showed no signs of damage even when subjected to an earthquake record with a peak acceleration of 0.9g. Similarly, another nine-story three-bay frame equipped with friction dampers underwent testing at the Earthquake Engineering Research Center of the University of California, Berkeley (Aiken et al., 1988). Despite reaching an acceleration of 0.84g, all components of the friction-damped frame remained elastic. These shake table tests demonstrate the effectiveness of friction dampers as a reliable seismic retrofitting measure.

2.2.2. Design, Optimization, and Real-world Applications of Friction Devices

While friction devices hold the promise of mitigating the seismic risk of structures, their effectiveness hinges on the proper design of parameters and configurations (Constantinou et al., 2007). Moreover, to maximize the mitigation effectiveness of friction devices, optimization is necessary for identifying optimal design parameters regarding, e.g., damper slip loads, the number of dampers, and their positioning within the structure (Jaisee et al., 2021).

Early research on optimizing the design procedure was conducted by Filiatrault and Cherry (1990), focusing on determining the optimal slip load for friction dampers. In particular, the total energy dissipated through friction devices depends on the slip load and slip distance. When the slip load is high, there is no slippage, resembling a conventional braced frame. Conversely, with a low slip load, energy dissipation might become insignificant. Hence, it is essential to tune a friction damper between these two extremes to find a slip load for optimal structural response control. Filiatrault and Cherry (1990) introduced the concept of optimum slip load, such that an intermediate slip load zone exists that maximizes the seismic energy dissipation.

Many studies have been carried out to determine the optimal slip load. Patro and Sinha (2010) investigated optimizing friction dampers by employing a constant slip load distribution pattern. They concluded that the optimum slip load of a friction damper is influenced by the characteristics of ground motion rather than the properties inherent to the structure. Moreover, various optimization strategies have been explored in the optimization process, including the genetic algorithm (GA) (Miguel et al., 2014; Moreschi

& Singh, 2003) and the backtracking search algorithm (BSA) (Miguel et al., 2016b, 2016a). These studies consider linear elastic responses simulated through an equivalent single-degree-of-freedom system. The slip loads are varied at the base while maintaining a fixed vertical distribution, and the seismic performances of the structure are then evaluated against indices combining maximum inter-story drift, dissipated energy, and base shear. The optimization methods generally require complex mathematical calculations. In contrast, Nabid et al. (2018) proposed a low-cost performance-based optimization approach, incorporating the uniform damage distribution concept. Overall, numerous studies have been dedicated to achieving the common objective of optimizing the design of friction dampers to make them more effective in mitigating the seismic responses of structures (Lee et al., 2008; Miguel et al., 2015, 2018; Moghaddam et al., 2022; Taiyari et al., 2019; Weber et al., 2010).

However, it is essential to recognize the significance of uncertainties related to structural properties and seismic excitations during the optimization process of friction devices. Several studies have incorporated these uncertainties for damper optimization. Miguel et al. (2014) introduced a pioneering study on robust design optimization for friction dampers; their approach aimed to simultaneously minimize the mean and variance of the maximum displacement associated with a six-story building equipped with friction devices. Monte Carlo simulation (MSC) was utilized to quantify the stochastic response data. Results indicated a substantial reduction in both the mean value (70%) and variance (99%) of the maximum displacement, demonstrating the effectiveness of the optimization procedure. Additionally, Miguel et al. (2016a) proposed a robust optimization framework for friction dampers to minimize the probability of building failure. This study accounted for uncertainties related to structural attributes and ground motions. The authors analyzed a three-bay ten-story building structure with BSA, considering parameters such as friction force and damper positioning in response to seismic activity. The optimization strategy successfully reduced the building failure probability, inter-story drift, and response variances by 99%, 70%, and 97%, respectively, with the installation of three dampers. Later, Ontiveros-Pérez et al. (2019) devised a streamlined approach for concurrently optimizing the friction force and optimal placement of friction dampers within a building structure, considering the uncertainties of seismic excitations and the nonlinear behaviors of the dampers. This methodology was developed through the reliability-based optimization design to minimize the probability of failure. The authors employed a novel meta-heuristic technique known as the search group algorithm (SGA) for the optimization process. Essentially, SGA explores promising regions within the search domain and refines its search based on past results to identify the optimal design. The authors determined the optimum slip loads and positions of friction dampers.

In practice, there have been successful applications of friction dampers in both new constructions and existing buildings across Canada and internationally (Avtar Pall & Rashmi Pall, 1996). Figure 2-9 illustrates various applications of friction devices in different types of buildings in different countries.

Figure 2-9 Examples of buildings with installation of friction dampers (Quaketek, 2023)

2.3. Economic Challenges for Seismic Retrofitting Existing Buildings

Building owners frequently exhibit reluctance towards installing seismic mitigation measures, despite the evident seismic vulnerabilities of their buildings and the proven effectiveness of seismic protective devices (Egbelakin et al., 2011; Solberg et al., 2010). Previous research examining the economic impediments hindering seismic retrofitting of earthquake-prone buildings has revealed several related obstacles to seismic risk mitigation decisions. These barriers include perceptions regarding the financial commitments associated with retrofitting, the variability in the actual costs of retrofitting, and the expenses related to insurance premiums (Egbelakin et al., 2014).

The financial implications of seismic retrofitting act as a considerable driving force influencing mitigation decisions. Interviews conducted with building owners have uncovered a common misconception regarding the relationship between higher seismic strength and retrofit costs, with many erroneously believing that doubling a building's seismic strength results in a doubling of retrofit costs (Egbelakin et al., 2014). The high cost of retrofitting stands as a significant barrier to adopting seismic retrofitting. Additionally, these costs exhibit considerable variability, making accurate cost estimation challenging. These variabilities are influenced by factors such as location, type of structure, building characteristics, rehabilitation approach, desired performance level, and additional works related to provisions in the building codes (Baker & Cornell, 2008). The estimation process for seismic retrofit costs is further complicated by both direct costs (including seismic and non-seismic retrofit construction expenses) and indirect costs (such as those stemming from business disruption and loss of revenue) (Bradley et al., 2009). The inability to accurately estimate the total retrofitting costs becomes another significant barrier to making informed seismic retrofit decisions.

An additional obstacle to seismic retrofitting is that insurance premiums do not accurately reflect the seismic mitigation actions undertaken in a retrofitted earthquake-prone building. Building owners commonly rely on earthquake insurance as a risk management tool (Spence & Coburn, 2008). However, insurance premiums are not calculated based on a risk-based analysis and fail to account for the reduction in risk through retrofitting. Therefore, the building owners who retrofitted their structures were unable to secure a policy that reflected the level of risks posed by their buildings. In essence, the absence of a corresponding lower cost in insurance premiums undermines the incentive for seismic retrofitting.

In conclusion, the inability to accurately quantify the costs and benefits of seismic retrofits has been a significant deterrent for building owners considering such investments. A critical aspect of this issue is the difficulty in assessing the risk reduction benefits over the life-cycle of the retrofit. A building level risk-based earthquake loss assessment can be undertaken by integrating site seismic hazard, building vulnerability, and the consequences of failure/damage (Tesfamariam & Saatcioglu, 2008). However, uncertainties are inherent at every stage of the procedure (Choun & Elnashai, 2010): 1. Uncertainty in a seismic hazard arises from the identification of earthquake sources, the modeling of earthquake occurrence, and the estimation of attenuation. This uncertainty is epistemic, as it can be mitigated through the collection of additional data and the enhancement of theories regarding earthquake processes. 2. The building vulnerability model can be developed based on empirical data, experimental tests, analytical, or expert judgment. Each of these methods involves inherent uncertainties in both the assessment procedures and the data used. These uncertainties include measurement uncertainty related to the observations, variability in ground motions, statistical uncertainty inherent in parameter estimates, uncertainty due to simplification of models, and uncertainty in expert judgments. Additionally, variation in structural geometry and material properties contribute to uncertainties in seismic demand and capacity. 3. Building failure and damage due to earthquakes result in both direct and indirect economic losses. Direct losses include repair and replacement costs, which are influenced by the building's size, shape, design features, materials, and pre-damage geographic conditions. Consequently, the replacement cost of a building is subject to uncertainty. Indirect economic impacts are even more difficult to assess due to variability in losses and challenges in estimating recovery time.

A probabilistic approach is essential for accurately identifying, quantifying, and incorporating uncertainties associated with input parameters (Crowley et al., 2005). To minimize epistemic uncertainty, the approach requires detailed hazard, building, and cost information, which poses several challenges: 1. The latest seismic hazard models must be integrated, and the selection of ground motions should align with site-specific seismological conditions. A large dataset of ground motions is necessary to capture variability in response spectra and perform time history analyses. 2. Developing reliable fragility curves requires high-fidelity numerical models. These models should be validated using post-disaster building damage records or experimental tests to enhance the accuracy of damage predictions. 3. Both direct and indirect economic losses need to be accounted for, with appropriate price adjustments to estimate future costs accurately. A thorough risk-based framework is thus required to address these challenges and accurately assess the dollar value of the benefits. By providing a clearer understanding of the long-term benefits, such a methodological framework can help incentivize building owners to prioritize and invest in retrofitting measures.

2.4. Performance-Based Earthquake Engineering Framework

Seismic design codes establish criteria defining minimum levels of strength, stiffness, and ductility for buildings to ensure their safety and performance during earthquakes (Kam & Jury, 2017). The codes focus on protecting human life by preventing local or global collapse under a specific earthquake level that has a low probability of occurrence. However, the seismic events of the 1994 Northridge and 1995 Kobe earthquakes prompted the structural engineering community to reassess these design philosophies. Despite complying with existing seismic codes, the amount of damage, economic loss due to downtime, and repair cost of damaged building structures were unacceptably high (Lee & Mosalam, 2006).

The performance-based earthquake engineering (PBEE) framework holds the potential to replace the load-and-resistance-factor design (LRFD) method in design codes. A key distinction between the two approaches is that LRFD primarily focuses on ensuring the performance of individual structural components in terms of their failure probabilities. In contrast, PBEE aims to assess performance primarily at the system level, taking into account risks related to collapse, fatalities, repair costs, and the loss of function in earthquake events (Porter, 2003). The early versions of PBEE methodologies were detailed in several reports (ATC-40, 1996; FEMA-273, 1997; FEMA-356, 2000). The authors characterized PBEE as a methodology aimed at ensuring desired system performance across different levels of seismic excitations. However, these pioneering initiatives were constrained by their inability to comprehensively quantify all uncertainties. In response to the limitations of first-generation procedures, the Pacific Earthquake Engineering Research (PEER) Center developed a more robust PBEE methodology. This approach integrated rigorous probabilistic methods to account for uncertainties in earthquake intensity, ground motion characteristics, structural response, physical damage, and economic and human losses. As shown in Figure 2-10, the PEER PBEE methodology consists of four main steps: hazard analysis, structural analysis, damage analysis, and loss analysis (Günay & Mosalam, 2013). Each step is treated as a discrete Markov process, where the conditional probabilities between parameters are independent (Moehle & Deierlein, 2004).

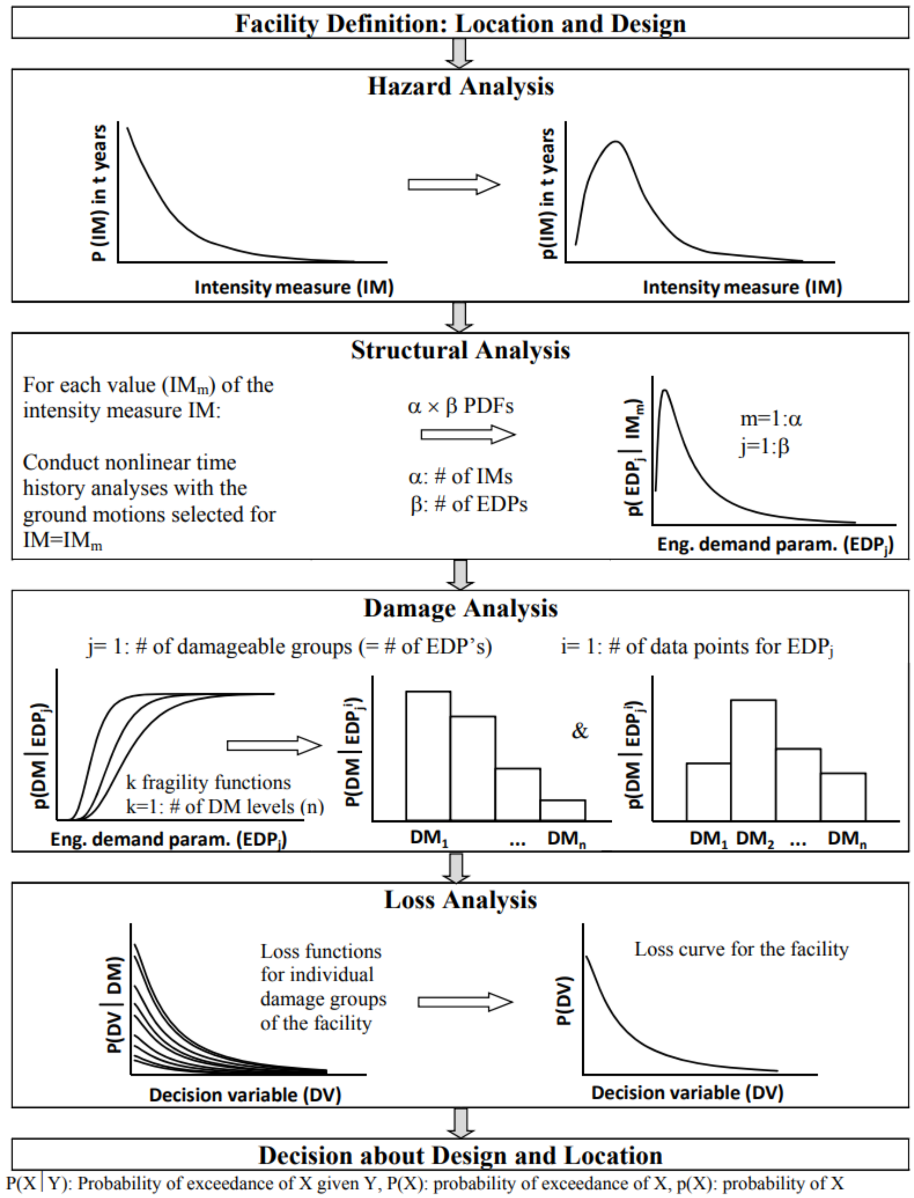

Figure 2-10: Analysis Stages of PEER PBEE Methodology (Günay & Mosalam, 2013)

The PBEE framework can be mathematically represented by integrating distribution functions using the principle of total probability, as expressed in Equation 2-4.

$$p(l) = \int\int\int p(l|dm)dp(dm|edp)dp(edp|im)dp(im) \qquad 2\text{-}4$$

where $p(l)$ is the annual rate exceedance for the loss l; $p(x|y)$ is the exceedance probability of x given y (e.g. complementary cumulative distribution function); dm is the damage measure (e.g. damage state); edp stands for the engineering demand parameters (e.g., maximum drift); im denotes the intensity measure(e.g. peak ground acceleration); $p(im)$ represents the expected rate of return of the seismic hazard (e.g., hazard curve).

A number of studies have utilized the PBEE framework to evaluate seismic retrofit strategies across various types of buildings (Carofilis et al., 2020; Dong & Frangopol, 2016; Harrington & Liel, 2021; Hutt et al., 2016; Vitiello et al., 2017). Hutt et al. (2016) conducted an analysis of a 40-story steel building in San Francisco and estimated the direct economic losses attributed to structural and non-structural damage. Dong and Frangopol (2016) demonstrated that installing base isolation reduced repair costs and carbon emissions for a 3-story steel building in Los Angeles subjected to simulated ground motion from the 1940 El Centro earthquake. These studies have demonstrated that the PBEE framework enables reliable estimations of seismic losses for steel structures.

2.5. Life-Cycle Cost-Benefit Analysis Framework

Seismic retrofitting utilizing friction devices, designed to control specific structural responses during a targeted design earthquake scenario, often falls short of ensuring the optimal economic performance of the system. This is primarily because the life-cycle cost-benefit analyses associated with various design scenarios are often overlooked in studies mentioned in Section 2.2.2. Consequently, even in cases where full retrofit with optimal slip load is implemented, it may not be economical (Zhang et al., 2024). Moreover, these designs typically do not explicitly quantify the various sources of uncertainties and reliabilities, further complicating the assessment of their economic efficiency. To address these issues, a risk-based seismic life-cycle cost-benefit analysis (LCCB) is proposed (Freddi et al., 2020; K. Lin et al., 2024; Padgett et al., 2010). This approach incorporates information on seismic hazard analysis, structural performance characteristics, seismic fragility assessment, costs related to damage, and expenses associated with retrofitting.

The life cycle cost of a structure subjected to seismic hazard can be estimated using the following equation (Dyanati et al., 2017; Zhang et al., 2022):

$$C_{LC}(t,\boldsymbol{X}) = C_0(\boldsymbol{X}) + C_M(t,\boldsymbol{X}) + C_{LCE}(t,\boldsymbol{X}) \tag{2-5}$$

where $C_{LC}(t,\boldsymbol{X})$ is the life-cycle cost, $C_0(\boldsymbol{X})$ is the initial construction cost, and $C_M(t,\boldsymbol{X})$ is the life-cycle operation and maintenance cost, and $C_{LCE}(t,\boldsymbol{X})$ is the life-cycle earthquake-induced cost. t is the life span of the building and $\boldsymbol{X}$ is the retrofit design vectors. To calculate the total cost over the expected life cycle of the building, the annual earthquake-induced cost, $C_{LCE}(1,\boldsymbol{X})$, is initially determined using the following equation:

$$C_{LCE}(1,\boldsymbol{X}) = EAL_{\boldsymbol{X}} \tag{2-6}$$

where $EAL_{\boldsymbol{X}}$ is the expected annual losses under $\boldsymbol{X}$ design and is calculated in accordance with the PBEE framework:

$$EAL_{\boldsymbol{X}} = \int_0^{\infty} l\,|dp(l)| \tag{2-7}$$

The life-cycle economic benefits $B_{LC\boldsymbol{X}}$, incorporating discount rate r, can thus be calculated from the reduced earthquake-induced loss through the following equation:

$$B_{LC\boldsymbol{X}} = [C_{LCE}(t) - C_{LCE}(t, \boldsymbol{X})] \sum_{T=1}^{T=t} (1 + r)^{-T} \qquad 2\text{-}8$$

where $C_{LCE}(t)$ is the life-cycle earthquake-induced cost of the existing building without seismic retrofits.

After estimating the initial retrofit cost $C_{\boldsymbol{X}}$ associated with design $\boldsymbol{X}$, the LCCB can be compared using two metrics: benefit-cost ratio (BCR) and net present value (NPV) (Fung et al., 2022).

$$BCR_{\boldsymbol{X}} = \frac{B_{LC\boldsymbol{X}}}{C_{\boldsymbol{X}}} \qquad 2\text{-}9$$

$$NPV_{\boldsymbol{X}} = B_{LC\boldsymbol{X}} - C_{\boldsymbol{X}} \qquad 2\text{-}10$$

where $BCR_{\boldsymbol{X}} > 1.0$ and $NPV_{\boldsymbol{X}} > 0$ indicates that the monetary benefit of the seismic retrofits outweighs the cost, demonstrating the cost-effectiveness.

In the life-cycle cost-benefit analysis process, data from the HAZUS model are adopted to link a building's structural performance with monetary losses (Federal Emergency Management Agency (FEMA), 2012; Günay & Mosalam, 2013; Kircher et al., 2006; Porter, 2003). The HAZUS method of estimating direct building losses closely resembles the general four-step approach in the PBEE method. The primary difference lies in that HAZUS directly correlates hazard and damages through the use of empirical data and expert judgment, without explicitly conducting structural analysis of buildings

(Kircher et al., 2006). In addition to the direct cost of building repair and replacement, HAZUS also incorporates non-material costs such as income loss and relocation expenses.

This thesis will integrate HAZUS data into the PBEE framework in seismic loss assessment. In particular, seismic capacity models and cost estimations will be obtained from HAZUS data. A workflow illustrating these methods is presented in Figure 2-11. To date, there is a limited body of literature on conducting a comprehensive LCCB analysis of seismic retrofitting for steel buildings, with only a handful of studies investigating the benefits of such retrofitting measures (Dong & Frangopol, 2016; Hutt et al., 2016). This thesis aims to bridge these gaps by implementing the LCCB framework to evaluate seismic retrofitting of benchmark steel buildings in Canada.

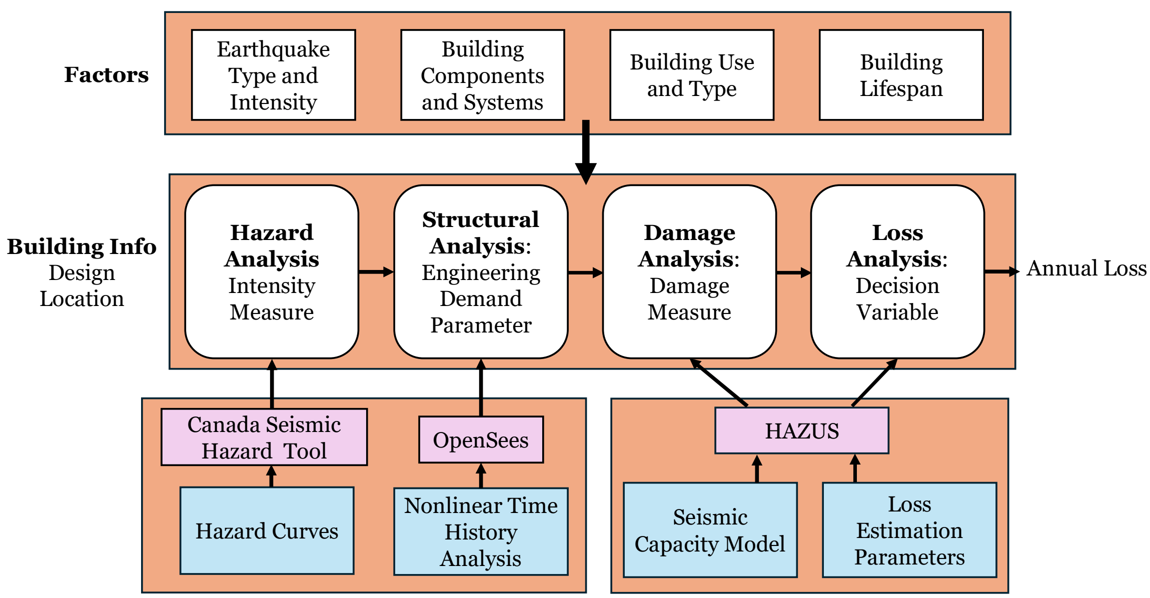

Figure 2-11: Seismic loss estimation workflow integrating PBEE framework and HAZUS

Chapter 3. Benchmark 1960s Steel Buildings in Canada

3.1. Benchmark Building Design

A six-story office building is benchmarked as a representative steel frame structure in Canada. The structure was initially proposed in the studies from Biddah and Heidebrecht (1998, 1999), where they focused on evaluating the seismic performance of steel MRFs designed in Victoria, Vancouver, and Montreal, against high, intermediate, and low seismic hazards, respectively. The same structural layout has been further investigated by Gomez (2014, 2015), where it serves as a representative structure in Canada for comparisons between various design purposes. The six-story steel MRF was redesigned and assessed in Montreal and Vancouver following the design provisions of NBCC in the three periods: 1960s, 1980s, and 2010. The buildings' performance was assessed through pushover and nonlinear time history analysis. Pushover analysis revealed that both the 1960s and 2010 steel MRFs in both cities exhibited a strong-column-weak-beam failure mode. On the other hand, the 1980s steel MRFs in both cities demonstrated a soft-story mechanism. Additionally, seismic fragility curves were constructed and compared. This study demonstrates the impact of seismic design practice evolution over time on structural seismic performance. This study utilizes the structural designs provided by Gómez (2014, 2015) as representative examples of the 1960s steel buildings located in Montreal and Vancouver.

3.2. Building Description

3.2.1. Building Layout and Design Loads

The building features a plan view characterized by a rectangular layout, spanning three bays by four bays. The lateral force resisting system (LFRS) of the building is composed of steel braced frames in the north-south direction and steel MRFs in the east-west Direction. This study focuses on the steel MRF in the east-west direction. In the elevation view, the building comprises a ground floor with a height of 4.5 meters, and other floors each have a height of 3.6 meters, giving a total building height of 22.5 meters. Figure 3-1 illustrates the plan view and elevation view of the building, respectively. In addition, Figure 3-2 provides a three-dimensional representation of the entire structure.

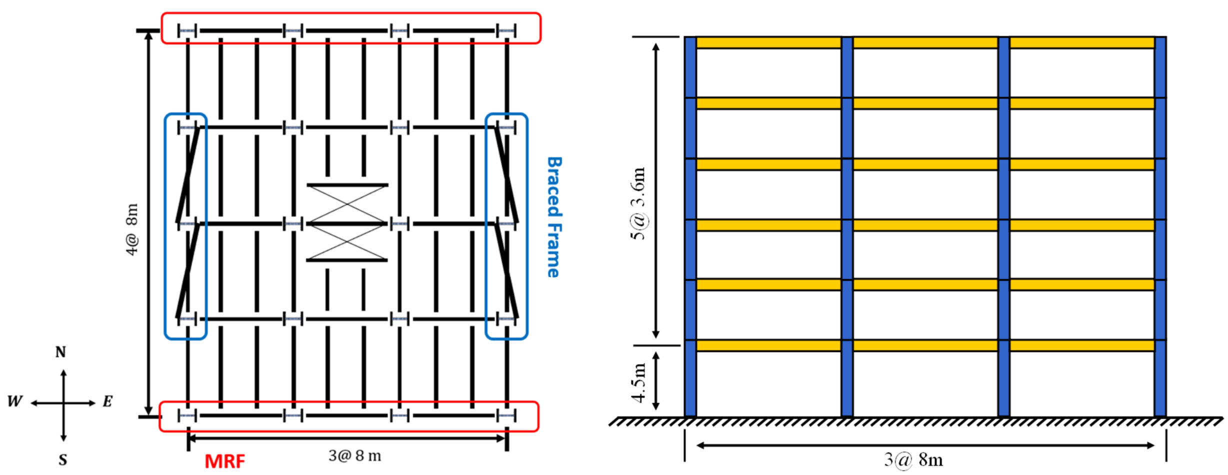

(a) (b)

Figure 3-1 (a) Plan view and (b) elevation view of the building

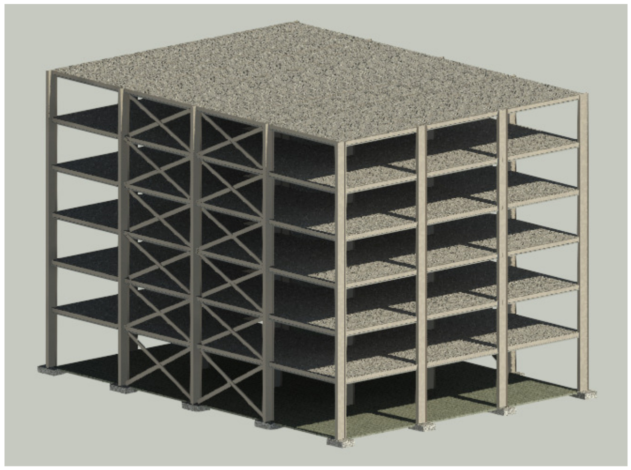

Figure 3-2 Three-dimensional Rendering of the building

The structure is symmetrical in both directions. The interior columns are designed to support gravity loads only. The roof and floors consist of equally spaced secondary steel beams with composite concrete and steel deck slabs. The intended use of the building is for office purposes, categorized under normal importance, and the site class is Type C. The design gravity loads are presented in Table 3-1.

Table 3-1 Design gravity loads of the steel building

Load	Type	Detailed Loads (kPa)	Load (kPa)
Live	Offices areas - 1st storey	4.8	4.8
	Offices areas - above 1st storey	2.4	2.4
	Roof	1	1
Dead Floor	Partitions	1	4.6
	Floor finish	0.2	
	Concrete slab and steel deck	2.5	
	Floor framing	0.4	
	Mechanical and ceiling	0.5	
Dead Roof	Insulation and vapour barrier	0.2	2.95
	Mechanical and ceiling	0.05	
	Membrane	0.3	
	Concrete slab and steel deck	2	
	Roof framing	0.4	
Exterior Wall	Cladding (on the vertical face)	1.5	1.5

3.2.2. Structural Design Process

The allowable stress design (ASD) and imperial units were prevalent in the period of 1960s, and the structural design of a steel building follows the codes NBCC 1965 and CSA S16-1969 (Gómez, 2014). As mentioned previously, there were no seismic design provisions in CSA S16 prior to 1989, and engineers prioritized the design of LFRS to resist wind loads. This practice stemmed from the observation that the base shear induced by wind loads typically exceeded that caused by seismic loads. An example calculation and comparison of the two lateral loads for the building in Montreal are provided below.

The wind pressure p is defined in NBCC 1965 as follows:

$$p = qC_hC_p \tag{3-1}$$

$$C_h = \left(\frac{h}{30}\right)^{\frac{1}{5}} \tag{3-2}$$

where q is the velocity pressure at the structure location, C_h is the height factor, C_p is the external pressure coefficient, and h is the height at the level of evaluation. The external pressure coefficients for windward (C_{pw}) and leeward (C_{pl}) sides are 0.9 and -0.5 respectively. For NBCC1965, the designated velocity pressure is 15 psf for Montreal and 22 psf for Vancouver. The total wind-induced base shear of the Montreal structure is 682 kN and the distribution of wind loads on one side of the steel MRF is shown in Figure 3-3.

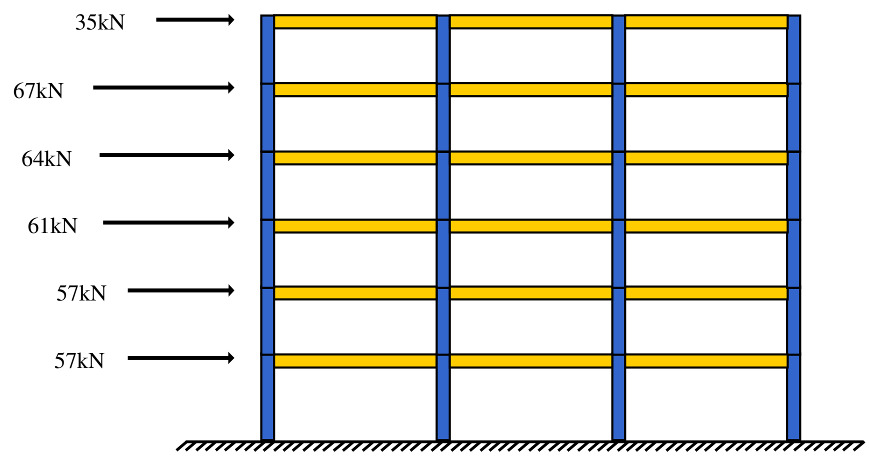

Figure 3-3 Distribution of wind loads for Montreal structure

The seismic load is calculated in NBCC 1965 as follows:

$$K = RCIFS \qquad 3\text{-}3$$

where R is the earthquake factor, C is the construction factor, I is the importance factor, F is the foundation factor, and S is a number reflecting the number of storeys of the building. The designed base shear and distribution of the seismic loads are determined by the following formula:

$$V = KW \qquad 3\text{-}4$$

$$F_x = V\frac{w_x h_x}{\sum wh} \qquad 3\text{-}5$$

where W is the seismic weight, F_x is the lateral force at level x, V is the base shear, w_x is the portion of weight assigned to that level, h_x is the height in feet above the base at level x, and $\sum wh$ is the sum of the product of w_x and h_x of the whole building. Presented in Figure 3-4, the base shear obtained from seismic load calculation stands at 434 kN, which is 64% of the base shear attributed to wind load. Despite wind load exerting a greater base shear compared to seismic loads, the force distributions are different. Nonetheless, engineers during that era typically focused solely on designing for wind load, neglecting to account for load distribution variations.

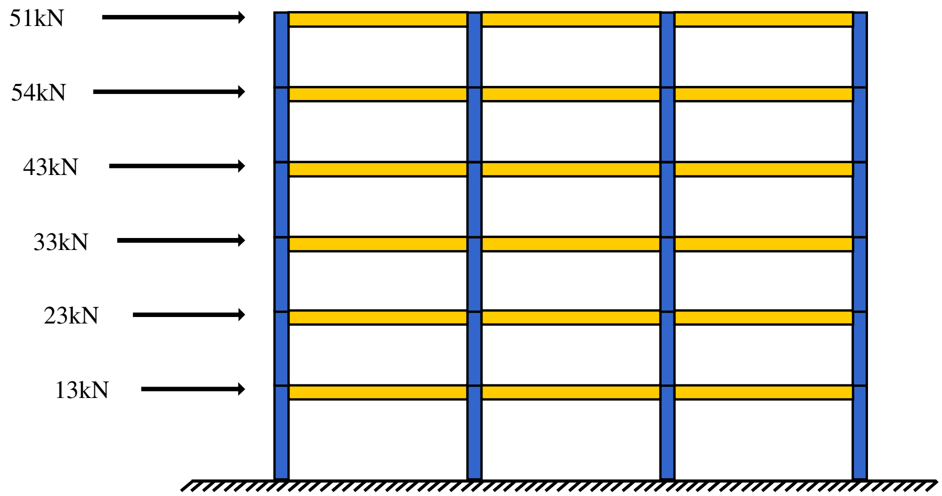

Figure 3-4 Distribution of seismic loads for Montreal structure

The ASD design approach requires that the stresses due to the loads in the structural member must be less than the permitted stresses. The wide flange sections, manufactured with the steel ASTM A36, are selected for construction. ASTM A36 is a low-carbon steel material widely adopted in the 1960s and has a yielding stress of 36ksi or 248MPa. During preliminary design, beam sections are first configured as simply supported under gravity loads within the Type 2 Construction specification. Beam webs and flanges are checked against the prescribed width-to-thickness ratio to ensure bending resistance; beam sections need to be verified to yield due to bending moments before reaching shear capacity. The columns are subsequently designed, ensuring their stresses are lower than the allowable stresses. Additionally, column sections must satisfy slenderness ratios for both the web and flanges to avoid buckling before reaching structural capacity. The connections are then designed after the selection of appropriate beam and column sections.

Type 2 with Wind connections are designed solely to withstand wind loads. The material employed for the connection is ASTM A36, with the welding using the E60 electrode. In the WFP configuration, the web of a beam consists of a single plate field bolted to the beam web and shop wielded to the column flange. The flange connection comprises a moment plate field welded to the column flanges and top and bottom beam flanges. The web connection, flange connection, column shear capacity, column web stiffener, and the stiffener welds are checked against the unbalanced moments. The final sections for the 1960s steel MRF in Montreal and Vancouver are described in Table 3-2 and shown in Figure 3-5.

Table 3-2 Building structural sections summary

City	**Storey**	**Columns**		**Beams**
		Exterior	**Interior**	
Montreal	6	W10×33	W12×45	W18×40
	5	W10×33	W12×45	W18×50
	4	W12×45	W14×82	W18×50
	3	W12×45	W14×82	W18×50
	2	W14×61	W14×159	W18×50
	1	W14×61	W14×159	W18×50
Vancouver	6	W12×45	W12×45	W18×40
	5	W12×45	W12×45	W21×50
	4	W14×109	W14×109	W21×50
	3	W14×109	W14×109	W21×50
	2	W14×193	W14×193	W21×50
	1	W14×193	W14×193	W21×50

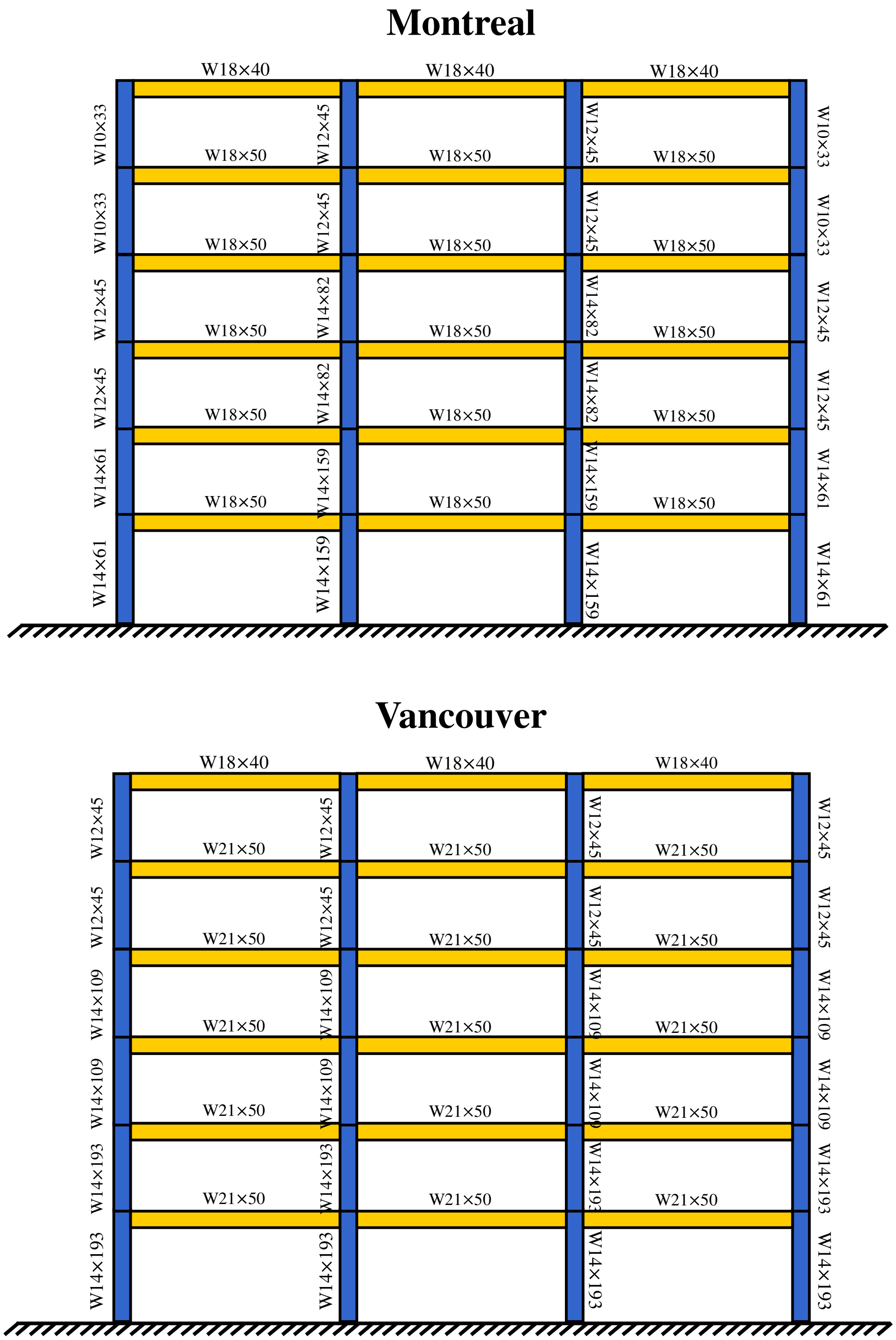

Figure 3-5 Schematic of building structural sections

3.3. Numerical Modeling of the Steel MRF and Friction Devices

3.3.1. Beam and Column Modeling

Numerical models for steel MRFs can generally be categorized into three types: concentrated hinge models, fiber-type models, and continuum finite element models (Applied Technology Council, 2017). In general, continuum finite element models are most accurate at simulating localized effects within structural members and connections. On the other hand, concentrated hinge or fiber-type discrete models are more adept at practical applications for modeling the overall response of entire frame systems. A schematic of those inelastic models, organized in the order of complexity and accuracy, is shown in Figure 3-6. The numerical models in this study adopt the combination of concentrated hinge models and fiber-type models.

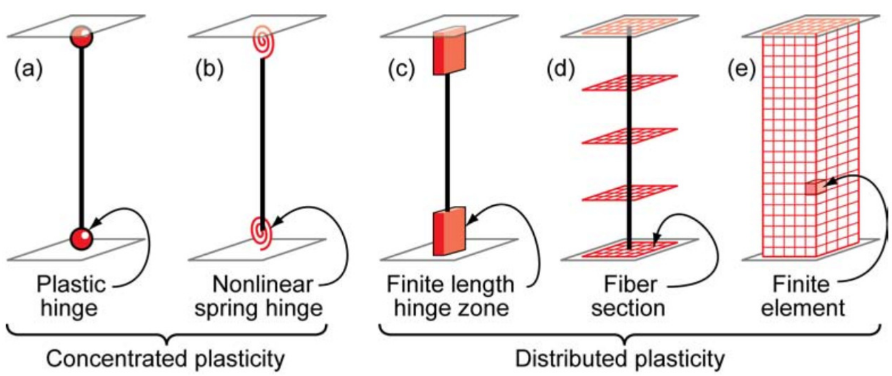

Figure 3-6 Idealized models of structural elements (Deierlein et al., 2010)

Because of the symmetry of the building, a two-dimensional numerical model of the steel MRF is developed in OpenSees (McKenna, 2011) for the frame on each side, as shown in Figure 3-7. Each steel MRF, assumed located in Montreal and Vancouver respectively, has its own design and numerical model. The beams and columns constituting the steel MRFs are modeled using the fiber section with distributed plasticity.

The fiber cross-section models can capture axial and flexural effects ($P - \delta_x$ and $M - \Phi$) as stresses and strains are integrated through the cross-section during the analysis. The uniaxial material model Steel02 with isotropic strain hardening is used to simulate the ASTM 36 steel and the stress hardening ratio is assumed to be 0.01. The columns are assumed to be fully fixed at their bases. The steel beams are considered to have simple wide flange sections without the composite behaviors with the floor deck since they are not explicitly designed as composite beams in the MRFs. Diaphragms are applied on each level to simulate the impact of the slab on the overall structural behavior.

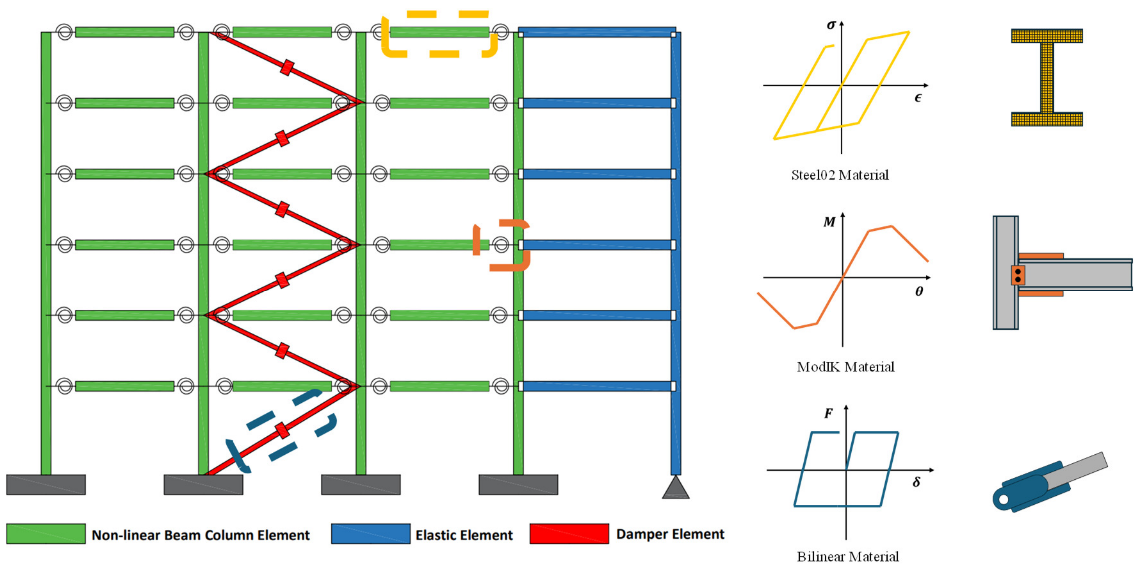

Figure 3-7 Schematic representation of the numerical models

The gravity columns and beams are not explicitly modeled because it is generally considered acceptable and conservative to ignore the strength and stiffness of the gravity framing (Applied Technology Council, 2017). The destabilizing geometric stiffness ($P - \Delta$) effects of the gravity system have been taken into consideration in the nonlinear analysis by adding one pin-ended leaning column. The truss elements are used to connect the leaning column to the MRF with hinges at the ends. Consequently, only an extra overturning moment due to lateral displacement will be generated and the leaning columns, being pinned, do not bear lateral loads. The leaning columns are modeled with elastic elements, and they share the same material model Steel02 as the MRF columns. Additionally, the moment of inertia of the leaning column approximately equals that of the gravity columns, and the leaning column at each level carries a corresponding tributary gravity load.

3.3.2. Connection Modeling

Lumped spring models, which concentrate the inelastic deformations of the member in the hinges with zero length elements, are used to simulate the behavior of beam-column connections in the steel frame. These hinge models are based on calibration test data and can simulate nonlinear behaviors such as strength/stiffness degradation and pinching. Ibarra et al. (2005) developed the modified Ibarra and Krwinkler model (ModIK) that is capable of simulating cyclic deterioration, softening of the post-yielding stiffness, and residual strength after deterioration of a structural assembly. This model has been extensively validated and shown to adequately capture the behavior of steel beam-to-column connections subject to strength deterioration for full-moment connections and reduced beam section connections (Lignos & Krawinkler, 2011). The model was further refined by incorporating calibrated deterioration parameters and predictive equations derived from a comprehensive analysis of over 300 experiments involving steel components.

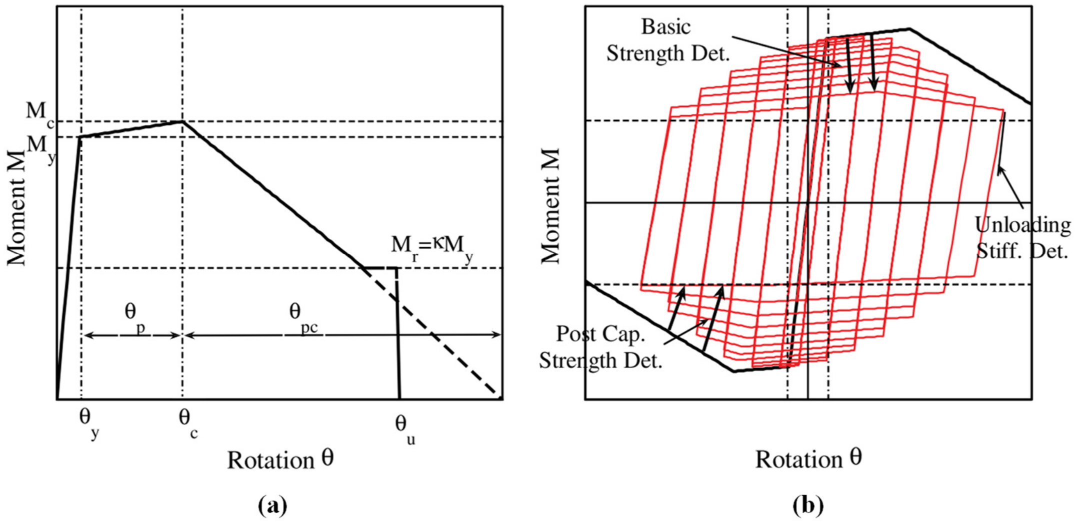

Figure 3-8 ModIK model: (a) monotonic curve and (b) cyclic deterioration (Lignos & Krawinkler, 2011)

Figure 3-8(a) illustrates a monotonic backbone curve of the ModIK model, characterized by three strength parameters and four deformation parameters. The strength parameters include effective yield moment M_y, capping moment strength M_c, and residual moment $M_r = \kappa M_y$; the four deformation parameters include yield rotation θ_y, pre-capping plastic rotation θ_p, post-capping plastic rotation θ_{pc}, and ultimate rotation capacity θ_u. Additionally, Figure 3-8(b) delineates the ModIK model's various modes of cyclic deterioration, comprising basic strength stiffness deterioration, post-capping strength stiffness deterioration, and unloading and reloading stiffness deterioration.

The numerical model of the beam-column connections in the current structure is based on the parameters proposed by Lignos & Krawinkler (2011) for connections other than the reduced beam section (RBS). Subsequently, this model undergoes calibration using experimental results obtained by Kyriakopoulos (2012), who experimentally studied the behavior of the connections of a steel MRF building from the 1960s. The building is a nine-story hospital near Quebec City, and it was designed under the Type 2 Construction philosophy. Two single-story frames, built with member sizes closely resembling full-scale dimensions, were constructed and tested. One of the frames, consisting of a beam with a W18x50 (W460x74) section, two columns with W14x176 (W360x262) sections, and a connection with half-inch flange plates, is used to validate the connection behavior in this thesis. The cyclic loading was applied to the experiment assembly, as shown in Figure 3-9, following the loading history proposed by the SAC Joint Venture (1997). A moment versus rotations plot of the connection behavior is illustrated in Figure 3-10.

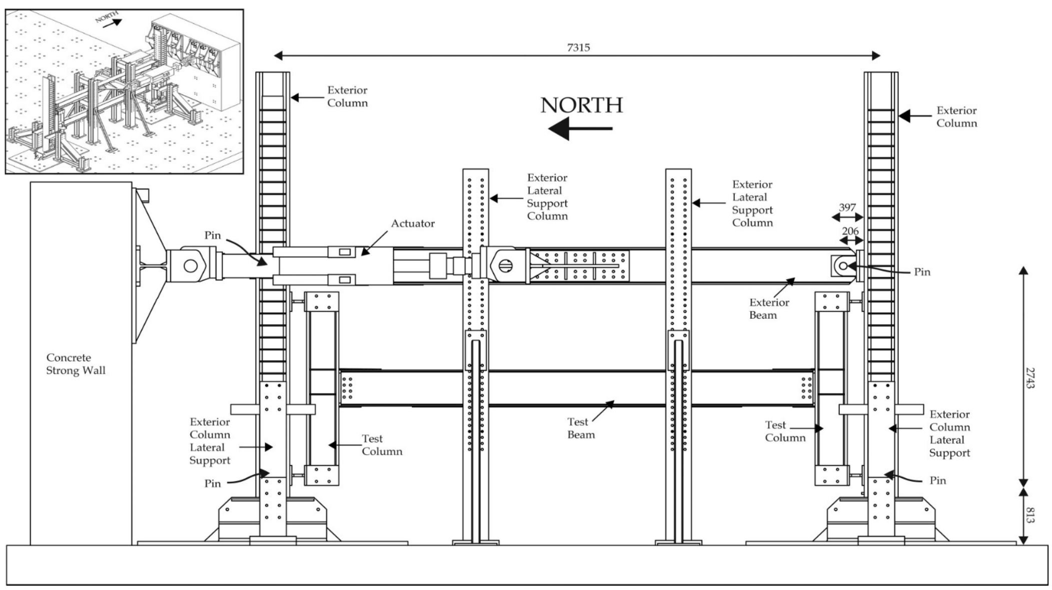

Figure 3-9 Type 2 with Wind connection experimental test setup (Kyriakopoulos & Christopoulos, 2013)

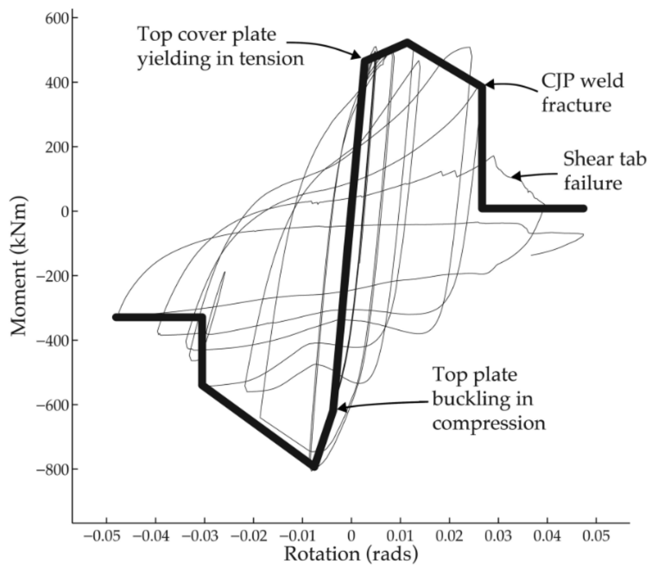

Figure 3-10 Hysteresis of connection with a backbone curve (Kyriakopoulos, 2012)

The predicting equations for the initial rotation stiffness K_θ and yielding moment M_y of the connection are proposed as follows:

$$K_\theta = \frac{EI}{L} \tag{3-6}$$

$$M_y = SF_y \tag{3-7}$$

where E is the Young's modulus of the steel, I is the moment of inertia of the connections, L is the length of the connection, S is the section modulus of the connection, and F_y is the yielding stress. The connection consists of flange plates and a shear tab, and the length of the connection is taken as the distance between the column face to the location where the plate is fastened to the beam, which is 12 in. Four parameters in the numerical model developed by Lignos and Krawinkler (2011) are calibrated to enhance the prediction of connection behavior. Table 3-3 presents a comparison of both sets of parameters. The parameters derived from Lignos and Krawinkler (2011) serve as the initial reference point, as they are obtained from experimental results where yielding occurred primarily in the beams. However, in the connections under consideration, yielding and failure predominantly occur within the connection elements. The calibrated values of θ_p, θ_{pc}, and θ_u are found to be smaller than those in Lignos and Krawinkler (2011), indicating that the actual performance of the connection is inferior to what would be inferred using the original parameters. The numerical modeling parameters proposed by Kyriakopoulos more accurately captures the behavior of the Type 2 Construction connection.

Table 3-3 Comparison of initial and calibrated ModIK model parameters

Reference	**Post-Yield Rotation θ_p**	**Post-Capping Rotation θ_{pc}**	**Ultimate Rotation θ_u**	**Residual Moment Factor κ**
(Lignos & Krawinkler, 2011)	0.051	0.177	0.06	0.4
(Kyriakopoulos, 2012)	0.0216	0.0145	0.0475	0.2

3.3.3. Friction Device Modeling

The friction devices are installed in the inter-stories of the building with additional supporting braces. In this system, one end of the brace is typically affixed to the upper corner of the frame, while the other end is linked to the friction damper which itself is fixed to the lower opposite corner, as shown in Figure 3-11 (a). Consequently, the friction device and the brace are connected in series with each other.

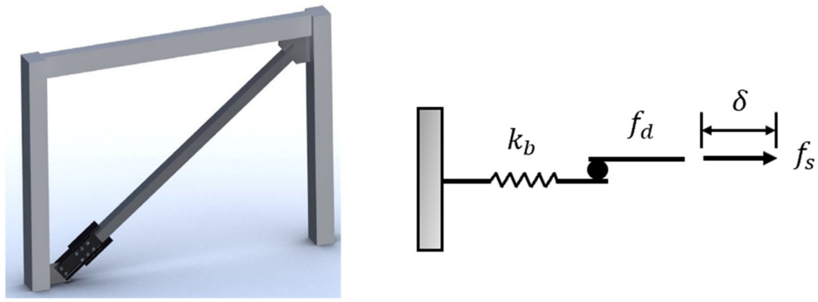

(a) (b)

Figure 3-11 Friction damper-bracing system: (a) structural layout (Armali et al., 2019) *(b) idealized model*

The friction-device bracing system can be simulated through Figure 3-11 (b), where k_b is the stiffness of the brace, δ is the total displacement, f_d is the frictional force of the damper, and f_s is the force applied to the entire friction damper-bracing system. As a series system, the force applied to the entire system, the axial force in the brace, and frictional force of the damper are equivalent (Lee et al., 2008).

$$f_s = f_d = k_b \delta_b \qquad 3\text{-}8$$

The total displacement can be calculated as:

$$\delta = \delta_b + \delta_d \qquad 3\text{-}9$$

where δ_b and δ_d are displacements of brace and damper, respectively.

The hysteretic loop of a friction damper-bracing assembly is simulated using a bilinear model as shown in Figure 3-12, where the stiffness is governed by the connecting braces and a flat yielding line defined by the slip load of the friction device. The friction damper-bracing systems are incorporated into the center bay of the Steel MRF with a zigzag layout in this study as shown in Figure 3-13. Such configuration provides a clear and continuous load path for the transferring of the seismic loads and is architecturally aesthetic because of its symmetry (Gasim & Lakshmi, 2016).

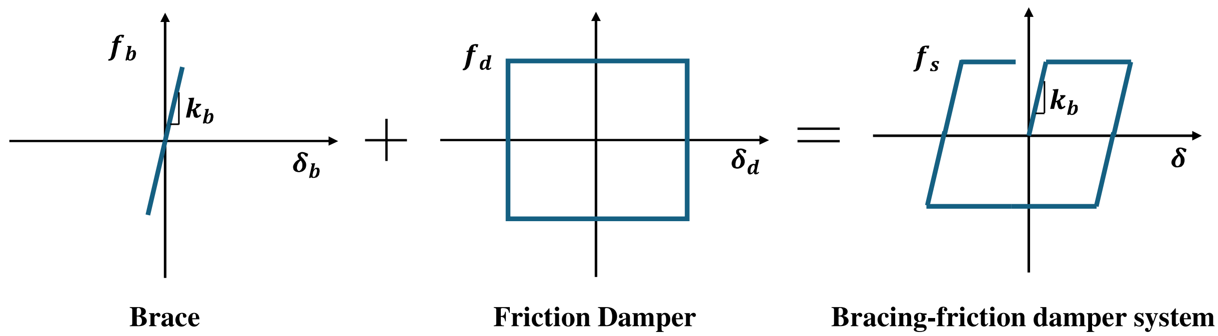

Figure 3-12 Hysteretic loop of a braced friction damper system

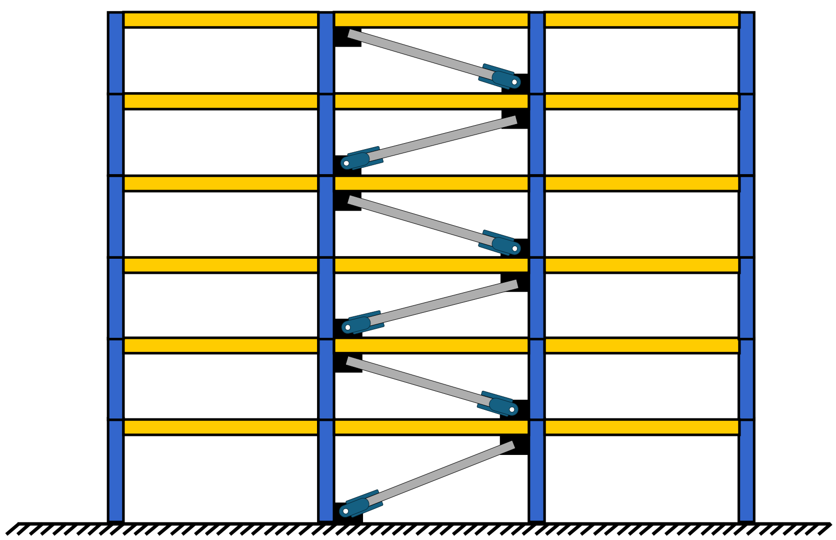

Figure 3-13 Steel MRFs retrofitted with friction damper-bracing systems

Chapter 4. Seismic Retrofit Design of the Friction Damper Bracing System

4.1. Assessing the Necessity of Seismic Retrofits

To assess the seismic deficiencies and the need for seismic retrofitting, an initial seismic evaluation of the 1960s buildings is conducted with the equivalent static force procedure (ESFP) outlined in the earthquake design provisions of the latest NBCC (2020). ESFP is a simplified procedure that substitutes the effect of dynamic loading of an anticipated earthquake by a static force distributed laterally on a structure for design considerations. This method relies on the assumption that the building primarily responds in its fundamental lateral mode. To uphold this assumption, the building must be less than 60 m in height and possess a degree of symmetry to avoid torsional moments induced by ground motions, as required by NBCC 2020. The benchmark buildings in Montreal and Vancouver both satisfy these required conditions and thus qualify for the simplified approach.

First, the fundamental period T_a in the direction of consideration is determined using an empirical equation for the steel MRF:

$$T_a = 0.085(h_n)^{\frac{3}{4}} \tag{4-1}$$

where h_n is the height of the structure. The numerical models compute the fundamental periods of the structures in Montreal and Vancouver as 2.9 s and 2.4 s, respectively, from which NBCC2020 allows an elongation of T_a with an upper limit of 1.5 times, as follows:

$$T_a = 1.5 \times 0.085(h_n)^{\frac{3}{4}} = 1.3\ s \tag{4-2}$$

The second step calculates the seismic weight of the structures, which includes specified dead loads (with the partition weight capped at 0.5 kPa), 25% of the specified snow loads, and tributary exterior wall weight. The calculated seismic weights are shown in Table 4-1. The base shear forces of the buildings are subsequently calculated using the following equation:

$$V = \frac{S(T_a)M_v I_E W}{R_d R_0} \quad (4\text{-}3)$$

where V is the design lateral earthquake base shear, $S(T_a)$ is the spectral acceleration from the uniform hazard spectrum (UHS) against the fundamental period T_a of the structure, M_v is the higher mode factor, I_E is the importance factor, W is the seismic weight, and R_d and R_0 are ductility factor and overstrength factor, respectively.

Table 4-1 Seismic weights of the benchmark structures

City	Type	Dead (kPa)	25% Snow Load (kPa)	Exterior Wall (kPa)	Seismic Weight (kN)	Total Seismic Weight(kN)
Montreal	Roof	2.95	0.62	1.5	3044	21888
	Intermediate Floors	4.1	-	1.5	3754	
	First Floor	4.1	-	1.5	3829	
Vancouver	Roof	2.95	0.41	1.5	2883	21726
	Intermediate Floors	4.1	-	1.5	3754	
	First Floor	4.1	-	1.5	3829	

The ductility factor, R_d, is related to the inelastic characteristics of the structural system, such as energy dissipation and strength degradation (Annan et al., 2008). This factor reflects the capability of a structure to dissipate energy through reversed cyclic inelastic behavior (NBCC 2022). In contrast, the overstrength factor, R_o, reflects the inherent reserved strength within the structural system. It accounts for the dependable portion of additional strength beyond the nominal design strength, which contributes to the structure's response under seismic loading. Building structures often retain a significant amount of reserve strength owing to various factors, including material effects, structural system configuration, and design assumptions and simplifications. In NBCC 2020, the $R_d R_o$ combinations for steel LFRS are determined based on assumed ductility, type, and construction method. For example, a ductile steel MRF is assigned $R_d R_o = 7.5$, whereas a limited ductility steel MRF is assigned $R_d R_o = 2.6$. Currently, no specific $R_d R_o$ designation is provided for a steel MRF retrofitted with friction dampers. Although such a retrofitted frame resembles a braced frame in layout, the addition of friction devices is expected to provide significantly greater energy dissipation capabilities compared to conventional braced frames. Considering the combinations of $R_d R_o$ designated in NBCC 2020 and characteristics of friction dampers, a set of benchmark combination, $R_d R_0 = 2.6, 5.5, 7.5, 10, 12$, is employed in the analysis process. These combinations are adopted to reflect a range of realistic design scenarios, accounting for the structural system's ductility and overstrength characteristics. $R_d R_0 = 5.5$ will be utilized as an example case for illustration purposes, while the results of other combinations will be directly presented. The UHS data pertaining to Soil Class C in both Montreal and Vancouver are retrieved from the Canada Seismic Hazard Tool (2020), as shown in Table 4-2.

Table 4-2 Uniform hazard spectrum data for Soil Class C in Montreal and Vancouver (Earthquake Canada, 2021)

City	Sa (0.05)	Sa (0.1)	Sa (0.2)	Sa (0.3)	Sa (0.5)	Sa (1.0)	Sa (2.0)	Sa (5.0)	Sa (10.0)
Vancouver	0.661	0.95	1.08	1.08	0.866	0.503	0.306	0.0871	0.0369
Montreal	1.27	1.18	0.837	0.661	0.488	0.256	0.115	0.03	0.00968

When $R_d R_0 = 5.5$, the seismic base shears in two locations are calculated through linear interpolations as follows:

$$V_{Montreal} = \frac{0.214 \times 1.0 \times 1.0 \times 21888}{5.5} = 852kN$$

$$V_{Vancouver} = \frac{0.444 \times 1.0 \times 1.0 \times 21726}{5.5} = 1754kN$$

The lateral earthquake force V is distributed laterally to the structure such that a fraction, F_t, is concentrated on the top of the building. The remaining portion, $V - F_t$, is allocated throughout the height of the building in accordance with the following formula:

$$F_t = 0.07T_a V < 0.25V \quad \text{4-4}$$

$$F_x = (V - F_t)\frac{W_x h_x}{(\sum_{i=1}^{n} W_i h_i)} \quad \text{4-5}$$

where F_x is the seismic force exerted at level x. Since the structures consist of two steel MRFs in each direction of seismic loading, the forces in the individual LFRS need to consider the torsional effects of the building. The analysis involves applying torsional moments around a vertical axis at each level of the structure. This is conducted independently for each of the following load cases:

$$T_x = F_x(e_x + 0.10D_{nx}) \tag{4-6}$$

$$T_x = F_x(e_x - 0.10D_{nx}) \tag{4-7}$$

where T_x is the floor torque in floor x, e_x is the distance between the centre of mass and rigidity, D_{nx} is the plan dimension of the building perpendicular to the direction of seismic loading. The steel MRF system is considered to counteract the in-plane torsional moments, therefore, the lateral force acting on a level of the single steel MRFs is about 60% of the total earthquake load F_x, as shown in Figure 4-1.

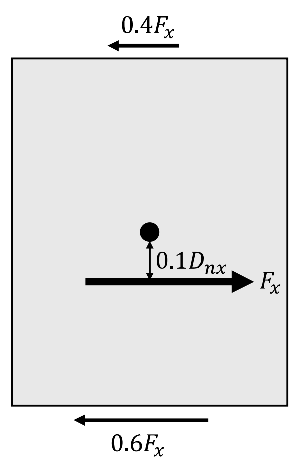

Figure 4-1 Torsional effects on the structure

The load combination under earthquake scenarios is prescribed as following:

$$1.0D + 1.0E + 0.5L + 0.25S \tag{4-8}$$

Thus, the linear loads on the Steel MRFs in accordance with tributary areas are calculated and shown in Table 4-3. These vertical loads are applied to the structure during the pushover analysis.

Table 4-3 Line loads applied to the steel MRF in ESFP

City	Level	Dead (kPa)	Live (kPa)	Snow (kPa)	Linear Load (kN/m)
Montreal	6	2.95	1.00	2.48	16.28
	5	4.60	2.40	0.00	23.20
	4	4.60	2.40	0.00	23.20
	3	4.60	2.40	0.00	23.20
	2	4.60	2.40	0.00	23.20
	1	4.60	4.80	0.00	28.00
Vancouver	6	2.95	1.00	1.64	15.44
	5	4.60	2.40	0.00	15.44
	4	4.60	2.40	0.00	23.20
	3	4.60	2.40	0.00	23.20
	2	4.60	2.40	0.00	23.20
	1	4.60	4.80	0.00	28.00

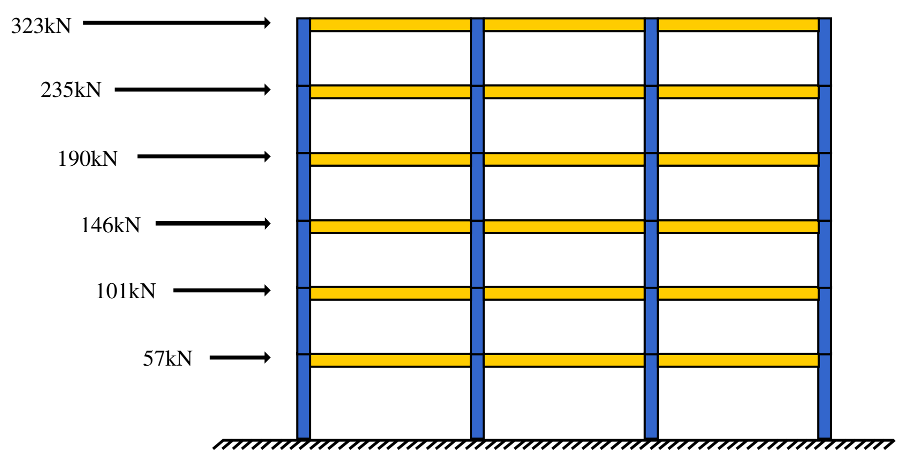

Figure 4-2 Distribution of seismic loads for structure in Vancouver

Distributed seismic loads for the structure in Vancouver are shown in Figure 4-2. A linear elastic pushover analysis of the base structure is executed to evaluate the lateral deformation at each level, which is multiplied by $R_d R_0 / I_E$ to acquire anticipated deflections. As per NBCC2020, the largest inter-story deflection at any level should adhere to the following limitations: $0.01hs$ for post-disaster buildings, $0.02hs$ for high importance category buildings, and $0.025hs$ for normal importance category buildings.

Upon the analysis of the pushover results, the anticipated inter-story deflection exceeds the allowable deflection at every level, as shown in Table 4-4. This shows that a seismic retrofit of the building is necessary.

Table 4-4 Inter-story drift ratios from pushover analysis when $R_d R_o = 5$

City	Type	Level	Interstory Drift Ratio (%)
Montreal	Roof	6	2.72%
	Floor	5	4.68%
	Floor	4	4.68%
	Floor	3	5.59%
	Floor	2	4.99%
	Floor	1	3.32%
Vancouver	Roof	6	4.65%
	Floor	5	7.54%
	Floor	4	6.84%
	Floor	3	7.81%
	Floor	2	7.02%
	Floor	1	4.26%

In addition, wind loads are also calculated for the two base structures per NBCC 2020. The wind loads of the Vancouver building are shown in Figure 4-3, which confirms that the lateral loads of the two buildings are controlled by seismic loads. Detailed wind load calculations are provided in Appendix A.

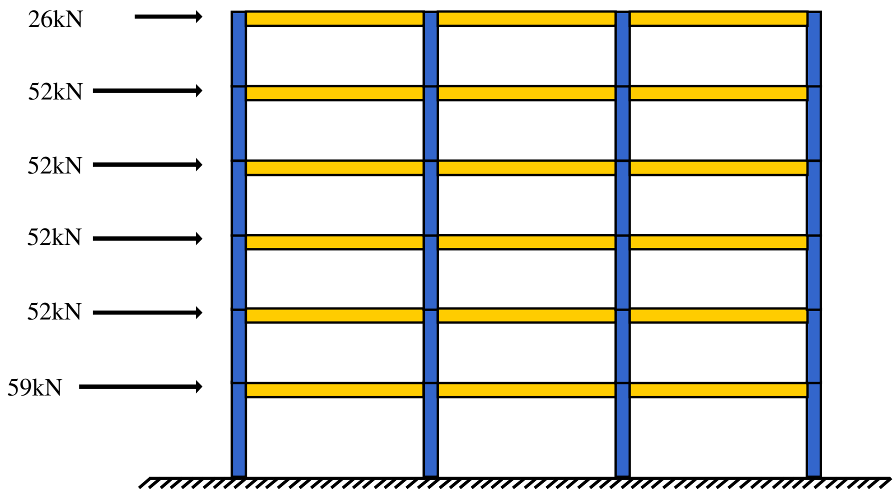

Figure 4-3 Distribution of wind loads for the structure in Vancouver

4.2. Seismic Upgrades using Friction Devices

As described in previous sections, the friction bracing system consists of a steel brace linked in series with a friction damper. The system adds stiffness and damping to the building frame and dissipates energy through the slippage and subsequent generation of hysteresis loops corresponding to displacement cycles. To that end, an iterative, displacement-based design approach is proposed for determining the axial stiffness of the brace and the slip load of friction dampers.

The friction damper at each story is considered to activate and slip when the inter-story drift ratio reaches 1.5% (Anderson et al., 1999). To identify the corresponding slip load, diagonal steel braces with linear elastic truss elements are added to the frame model, as shown in Figure 4-4. The area of each steel brace is then adjusted until each story experiences a drift ratio that is very close to 1.5% under lateral pushover analysis when subjected to the design-level seismic force. The slip force of the friction damper at level i, F_i, is then determined by extracting the corresponding axial force of each seismic brace.

As an iterative process is needed for keeping adjusting the sizes of diagonal braces until the 1.5% drift ratio is achieved at each story, the model of the steel MRF is changed to be a linear model to ensure design convergence and improve efficiency. However, at the interstory drift ratio of 1.5%, the beams of the frame are assumed to be yielded, whereas a soft story mechanism might be developed at the first story (Kyriakopoulos, 2012). To account for these damaging mechanisms, the moment of inertia for the elastic beam elements and the first-story column elements are reduced by 95%, as shown in Figure 4-4.

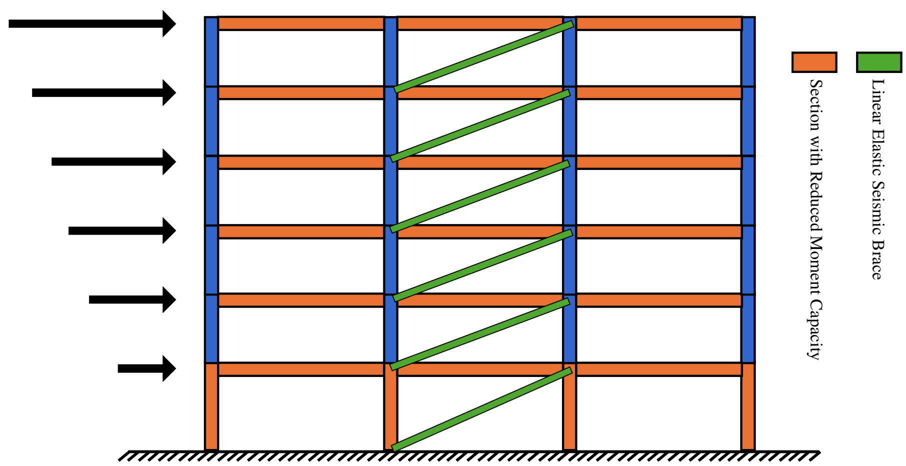

Figure 4-4 Revised steel MRF for the determination of damper force

Other than the damper slip load, the steel brace connected with the friction damper at each story is determined such that its lateral stiffness k_{brace} is twice that of the floor stiffness at each level (Lee et al., 2008). As will be discussed later, this stiffness ratio of 2 will be re-examined with additional parametric studies. The steel brace is chosen to have an HSS section, consisting of ASTM A992 steel with a yielding strength of 345MPa.

For the bracing-friction damper system to function properly, however, two additional design verification steps are required: (1) to prevent the unexpected activation of the friction devices during gust winds, and (2) to ensure that the connecting brace has a larger tensile (T_r) and compressive (C_r) capacity than the friction slip load. For the first step, the slip load of the friction damper must exceed the shear forces exerted by the wind loads. In particular, the damper slip load F_i is checked and adjusted if necessary to ensure it is equal or greater than F_{wind_i}, which is 115% of the wind shear at level i. For the second check, the steel brace should not yield before the friction mechanism engages. To achieve this, the slip load F_i is verified and adjusted if it requires to be smaller than the compression resistance of the chosen HSS section.

The overall seismic retrofit design process is illustrated using a flow chart shown in the Figure 4-5, whereas detailed calculations of this design process can be found in Appendix A. The final design of the bracing-friction damper system against $R_d R_o = 5.5$ is summarized in

Table 4-5. The steel braces are designed to maintain linearity during seismic events and are modeled as a part of the bilinear model described in Chapter 3.

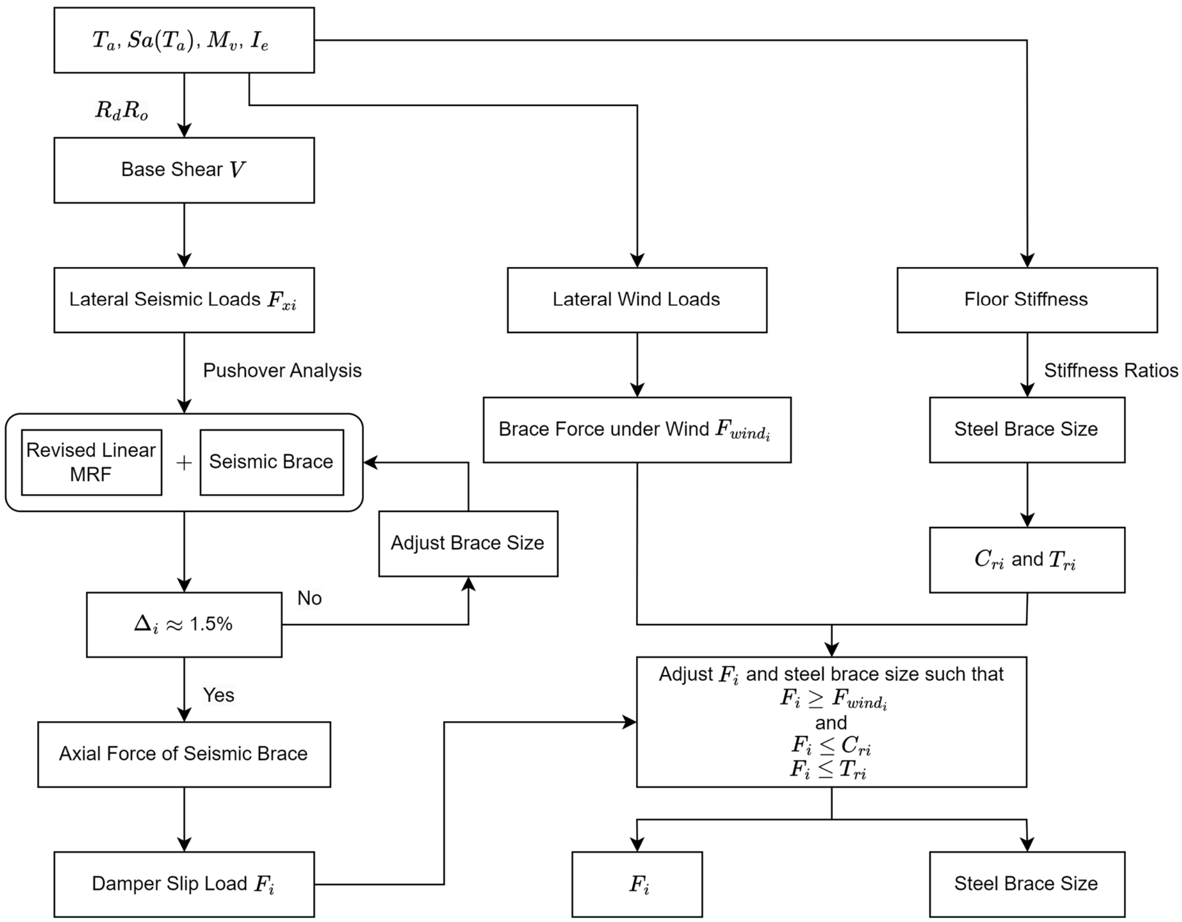

Figure 4-5 Seismic retrofit design process of the friction damper-bracing system

Table 4-5 Friction damper-bracing system design when $R_dR_o = 5.5$

City	Type	Level	Brace Section	Damper Slip Load (kN)
Montreal	Roof	6	139.7 × 139.7 × 4.8	140
	Floor	5	139.7 × 139.7 × 4.8	140
	Floor	4	228.6 × 228.6 × 6.4	400
	Floor	3	228.6 × 228.6 × 6.4	500
	Floor	2	304.8 × 304.8 × 9.5	550
	Floor	1	228.6 × 228.6 × 7.9	580
Vancouver	Roof	6	177.8 × 177.8 × 6.4	340
	Floor	5	177.8 × 177.8 × 6.4	370
	Floor	4	355.6 × 355.6 × 12.7	830
	Floor	3	355.6 × 355.6 × 12.7	980
	Floor	2	457.2 × 457.2 × 15.9	1130
	Floor	1	355.6 × 355.6 × 9.5	1160

4.3. Seismic Upgrades using Concentric Brace

Apart from the friction damper bracing system, steel braces themselves present an alternative solution for seismic retrofitting because of their high stiffness and ease of assembly (Sarno & Elnashai, 2004). A comparison between the two seismic retrofit options (i.e., steel braces with friction dampers versus only steel braces) can help stakeholders with the decision-making process. Therefore, an alternative design of seismic retrofit using concentric braces is proposed. As shown in Figure 4-6, the process of obtaining the brace capacity, B_i, mirrors that of obtaining damper slip force F_i. The steel HSS sections are then selected based on the seismic brace capacity B_i, ensuring each brace member has adequate T_R and C_R. Such design ensures that when the braced frame reaches the targeted lateral drift ratios, the steel braces remain linearly elastic. As the braced frame further deforms, it is anticipated that most of the strength will come from the braces under tension, while the braces under compression will have significantly reduced resistance due to local buckling. The selected concentric braces are shown in Table 4-6.

Table 4-6 Concentric braces selection when $R_d R_o = 5.5$

City	Type	Level	Brace Section
Montreal	Roof	6	127.0 × 127.0 × 9.5
	Floor	5	152.4 × 152.4 × 9.5
	Floor	4	152.4 × 152.4 × 12.7
	Floor	3	152.4 × 152.4 × 15.9
	Floor	2	177.8 × 177.8 × 9.5
	Floor	1	177.8 × 177.8 × 12.7
Vancouver	Roof	6	177.8 × 177.8 × 6.4
	Floor	5	203.2 × 203.2 × 7.9
	Floor	4	228.6 × 228.6 × 7.9
	Floor	3	228.6 × 228.6 × 9.5
	Floor	2	254.0 × 254.0 × 7.9
	Floor	1	254.0 × 254.0 × 9.5

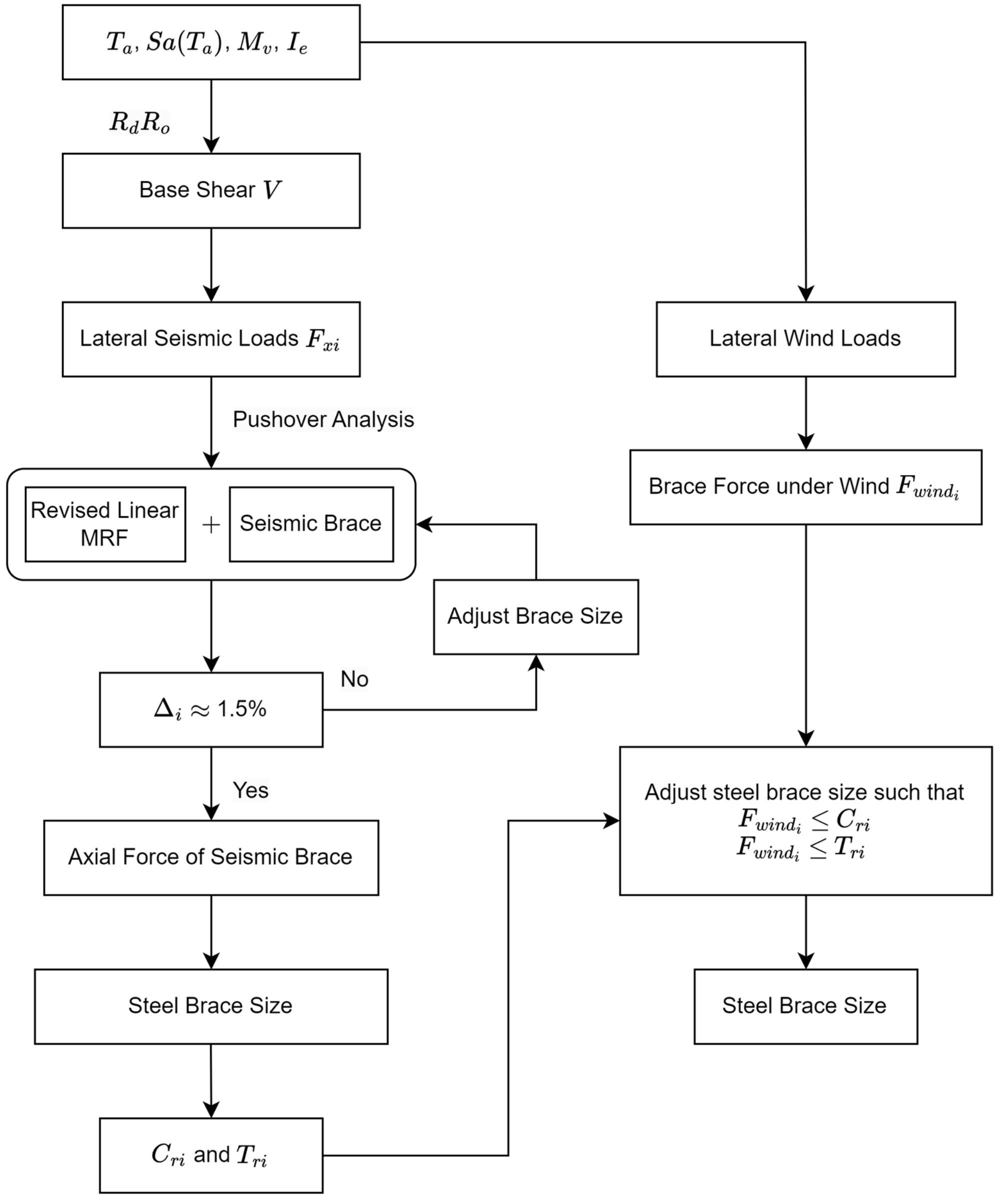

Figure 4-6 Seismic retrofit design process of the concentrically braced system

The braced frame dissipates seismic energy through inelastic deformations dominated by tensile yielding of the brace, brace buckling, and post-buckling deformation (Shen et al., 2017). To accurately capture the inelastic responses of steel braces under different levels of seismic shaking, a nonlinear model is adopted (Padilla-Llano et al., 2015). As shown in Figure 4-7, this model simulates steel braces and incorporates the effects of local buckling deformations and hysteretic energy dissipation. The model parameters are presented in a generalized form as functions of the member cross-sectional slenderness λ. These parameters are directly applicable to the Pinching 4 Material model in OpenSees. Figure 4-8 illustrates a schematic of the steel MRFs with added concentric braces.

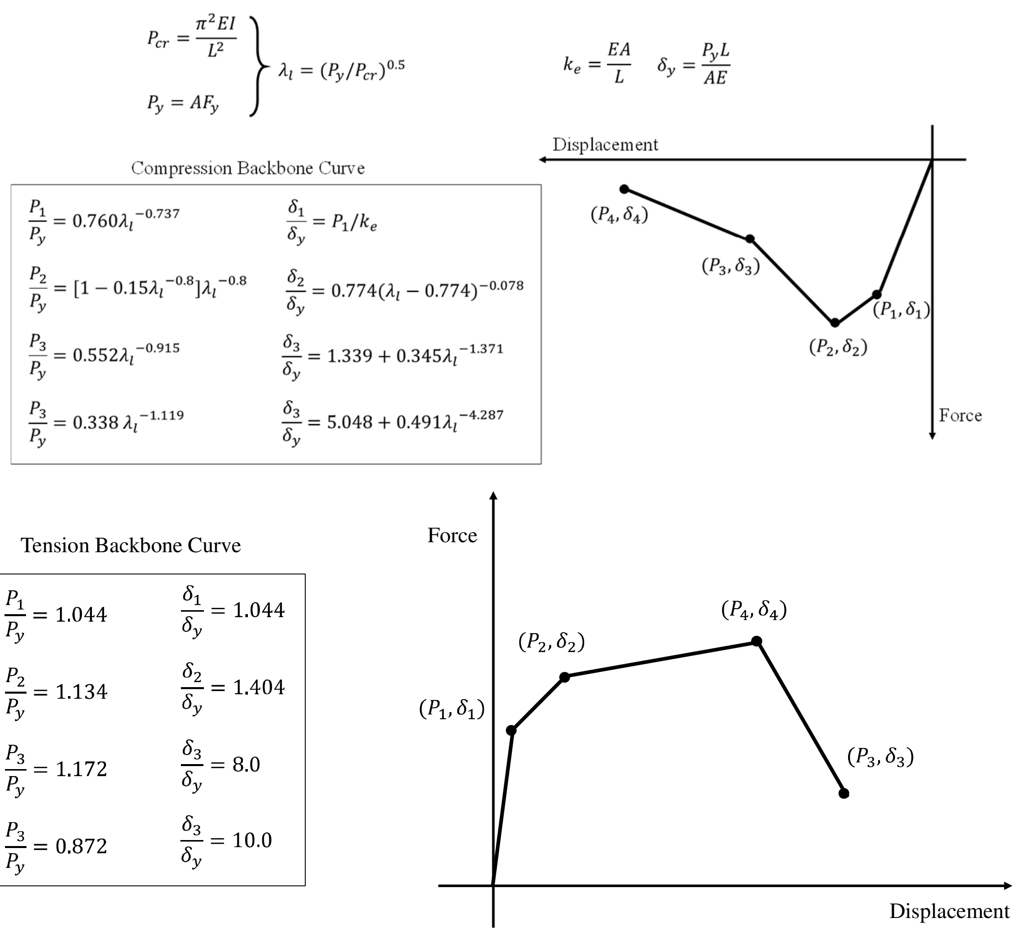

Figure 4-7 Concentric brace model parameters and backbone curves

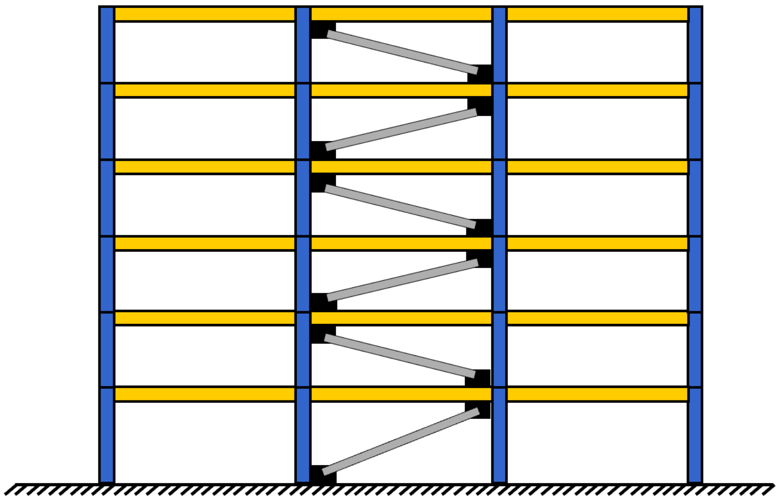

Figure 4-8 Steel MRF retrofitted with concentric braces

Chapter 5. Seismic Hazard Analysis and Ground Motion Selection

5.1. Selection of Intensity Measure

An intensity measure (IM) quantifies the intensity of ground motion and serves as a critical linkage between the seismic hazard and structural responses of the given structure (Baker & Cornell, 2005; Padgett et al., 2008). A proper selection of IM is essential to the risk-based seismic evaluations. In this study, seismically retrofitting the original buildings will change the corresponding fundamental periods. Specifically, the fundamental periods for pre-code and retrofitted structures in Montreal are 2.9 s and 1.1 s, whereas in Vancouver, these periods are 2.4 s and 0.8 s. To consider the period change, an average spectral acceleration $AvgSA(T_{\mathrm{a}})$ is chosen as the IM for the ground motions, where $T_{\mathrm{a}} = 1.3\ s$ is the empirical natural period calculated in Section 4.1.

$$AvgSA(T_a) = \left(\prod_{i=1}^{N} Sa(c_i T_a)\right)^{\frac{1}{N}} \tag{5-1}$$

$AvgSA(T_{\mathrm{a}})$ is computed as the geometric mean of spectral accelerations at the period interval $[0.2 \times T_{\mathrm{a}},\ 2.0 \times T_{\mathrm{a}}]$ with an incremental step of $0.1 \times T_1$, as shown in Equation 5-1. As such, the effect of the period changes due to (1) the installation of the friction devices and (2) structural nonlinearity and seismic damage is captured. Moreover, $AvgSA(T_{\mathrm{a}})$ has shown improved efficiency and sufficiency with respect to the probabilistic seismic demand modeling and seismic fragility assessment of structures (Eads et al., 2015; Ning & Xie, 2022).

5.2. Seismic Hazard Analysis

5.2.1. Overview of Seismicity

Montreal and Vancouver are two densely populated metropolitan areas in Canada, and they are both located in seismic active regions. Eastern Canada lies within a stable continental region within the North American plate, resulting in a comparatively low rate of earthquake activity (Kolaj et al., 2020a). However, despite this stability, the region has witnessed significant and destructive earthquakes in the past. Montreal is part of the Western Quebec Seismic Zone (WQSZ), which constitutes a vast territory that also includes the urban centers of Ottawa and Cornwall (Lamontagne & Ranalli, 2012; Tremblay et al., 2003). The WQSZ is a region characterized by shallow crustal earthquakes and moderate seismicity, which is related to the faults along the St. Lawrence rift system as shaded in Figure 5-1. While the majority of earthquakes within the WQSZ are typically smaller than magnitude 4.5, at least three significant earthquakes have occurred in the past (Lamontagne et al., 2008). On September 16, 1732, an earthquake occurred in Montreal with a magnitude of 5.8. This event resulted in severe damage to approximately 300 houses. In 1935, the area of Temiscaming was shaken by an earthquake of magnitude 6.2. In 1944, an earthquake of magnitude 5.6, located between Cornwall, Ontario, and Massena caused damage evaluated at two million dollars at the time.

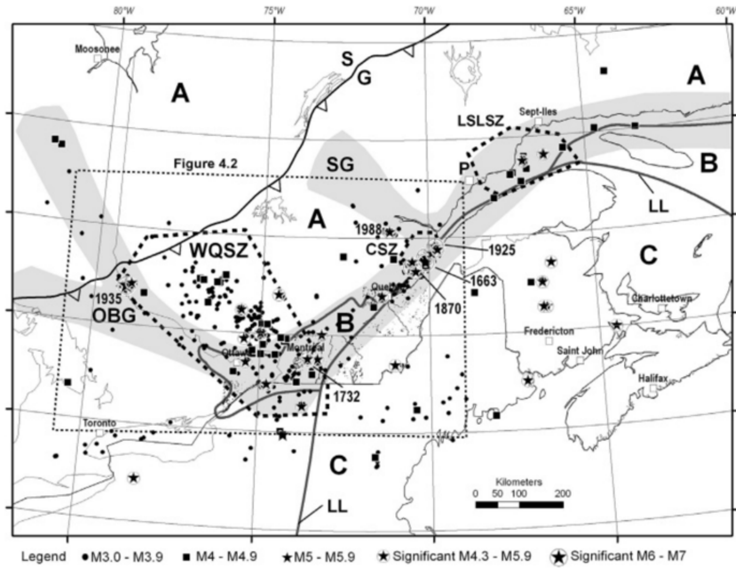

Figure 5-1 Seismicity Map of Eastern Canada (Lamontagne & Ranalli, 2012)

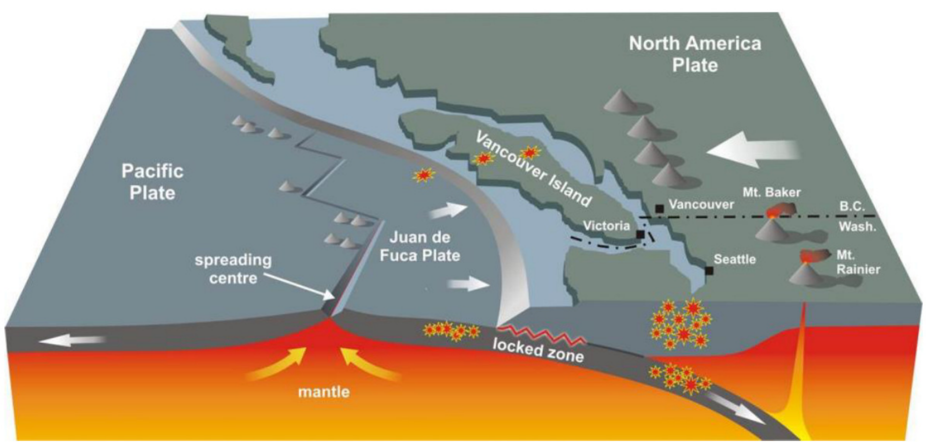

Figure 5-2 Tectonic setup and the earthquake mechanism on the West Coast of Canada (Rogers et al., 2015)

On the other hand, the Pacific Coast stands as the most earthquake-prone region in Canada, where the Geological Survey of Canada documents and locates over 1000 earthquakes annually (Earthquake Canada, 2023). Vancouver is located on the western coast of Canada and near the boundary of the North American Plate and the smaller Juan de Fuca Plate (Rogers et al., 2015). The subduction of the oceanic Juan de Fuca Plate beneath the continental North America Plate at a rate of approximately 2 to 5 cm per year off the west coast of Vancouver Island forms the Cascadia subduction zone. The tectonic setup, as shown in Figure 5-2, represents a unique convergence zone that generates three distinct types of earthquakes:

1. Crustal earthquakes occur within the continental crust of the North American plate. These shallow earthquakes occur near the surface and are often unrelated to plate boundaries. Because of their shallow depth, they possess significant destructive potential. These seismic events are primarily concentrated in two main areas: the Puget Sound region of Washington State and the southernmost region of the Strait of Georgia in British Columbia. An example of such seismic activity is the devastating 1946 Vancouver Island earthquake, registering a magnitude of 7.3 (Hodgson, 1946).

2. Subcrustal earthquakes occur within the subducting Juan de Fuca Plate. These earthquakes typically occur at depths of about 50-60 km under Georgia Strait and Puget Sound. While they usually cause less damage than shallower earthquakes, they are felt over a larger area. Examples of subcrustal earthquakes include the 1949 and 1965 Puget Sound Earthquakes and the 2001 Nisqually Earthquake, all ranging between magnitudes of 6.5 and 7.0 (Miller, 2001; Thorsen, 1986).

3. Subduction earthquakes take place at the interface of the two plates in the Cascadia subduction zone. These earthquakes exhibit an average recurrence

interval of 500-530 years, with the most recent one documented in 1700 (Wang, 2012). The estimated magnitude of the 1700 earthquake was approximately 9.0, resulting in a significant ocean-wide tsunami. Despite their offshore location and relative distance from urban centers, these earthquakes produce long-duration strong shaking over a large area, often lasting several minutes.

5.2.2. Seismic Hazard Disaggregation

In 2020, Natural Resources Canada developed its 6th generation seismic hazard model (SHM6) and subsequently generated a suite of seismic hazard maps covering Canada (Kolaj et al., 2023b, 2023a). The process of disaggregation unbundles the seismic hazard results and has become an important tool for understanding the relative contributions of earthquake sources (Halchuk et al., 2019). Allocating the total hazard based on distance and magnitude closes the gap between the thousands of earthquakes considered in hazard models and the specific scenario earthquakes needed for engineering purposes. Performing disaggregation across multiple periods helps determine if one source consistently dominates and clarifies whether more than one design earthquake scenario is necessary.

This study performs disaggregation of the SHM6 seismic hazard results for Vancouver and Montreal to analyze the relative contributions of earthquake sources, including distance, magnitude, and contribution. The disaggregation was carried out using the SHM6 OpenQuake platform (Pagani et al., 2014), with detailed 2% in 50 years results presented for Montreal and Vancouver in Figure 5-3 and Figure 5-4, respectively.

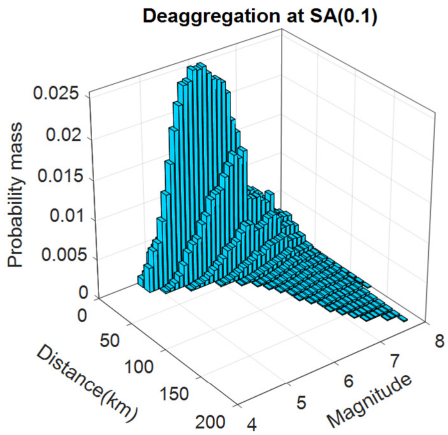

Earthquake type	$\bar{M}$	$\bar{R}$ (km)
Crustal	6.33	20.51

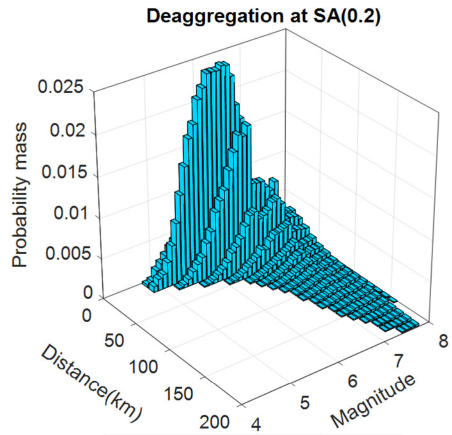

Earthquake type	$\bar{M}$	$\bar{R}$ (km)
Crustal	6.41	23.17

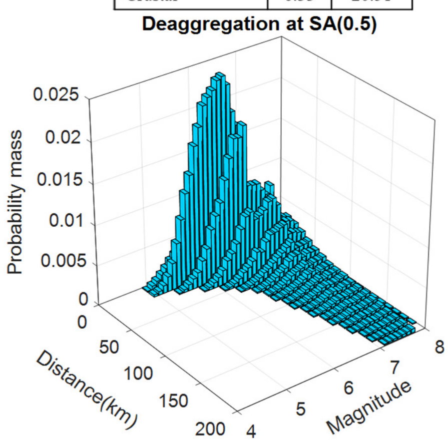

Earthquake type	$\bar{M}$	$\bar{R}$ (km)
Crustal	6.65	29.79

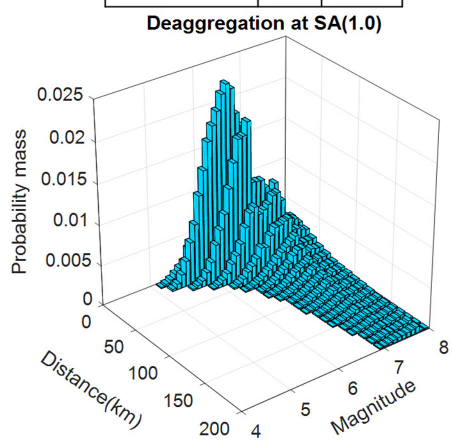

Earthquake type	$\bar{M}$	$\bar{R}$ (km)
Crustal	6.71	33.29

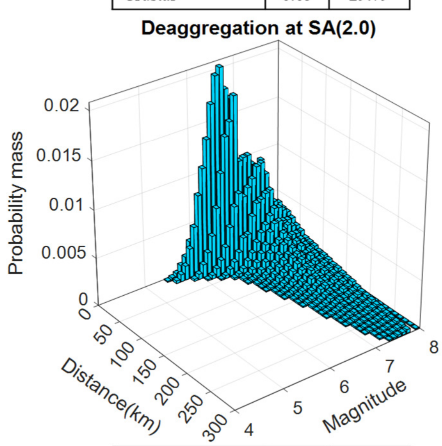

Earthquake type	$\bar{M}$	$\bar{R}$ (km)
Crustal	6.94	49.19

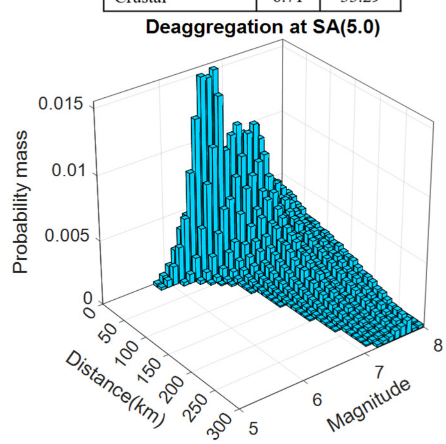

Earthquake type	$\bar{M}$	$\bar{R}$ (km)
Crustal	7.01	56.33

Figure 5-3 Seismic disaggregation for Montreal

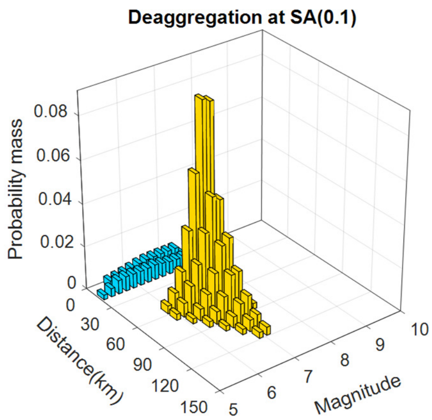

Earthquake Type	$\bar{M}$	$\bar{R}(km)$	Contribution
Crustal	6.42	10.50	0.13
In-slab	6.87	65.03	0.81
Interface	N/A	N/A	0

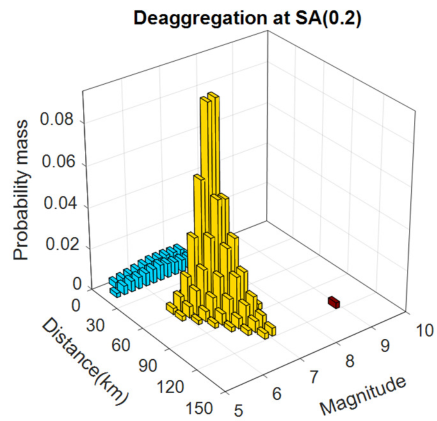

Earthquake Type	$\bar{M}$	$\bar{R}(km)$	Contribution
Crustal	6.50	10.32	0.12
In-slab	6.89	64.94	0.82
Interface	8.90	115.00	0

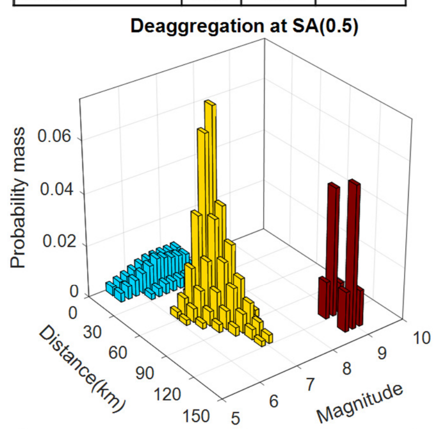

Earthquake Type	$\bar{M}$	$\bar{R}(km)$	Contribution
Crustal	6.61	12.48	0.19
In-slab	6.95	64.91	0.57
Interface	8.90	129.17	0.18

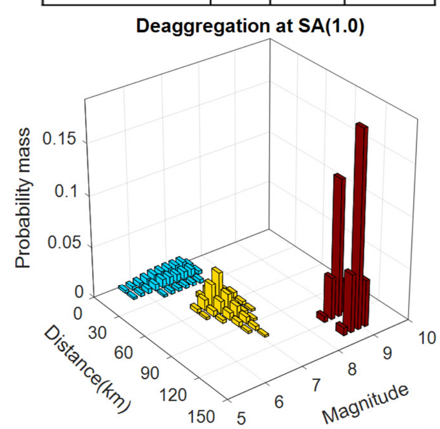

Earthquake Type	$\bar{M}$	$\bar{R}(km)$	Contribution
Crustal	6.73	11.95	0.14
In-slab	7.04	62.81	0.20
Interface	8.89	131.60	0.61

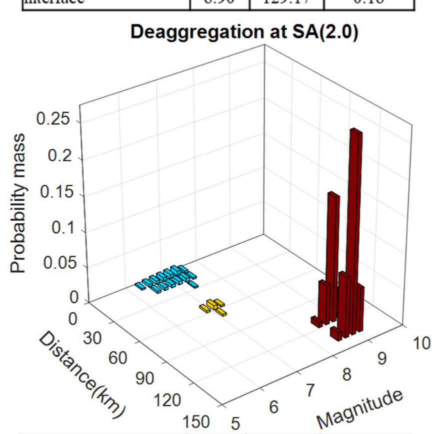

Earthquake Type	$\bar{M}$	$\bar{R}(km)$	Contribution
Crustal	6.98	9.82	0.06
In-slab	7.29	111.52	0.02
Interface	8.87	132.89	0.88

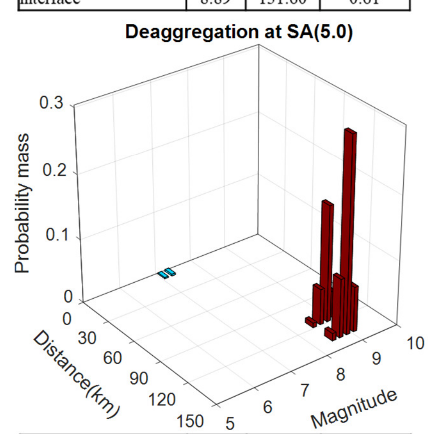

Earthquake Type	$\bar{M}$	$\bar{R}(km)$	Contribution
Crustal	7.22	5.00	0
In-slab	7.90	275.00	0
Interface	8.87	134.29	0.97

Figure 5-4 Seismic disaggregation for Vancouver

5.2.3. Seismic Hazard Curves

Seismic hazard data is retrieved from the online Canada seismic hazard tool (Earthquake Canada, 2021), developed in accordance with the SHM6 utilized in NBCC 2020. As depicted in Figure 5-5, the mean annual rates of exceeding given values of the spectral accelerations (Sa) at different natural periods constitute the seismic hazard curves.

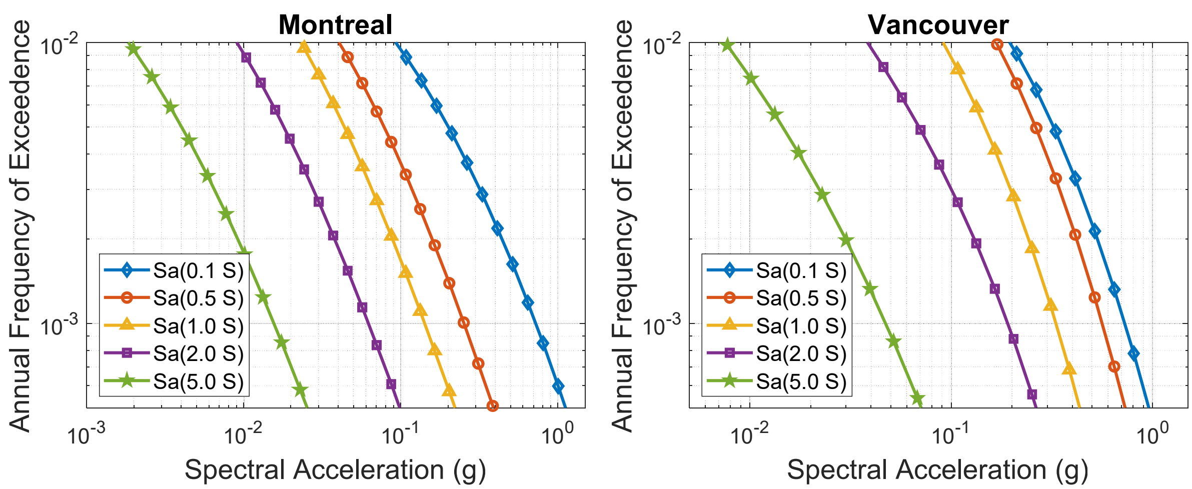

Figure 5-5 Earthquake hazard data (Earthquake Canada, 2021)

For ease of calculation, the hazard data is regressed into a continuous hazard curve using a hyperbolic model (Bradley et al., 2007):

$$\lambda(IM) = \alpha\, exp\left[\beta\left(ln\left(\frac{IM}{\gamma}\right)\right)^{-1}\right] \qquad 5\text{-}2$$

where α, β, and γ are regression constants. The associated hazard data for spectra accelerations at $T_a = 1.3\ s$ is obtained by a logarithmic interpolation between the regressed hazard curves of $Sa(1.0)$ and $Sa(2.0)$ in both cities. In Montreal, the conversion of the hazard curve intensity measure from spectral acceleration to average spectral acceleration involves the following steps: 1. Seismic hazard disaggregation is performed at a specific return period and T_a to determine the mean seismic scenario, characterized by magnitude ($\bar{M}$) and distance ($\bar{R}$). 2. The conditional mean spectrum for this return period is constructed using the method described by Baker (2011), which will be discussed in detail in the next section. The associated spectral acceleration values at periods from $0.2T_a$ to $2T_a$ are determined. 3. The average spectral acceleration values are then computed from these spectral accelerations using Equation 5-1. This results in a set of average spectral acceleration values paired with their corresponding return periods. By repeating this calculation for different return periods, a hazard curve of $AvgSA(T_{\mathrm{a}})$ is generated. For Vancouver, a similar approach is adopted. However, due to the presence of three types of earthquakes, the process involves additional steps: 4. The hazard curve of $AvgSA(T_{\mathrm{a}})$ is first individually analyzed and obtained for each type of earthquake, following the steps outlined previously. Based on the seismic disaggregation results, which attribute contributions of 11% to crustal earthquakes, 13% to subcrustal earthquakes, and 75% to subduction earthquakes, the individual hazard curves are then combined based on these contributions to produce the total hazard curve. The final hazard curves, reflecting the contributions of earthquake types, are shown in Figure 5-6.

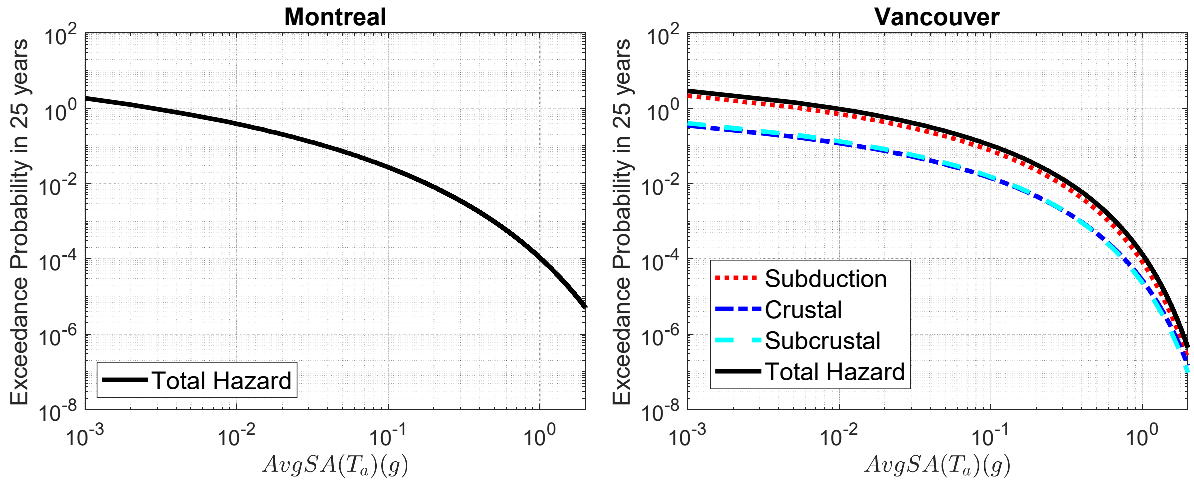

Figure 5-6 Seismic hazard curves

5.3. Ground Motion Selection

5.3.1. Ground Motion Selection based on Conditional Mean Spectrum

The CMS has been selected as the target spectra for selecting and scaling ground motions. The CMS is conditioned on the occurrence of a specific target spectral acceleration value at the period of interest (Baker, 2011). It provides an estimate of the distribution, including the mean and standard deviation, of the response spectrum. This spectrum exhibits a peak at the period used for conditioning and gradually decays to lower amplitudes at periods other than the conditioning period. In contrast with the results obtained from using a UHS, which conservatively assumes that large-amplitude spectral values will occur at all periods within a single ground motion, the adoption of the CMS as a target spectrum offers a more realistic representation of seismic inputs. The process for deriving the CMS can be presented as a four-step procedure: 1. Determine the target spectral acceleration (Sa) at a given period (T^*) and the associated magnitude (M), distance (R) and epsilons (ε) of contributing earthquakes. The M, R, and $\varepsilon(T^*)$ values are taken as the mean M, R, and $\varepsilon(T^*)$ from the results of seismic disaggregation. 2. Compute the mean and standard deviation of the response spectrum, given M and R. These terms are calculated with the ground motion models. 3. Compute ε at other periods, given $\varepsilon(T^*)$. The conditional mean ε at other periods can be expressed as $\varepsilon(T^*)$ multiplied by the correlation coefficient between the ε values at the two periods. 4. Compute the CMS using the mean and standard deviation in Step 2 and the conditional ε values from the step 3.

The conditioning period in the first step is frequently chosen as the fundamental period of the original structure, T_1. However, the structures under examination typically exhibit sensitivity to excitations across a spectrum of periods, including the higher mode effect and period elongation effects associated with the nonlinear behavior (Lin et al., 2013). To account for changes in periods, ASCE 7-16 (2017) recommends selecting a range of conditioning periods, with a lower limit of $0.2T_1$ and upper limit of $2T_1$. Consequently, the initial selected range comprises four conditioning periods based on the pre-code structure ($0.2T_1$, $0.4T_1$, T_1, and $1.5T_1$) (Uribe et al., 2018). Given that the retrofitted structure exhibits a significantly shorter fundamental period $\left(T_{1\,retrofit}\right)$ in comparison to the original structure, an extra conditioning period of $0.2T_{1\,retrofit}$ is introduced to address the difference in fundamental periods.

A software tool developed by Baker is used to automate the ground motion selection procedure (Jayaram et al., 2011). The tool is supplied with seismic disaggregation results and ground motion prediction equations selected based on regional characteristics and specific earthquake (Atkinson & Boore, 2006; Boore et al., 2014; Parker et al., 2022). Subsequently, it selects and scales a set of ground motions from the ground motion database while minimizing the spectral shape error concerning each of the target CMS. For crustal earthquakes in Montreal, 200 ground motions are selected from the PEER NGA-West2 ground motion database (Ancheta et al., 2014), with 40 motions allocated for each of the five conditional periods. In Vancouver, the selection process involves choosing 40 motions for each of the five conditional periods as well. However, similar to the approach used for developing seismic hazard curves, the number of records selected for each conditional period is based on the contribution of each type of earthquake, as determined by the seismic hazard disaggregation results. This distribution is detailed in Table 5-1. Crustal earthquakes in Vancouver are selected from the PEER NGA-West2 database, while subcrustal and subduction earthquakes are obtained from the NGA-Subduction database (Ahdi et al., 2017).

Table 5-1 Contribution of earthquake types in ground motion selection in Vancouver

T **(sec)**	**Contribution**			**Number of Ground Motions**		
	Crustal	**Subcrustal**	**Subduction**	**Crustal**	**Subcrustal**	**Subduction**
0.2	0.12	0.81	0.00	5	35	0
0.5	0.19	0.58	0.17	8	24	8
1.0	0.15	0.22	0.59	6	9	25
2.4	0.05	0.02	0.89	4	0	36
3.6	0.03	0.01	0.93	5	0	35

The selected ground motions for Montreal and Vancouver are shown from Figure 5-7 to Figure 5-10. The distribution of the 200 selected ground motions for Vancouver is then shown in Figure 5-11.

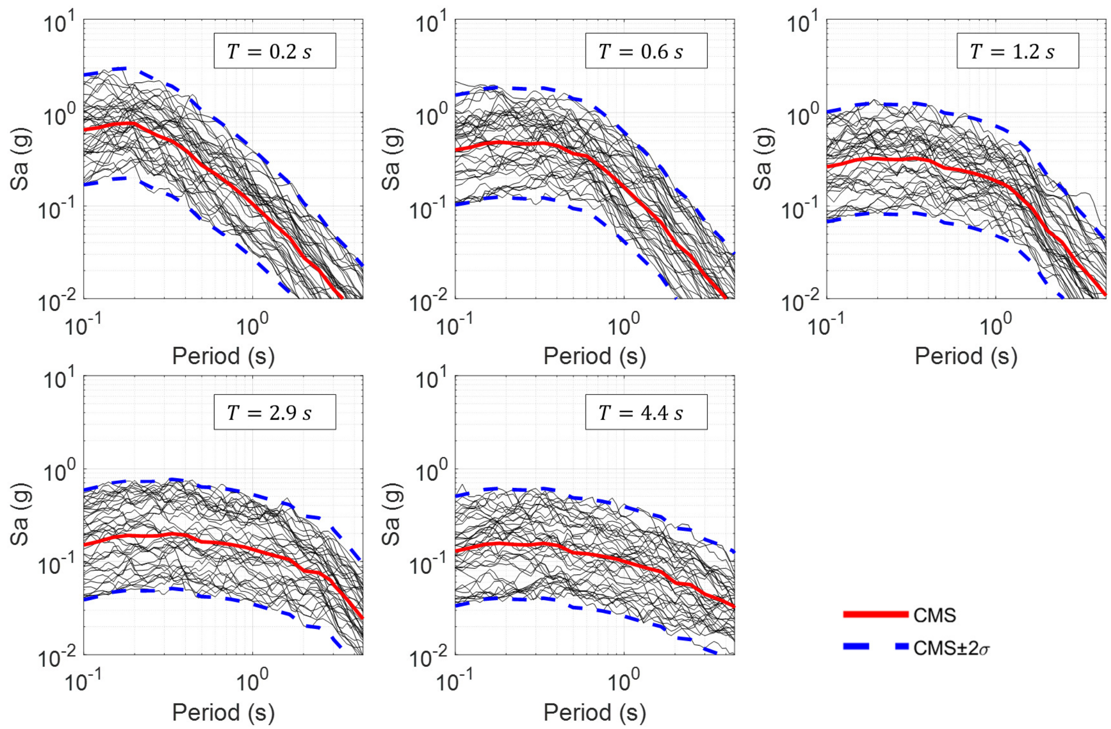

Figure 5-7 Ground motion selection for crustal earthquakes in Montreal

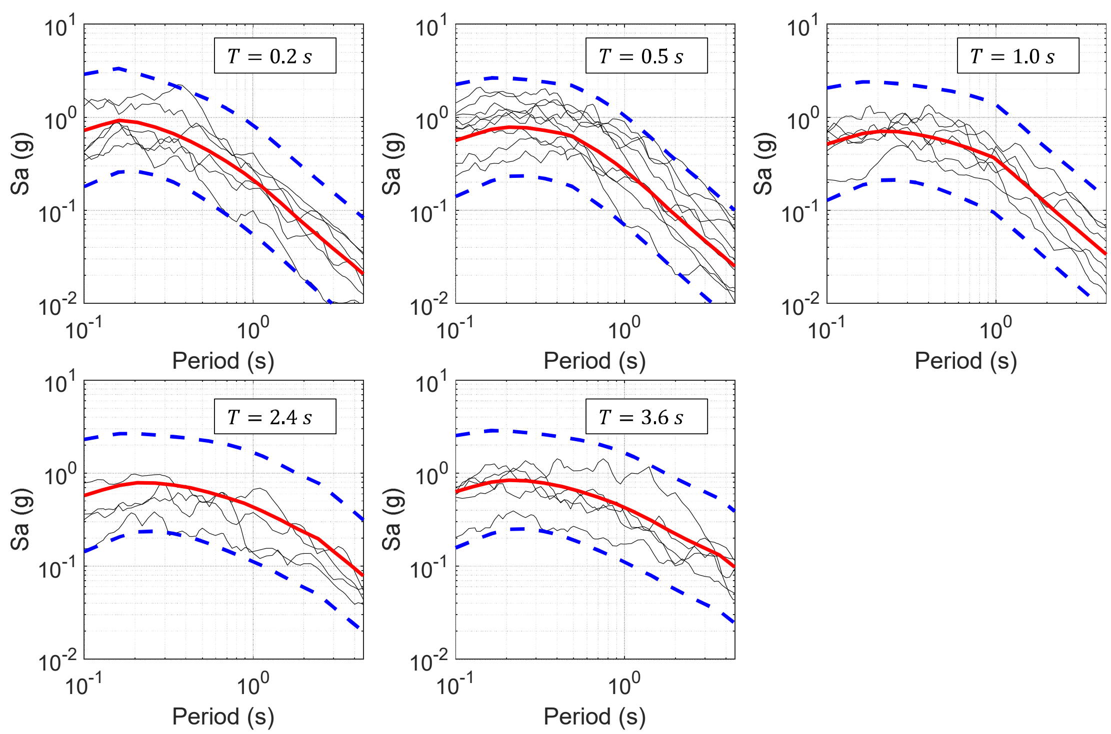

Figure 5-8 Ground motion selection for crustal earthquakes in Vancouver

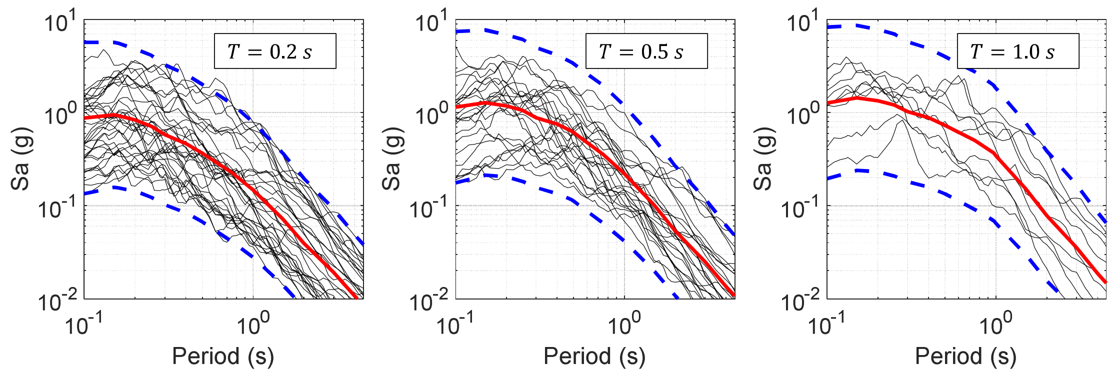

Figure 5-9 Ground motion selection for subcrustal earthquakes in Vancouver

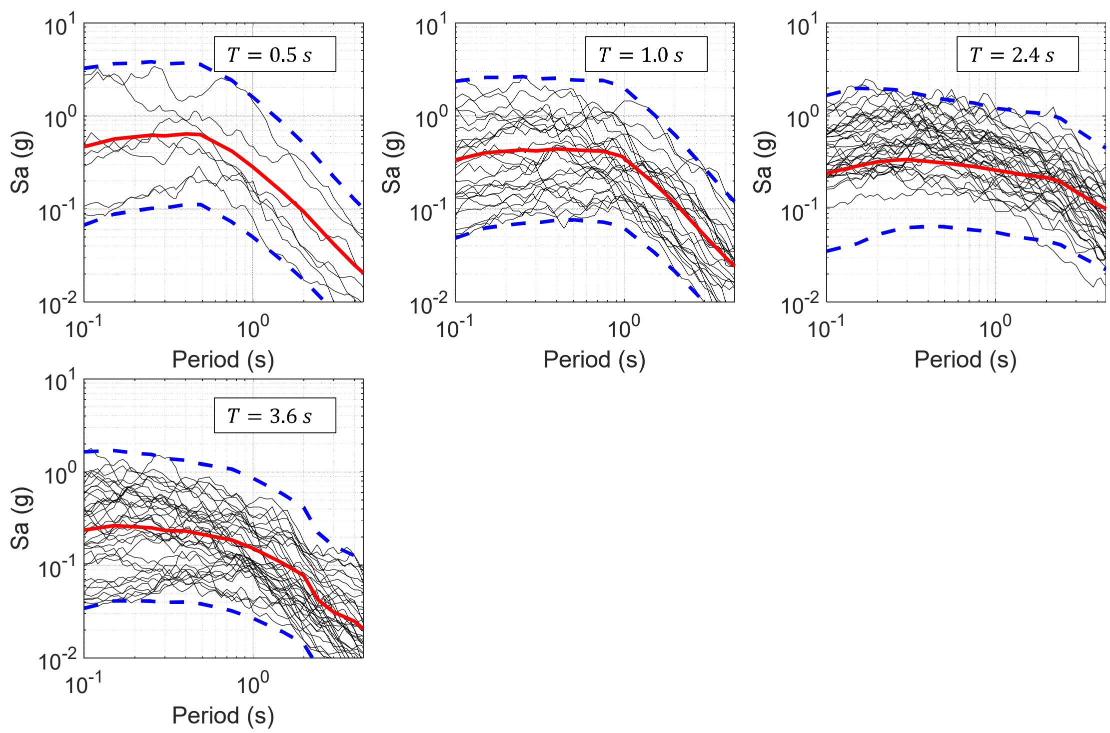

Figure 5-10 Ground motion selection for subduction earthquakes in Vancouver

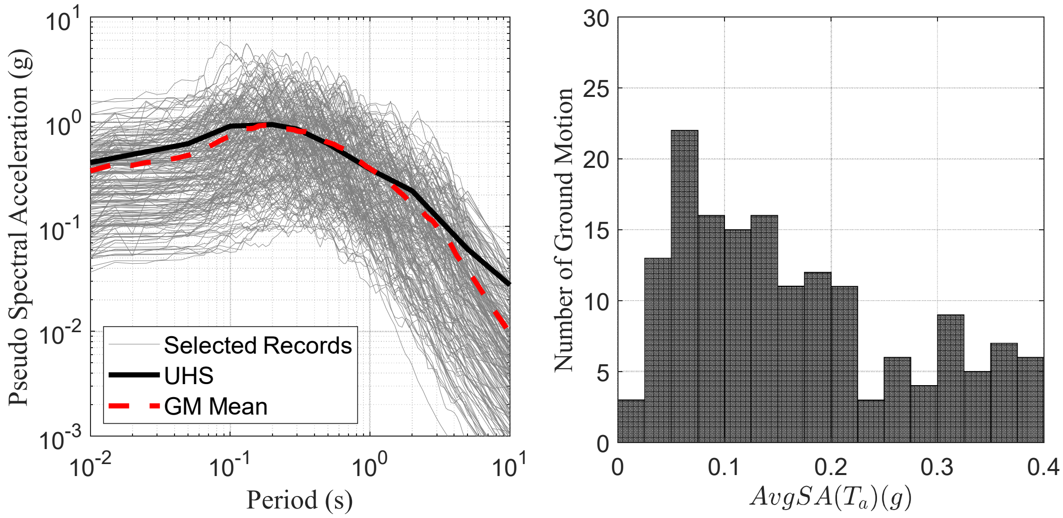

Figure 5-11 Selected ground motions for Vancouver

5.3.2. Additional Synthetic Ground Motions for Montreal

In complement to the 200 recorded ground motions chosen in Montreal, an additional set of 40 strong synthetic ground motions is selected based on the study by Atkinson (2009). The generation of these synthetic records follows the stochastic finite-fault method, replicating the seismological attributes of anticipated motions in eastern Canada in both frequency content and duration. The distribution of all 240 selected ground motions for Montreal is shown in Figure 5-12.

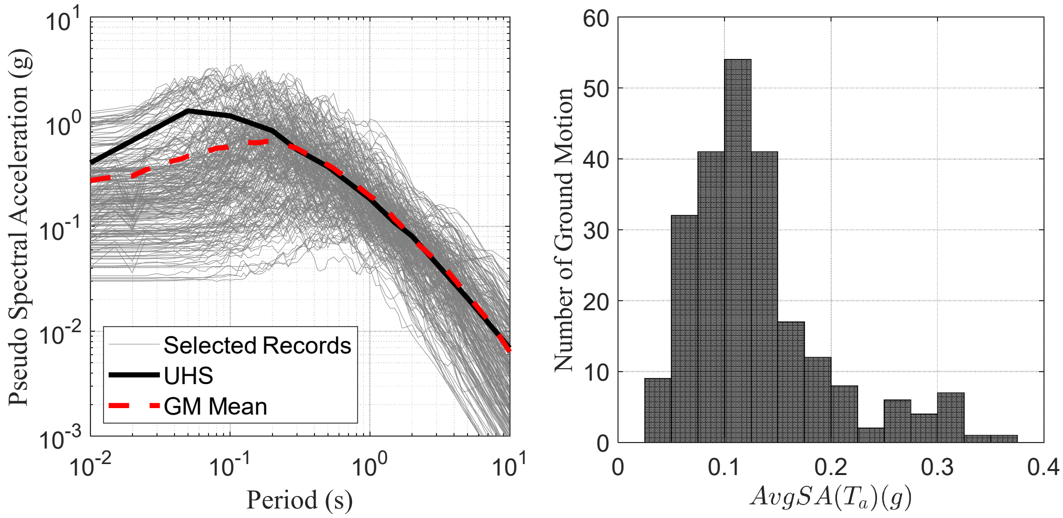

Figure 5-12 Selected ground motions for Montreal

Chapter 6. Probabilistic Seismic Response Analysis

6.1. Mean Responses of Seismic Demands

Nonlinear response history analyses are conducted on different building cases (i.e., the pro-code as the original frame, the ones retrofitted with friction damper braces, and the one retrofitted with the concentric brace) in both Montreal and Vancouver when subjected to the selected ground motions. Figure 6-1 depicts the mean responses of the seismic demand parameter, peak floor acceleration (PFA), under the selected ground motions. In Montreal, the frames retrofitted with friction devices experience higher acceleration compared to the pre-code frame in the first five levels. The PFA increases as $R_d R_o$ decreases across all stories. The frame retrofitted with concentric braces show a higher PFA than those with friction devices when $R_d R_o = 5.5$. In Vancouver, a similar pattern is observed for frames retrofitted with friction devices, which exhibit greater acceleration than pre-code frame in the first five levels, with acceleration increasing as $R_d R_o$ decreases across all levels. Frames retrofitted with concentric braces display a PFA comparable to that of frames with friction devices in the first four levels but show noticeably higher PFA in the upper two levels.

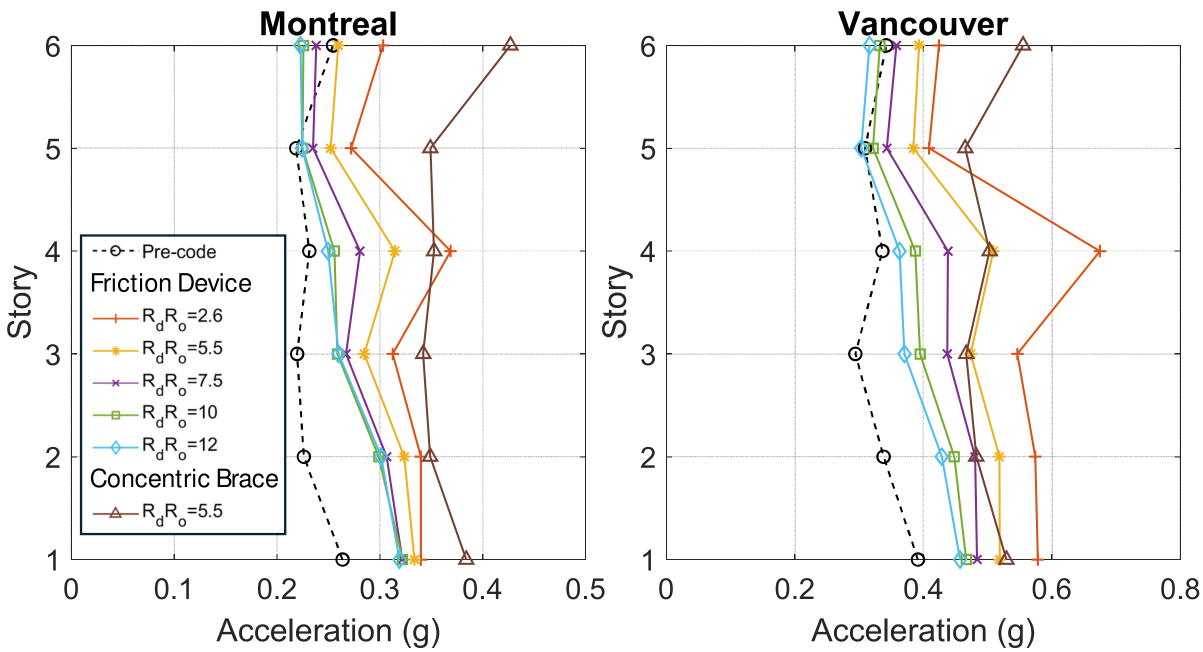

Figure 6-1 Mean seismic demand responses of peak floor acceleration

Figure 6-2 depicts the mean responses of inter-story drift ratio (IDR). In Montreal, a significant reduction in IDR is observed for frames retrofitted with friction devices. In the first four levels, IDR is reduced more markedly as R_dR_o decreases. However, this trend reverses in the upper two levels, where the smallest IDR is achieved at larger values of R_dR_o. Frames retrofitted with concentric braces reduce the IDR to a lesser extent compared to friction devices when $R_dR_o = 5.5$, but the difference across the stories remains consistent. In Vancouver, the frames retrofitted with friction devices significantly reduced IDR in all levels, except on the fifth floor when $R_dR_o = 2.6$. Frame retrofitted with concentric braces achieve a slightly smaller reduction in IDR compared to those with friction devices, except that there is almost no reduction observed on the fifth floor.

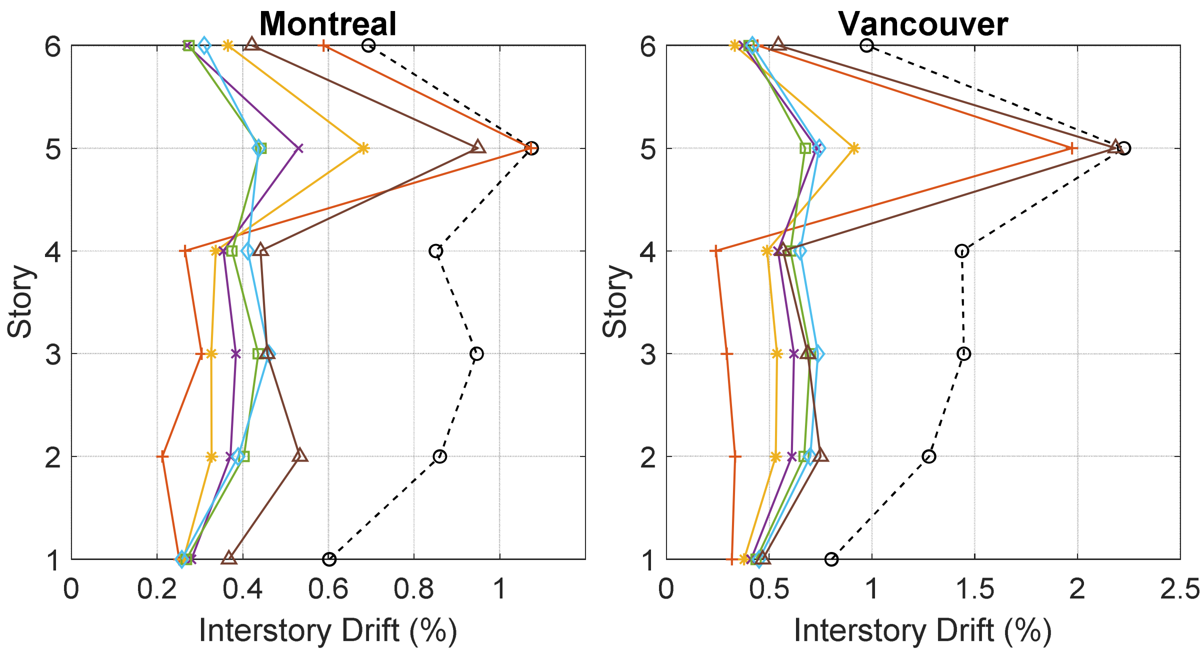

Figure 6-2 Mean seismic demand responses of inter-story drift ratio

6.2. Response Histories of Individual Structural Components

The time history responses of individual structural components within the structures were analyzed using response recorders in OpenSees. For instance, Figure 6-3 illustrates the response of a pre-code Vancouver structure subjected to one ground motion record. The hysteresis behavior of a selected column, beam, and connection within this structure is presented. These moment rotation curves reveal that the structural members exhibit nonlinear behavior, which leads to seismic damage.

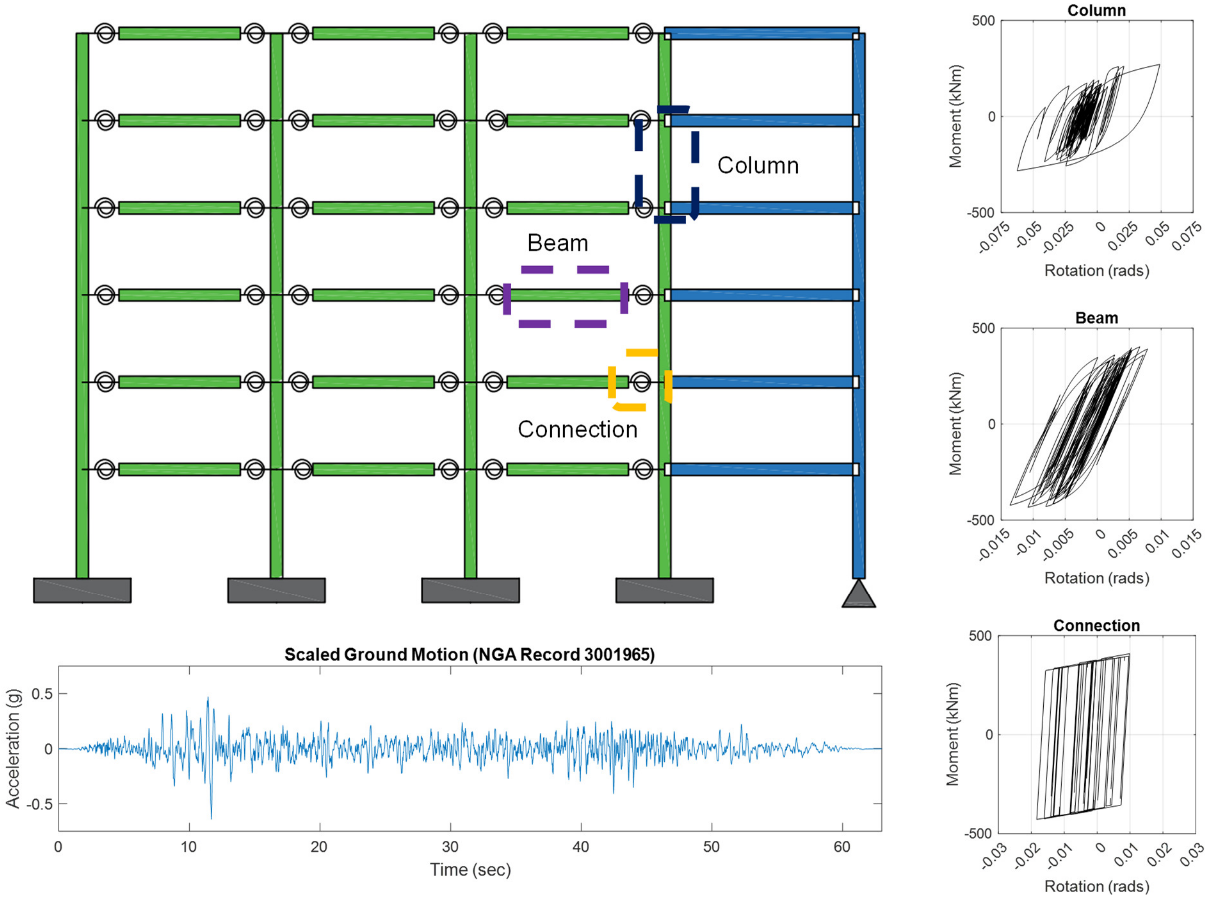

Figure 6-3 Time history responses of selected column, beam, and connection in pre-code Vancouver structure

The same ground motion was applied to excite the frame retrofitted by friction dampers, as shown in Figure 6-4. The hysteresis behavior of the column, beam, and connection at the same locations is compared with those of the pre-code frame, revealing that all components in the friction-retrofitted frame remain linear elastic throughout the seismic event. The force-displacement curve of the friction damper demonstrates stable, energy-dissipating hysteresis loops with relatively small displacements. When the same ground motion is applied to the frame retrofitted with concentric braces, shown in Figure 6-5, the beam and column remain linear elastic, but the connection exhibits nonlinear behavior. The hysteresis behavior of the concentric brace in this frame shows excessive deformation and buckling. Comparatively, the frame retrofitted with friction dampers better protect the structural components and experience less deformation than that retrofitted with concentric braces.

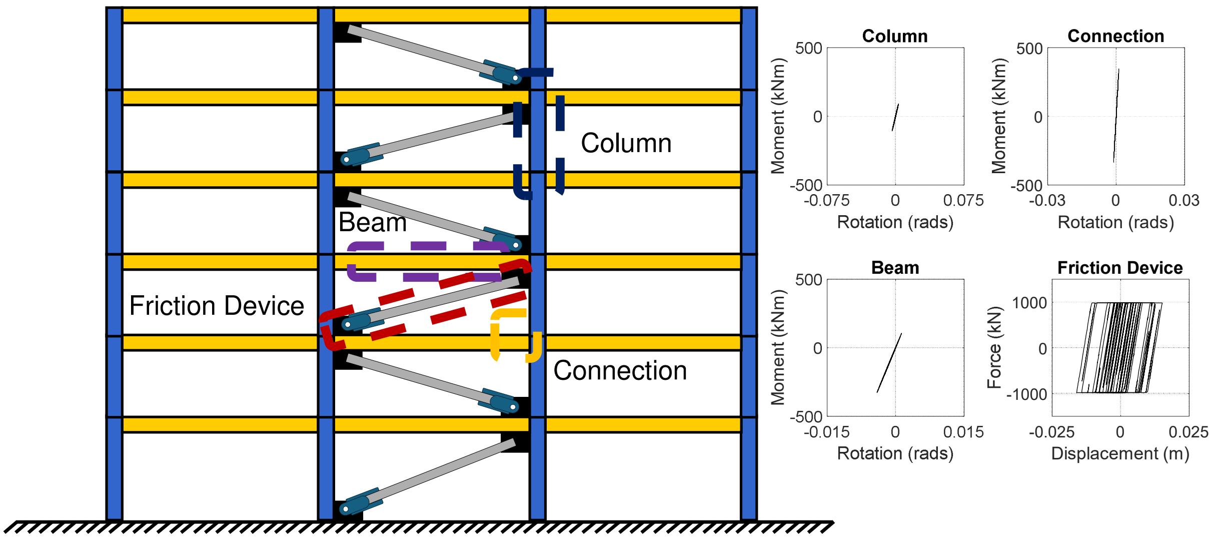

Figure 6-4 Hysteresis of structural components in the frame retrofitted with friction dampers

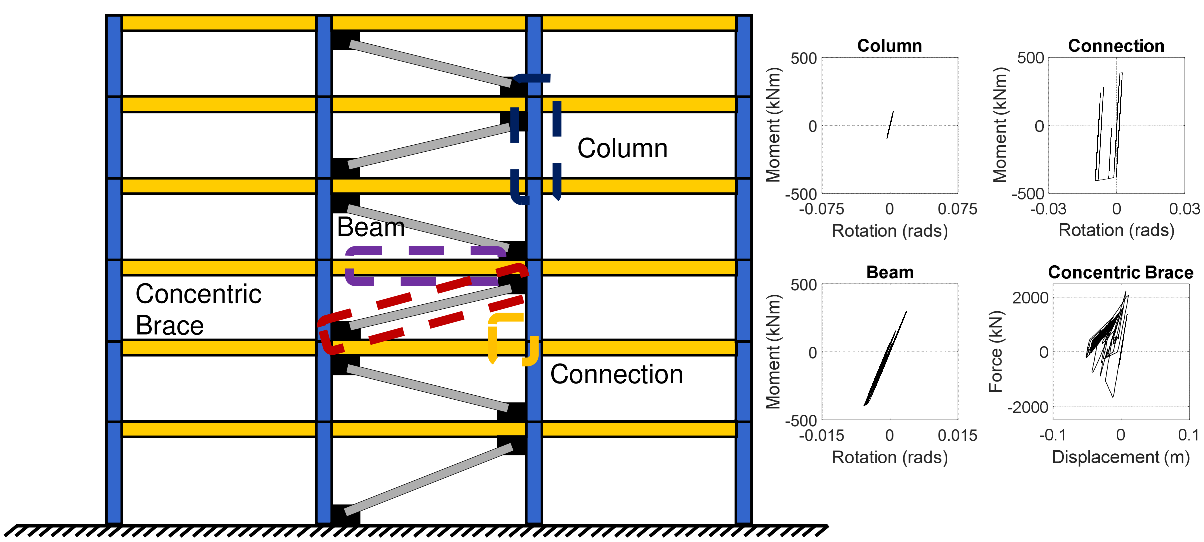

Figure 6-5 Hysteresis of structural components in the frame retrofitted with concentric braces

The analysis of hysteresis indicates that yielding in the connections is the earliest and most prevalent damage mechanism. To further investigate this, a time history response for all the beam-column connections of the Montreal pre-code building under the same ground motion record is analyzed, as shown in Figure 6-6. The damage pattern in these connections is consistent with the first mode damage. The connections in the lower levels experience more pronounced nonlinear damage, whereas those in the upper two floors largely remain linear.

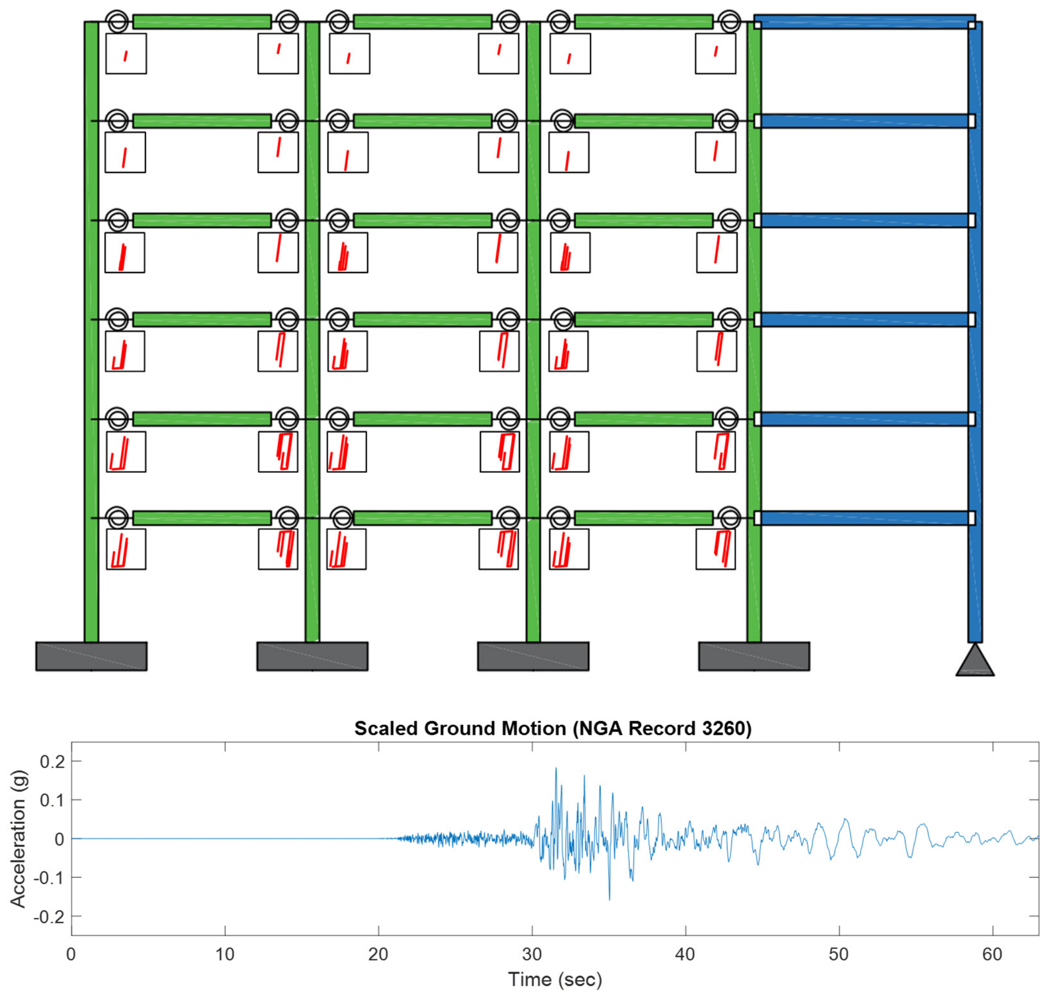

Figure 6-6 Hysteresis of connections in Montreal pre-code building

To gain a deeper understanding of the damage and the effectiveness of seismic retrofits, the hysteresis of the left connection on the first floor-interior bay of both the pre-code and retrofitted frames is examined under the full suite of ground motions in Montreal and Vancouver, respectively. The hysteresis responses of the selected connection in each frame are overlapped in Figure 6-7 to illustrate the extent of the damage in the components. In Montreal, the connection hysteresis for the pre-code structure predominantly clusters in the nonlinear range. This clustering is notably reduced in frames retrofitted with friction dampers and concentric braces, indicating that both retrofit methods effectively prevent connections from entering the nonlinear stage for a number of ground motion records. A similar trend is observed in Vancouver, where the hysteresis clusters are larger in the pre-code structures compared to the retrofitted frames. Furthermore, it is evident that the frame retrofitted with friction dampers better mitigates rotational demands compared to the frame retrofitted with concentric braces.

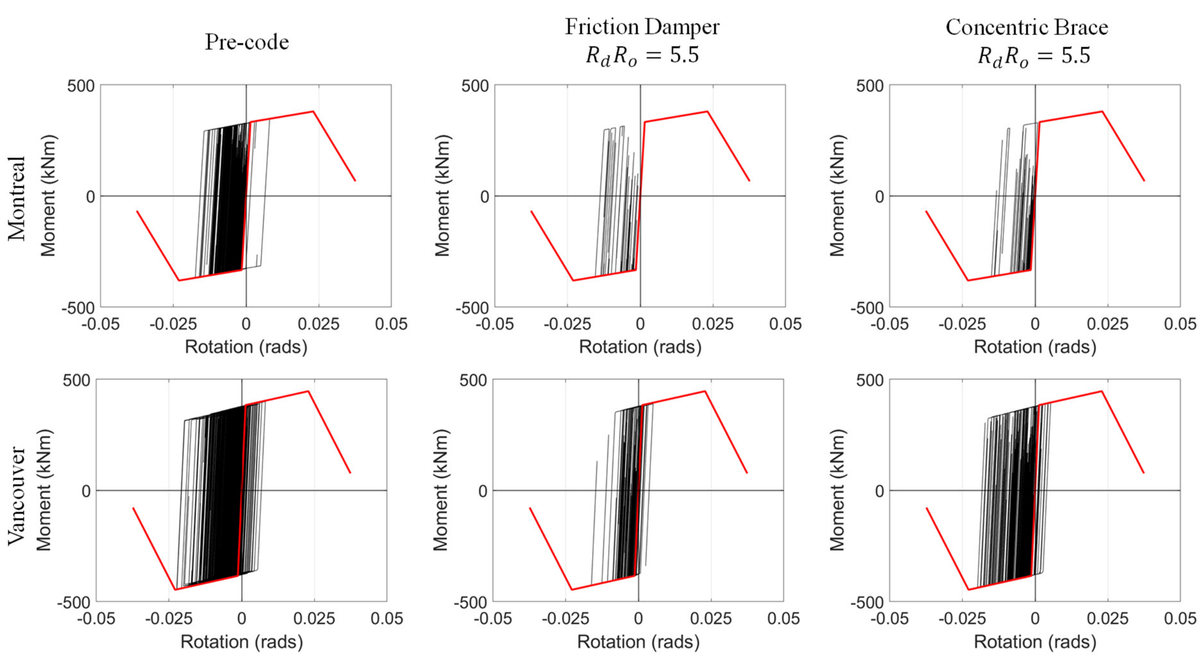

Figure 6-7 Hysteresis of the left connection in the first level interior bay

6.3. Demand to Yielding Capacity Ratio

In evaluating the seismic design level of buildings, two key parameters are demand and capacity. Demand consists of those when all external loads imposed on the building structure, including dead loads and earthquake forces. Capacity refers to the building's ability to withstand these demands. The objectives of demand and capacity analysis are to ensure that the structure has sufficient capacity to withstand anticipated loads and identify potential weakness and failures when demands exceeds capacity (Jaaz et al., 2021). The demand to yielding capacity ratio (DCR) is assessed for beams, columns, and connections to evaluate their performance under seismic loading. This ratio compares the demand imposed on these components with their corresponding yielding capacity. To prevent structural failure, the DCR must be maintained at or below one. For beams and connections, the capacities are defined as yielding moment. For column sections, it is related to the interaction between axial loading and uniaxial bending, as outlined below:

$$DCR_{column} = \frac{C_f}{C_r} + U_{1x}\frac{M_{fx}}{M_{rx}} \tag{6-1}$$

Figure 6-8 presents the distribution of the DCRs for columns in the first-floor interior bay across different structural configurations in both Vancouver and Montreal. The analysis shows that columns in retrofitted structures exhibit lower median DCRs compared to those in pre-code structures, indicating better performance and a lower likelihood of exceeding yielding capacity under seismic loading. Particularly, the median DCRs of the frames retrofitted with friction damper is smaller than that of the frames retrofitted with concentric braces in both locations. Figure 6-9 presents the DCRs for the beams. The data reveal that the median DCRs in the pre-code structures are close to one, indicating potential structural failure. On the other hand, median DCRs of both retrofitted frames are greatly reduced. The friction dampers are more effective at reducing the demands on beams compared to concentric braces. Figure 6-10 presents the DCRs for the connections. Like columns and beams, the connections in retrofitted structures show reduced median DCRs relative to the pre-code configuration. Among the retrofitting methods, friction dampers again demonstrate superior effectiveness in controlling seismic response. Overall, the comparison of DCRs demonstrates that seismic retrofitting of the pre-code building leads to improved performance and reduced risk of structural failure.

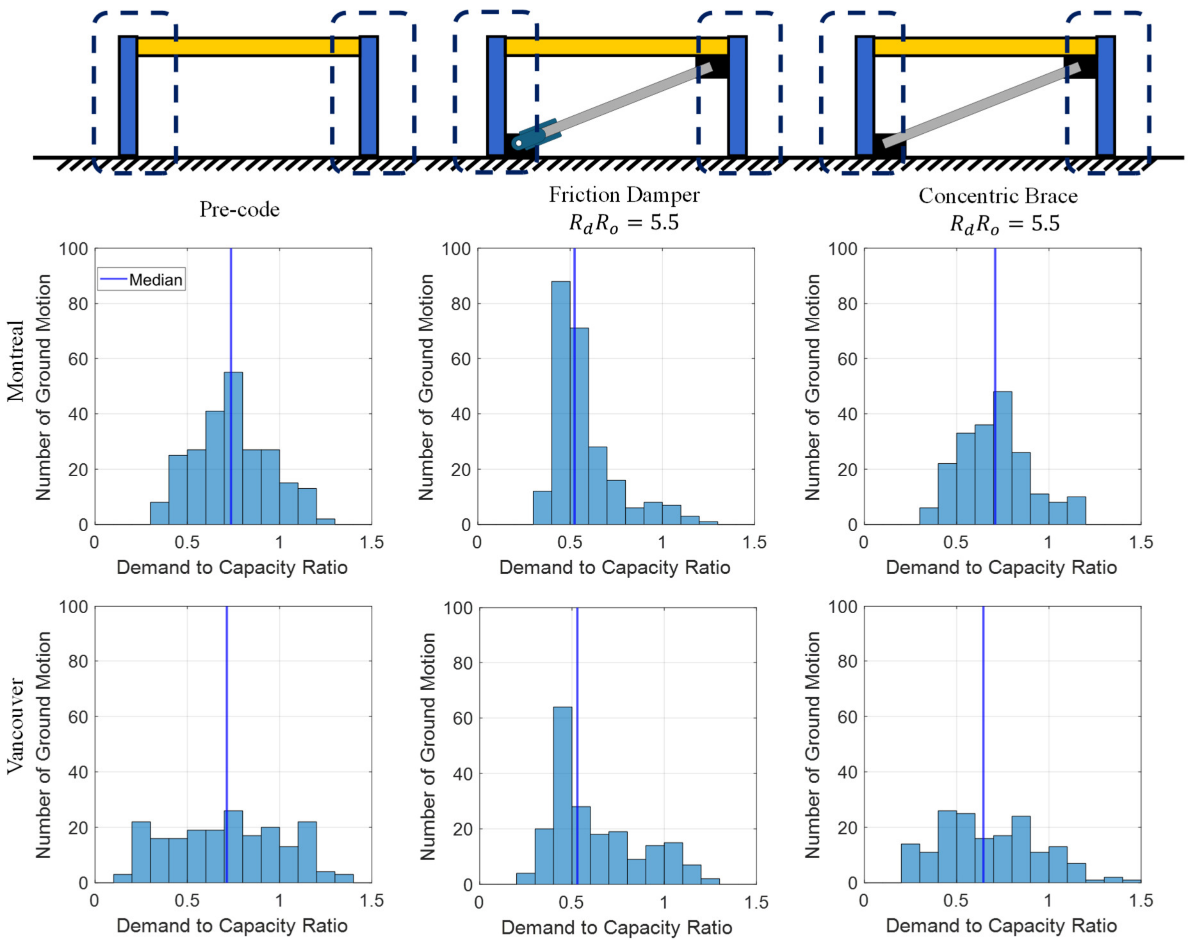

Figure 6-8 DCR of the first level interior bay column

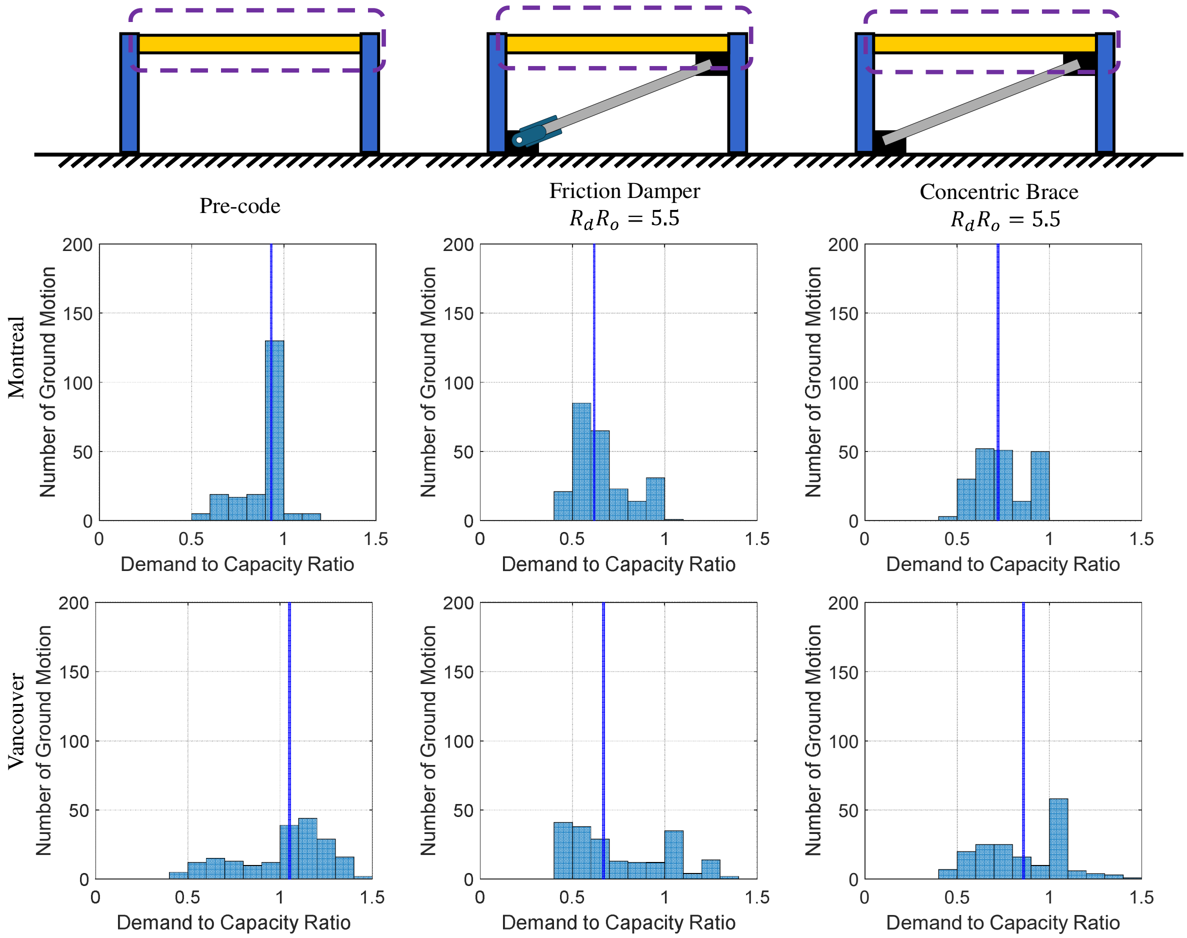

Figure 6-9 DCR of the first level interior bay beam

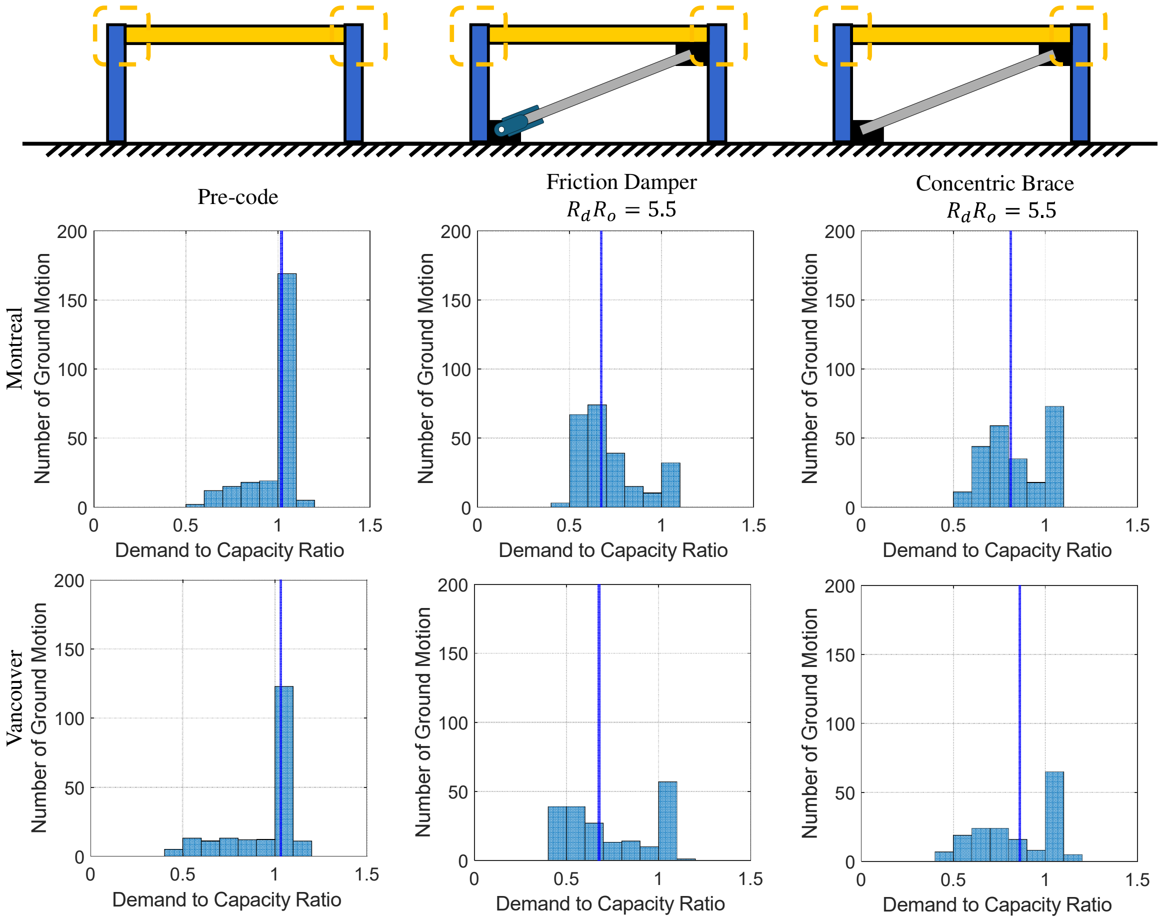

Figure 6-10 DCR of the first level interior bay connection

Chapter 7. Seismic Fragility Assessment

7.1. Seismic Capacity Model

In HAZUS (FEMA, 2022), the extent and severity of damage to both structural and non-structural components of a building are categorized into one of five damage states: None $(ds = 1)$, Slight $(ds = 2)$, Moderate $(ds = 3)$, Extensive $(ds = 4)$, and Complete $(ds = 5)$. The original structures are categorized as mid-rise steel MRF buildings, identified by the designation S1M. Conversely, the retrofitted structures, equipped with friction devices or concentric braces, are classified as mid-rise braced frames and are denoted S2M. The HAZUS damage state definitions for S1M and S2M for these five damage states are listed in Table 7-1.

Based on the results of time history responses and seismic demands of major structural members, the original frame is classified as having the pre-code seismic design, whereas the retrofitted frame is designated as high-code in seismic design. The capacity limit state thresholds for each damage state are outlined in Table 7-2, which include those for structural, drift-sensitive non-structural, and acceleration-sensitive non-structural components.

Table 7-1 Description of damage states for S1M and S2M

Damage States	Moment Frame (S1M)	Braced Frame (S2M)
None ($ds = 1$)	No damage	No damage
Slight ($ds = 2$)	Minor deformations in connections or hairline cracks in a few welds	A few steel braces may have yielded, possibly indicated by minor stretching or buckling of slender brace members. Additionally, minor cracks may be present in welded connections, along with minor deformations in bolted brace connections.
Moderate ($ds = 3$)	Some steel members have yielded, displaying noticeable permanent rotations at connections; major cracks may be observed in a few welded connections or some bolted connections may have broken bolts or enlarged bolt holes.	Some steel braces may have yielded, displaying observable stretching and/or buckling. Additionally, a few braces, other members, or connections may show signs of reaching their ultimate capacity, such as buckled braces, cracked welds, or failed bolted connections.
Extensive ($ds = 4$)	Most steel members have surpassed their yield capacity, leading to significant permanent lateral deformation of the structure. This level of damage may include instances where structural members or connections have exceeded their ultimate capacity, resulting in major permanent member rotations at connections, buckled flanges, and failed connections. Partial collapse of sections of the structure might occur due to the failure of critical elements and/or connections.	Most steel braces and other members have surpassed their yield capacity, leading to significant permanent lateral deformation of the structure. Some structural members or connections may have exceeded their ultimate capacity, evident through buckled or broken braces, flange buckling, broken welds, or failed bolted connections. Anchor bolts at columns may also be stretched. Partial collapse of sections of the structure might occur due to the failure of critical elements or connections.
Complete ($ds = 5$)	A significant portion of structural elements has exceeded their ultimate capacities or critical structural elements or connections have failed, resulting in dangerous permanent lateral displacement, partial collapse, or complete collapse of the building.	Most structural elements have reached their ultimate capacities, or critical members or connections have failed, resulting in dangerous permanent lateral deflection, partial collapse, or complete collapse of the building.

Table 7-2 Thresholds of damage states

Code Level	Component	EDP	Slight	Moderate	Extensive	Complete
Pre-code S1M	Structural	IDR (%)	0.32	0.51	1.08	2.67
	Drift-sensitive non-structural	IDR (%)	0.40	0.80	2.50	5.00
	Acceleration-sensitive non-structural	PFA (g)	0.20	0.40	0.80	1.60
High-code S2M	Structural	IDR (%)	0.33	0.67	2.00	5.33
	Drift-sensitive non-structural	IDR (%)	0.40	0.80	2.50	5.00
	Acceleration-sensitive non-structural	PFA (g)	0.30	0.60	1.20	2.40

7.2. Probabilistic Seismic Demand Analysis

Probabilistic seismic demand analysis (PSDA) calculates the demand model (PSDM) as a function of ground motion intensity measure. The Cloud analysis is employed to formulate the PSDM of interest in this study. The seismic demands of selected $EDPs$ are recorded and plotted against the IM for each ground motion in the logarithmic space. Subsequently, a linear regression analysis is conducted to establish the relationship between ground motion IM and $EDPs$ in logarithmic space, as shown in Figure 7-1 for the inter-story drifts of the original steel MRF in Montreal. The PSDM can be described mathematically by the following (Jalayer et al., 2014; Lu et al., 2008):

$$ln(\eta_{EDP|IM}) = ln\, a + b \times ln(IM) \tag{7-1}$$

$$\beta_{EDP|IM} = \sqrt{\frac{1}{n-2}\sum_{i=1}^{n}\left(ln(EDP) - ln(\eta_{EDP|IM})\right)^2} \tag{7-2}$$

where $\eta_{EDP|IM}$ is the mean value of the seismic demand regressed as a linear function of the IM, a and b are regression coefficients, $\beta_{EDP|IM}$ is the logarithmic standard deviation, and n is the number of $IM - EDP$ samples for the analysis.

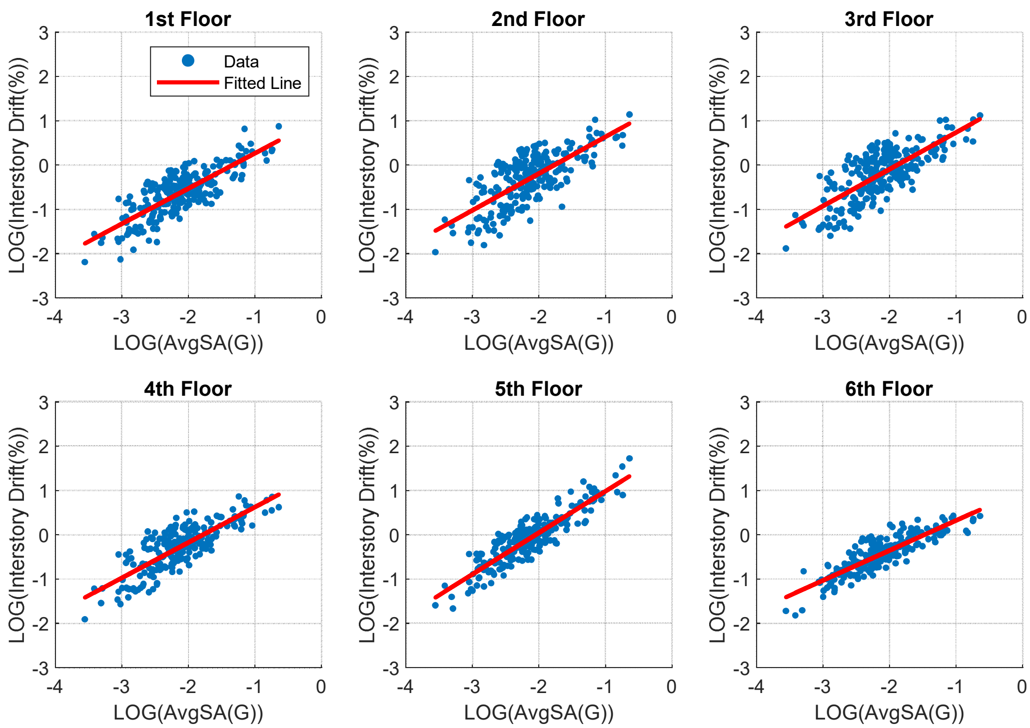

Figure 7-1: Probabilistic seismic demand model of the Montreal pre-code structure inter-story drifts

7.3. Seismic Fragility Curves

The seismic fragility curve based on the Cloud analysis method is expressed in the form of lognormal cumulative distribution as:

$$P(DS > ds|IM) = \Phi\left[\frac{ln\left(\frac{\eta_{EDP|IM}}{EDP_{ds}}\right)}{\sqrt{{\beta_{EDP|IM}}^2 + {\beta_{C,ds}}^2}}\right] \quad 7\text{-}3$$

where ds are the damage states, EDP_{ds} is the threshold for the EDP at damage state ds, and $\beta_{C,ds}$ is the associated standard deviation of the capacity model in the damage state ds. The $\beta_{C,ds}$ for the considered damage states are: 0.4 for drift-sensitive structural components, 0.5 for drift-sensitive non-structural components, and 0.6 for acceleration-sensitive non-structural components.

The comparison of fragilities between the Montreal pre-code structure and that retrofitted with friction dampers is presented through Figure 7-2 to Figure 7-4. Fragility functions provide the probability of exceeding limit states based on the intensity of ground shaking, and they are constructed based on the cloud analysis of 240 $IM - EDP$ samples. Figure 7-2 presents the fragility curves for drift-sensitive structural components. The retrofitted frame exhibits a reduced probability of exceeding any damage state compared to the pre-code frame under the same ground motion intensity. For example, at a hazard level of 2% in 50 years, approximately equivalent to 0.2 g measured with $AvgSA(T_a)$, the probability of exceeding the slight damage state is 95% in the pre-code frame. In contrast, with the addition of friction dampers, this probability decreases to 60%. Figure 7-3 shows the fragility curves for drift-sensitive non-structural components. A similar reduction in the probabilities of exceeding various damage states is observed for these components. Figure 7-4 depicts the fragility curves for acceleration-sensitive non-structural components. Unlike the drift-sensitive components, the reduction in the probabilities of exceeding damage states for acceleration-sensitive components is limited. Specifically, there are only marginal reductions in the probabilities of exceeding slight damage states across all levels. Figure 7-5 to Figure 7-7 illustrate the fragility comparisons for Vancouver, following the same order: drift-sensitive structural components, drift-sensitive non-structural components, and acceleration-sensitive non-structural components. These fragility functions are based on 200 $IM - EDP$ samples. The trends in Vancouver are similar to those in Montreal: friction devices significantly reduce the probabilities of damage for drift-sensitive components but show minimal impact on acceleration-sensitive components. This pattern aligns with previous observations of mean story responses in peak floor acceleration (PFA), where the use of friction devices somewhat increases the PFA in both cities.

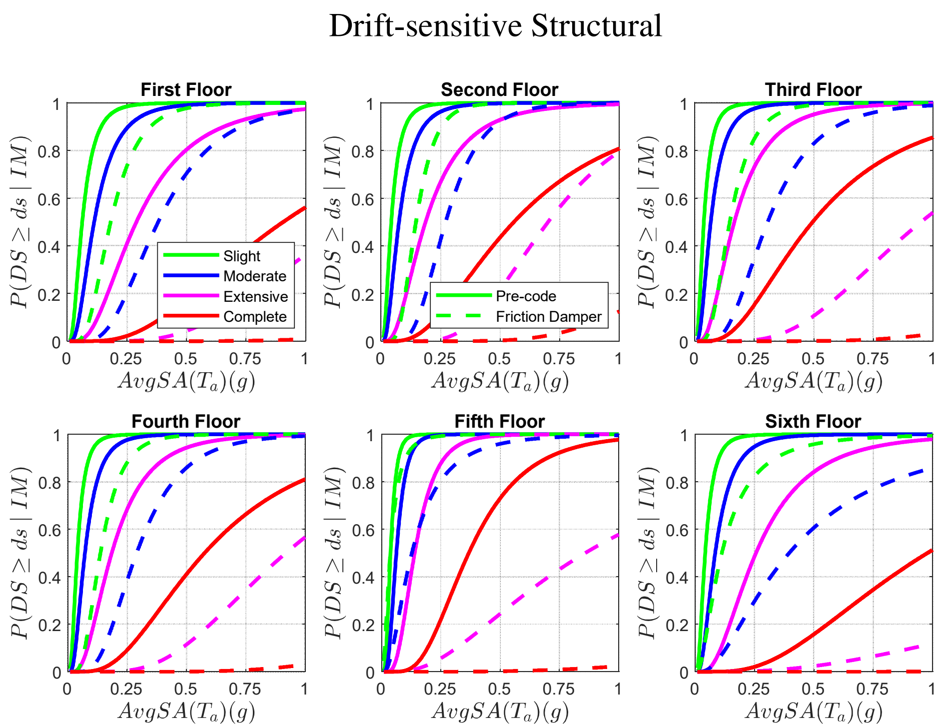

Figure 7-2 Seismic fragility comparison for drift-sensitive structural component in Montreal

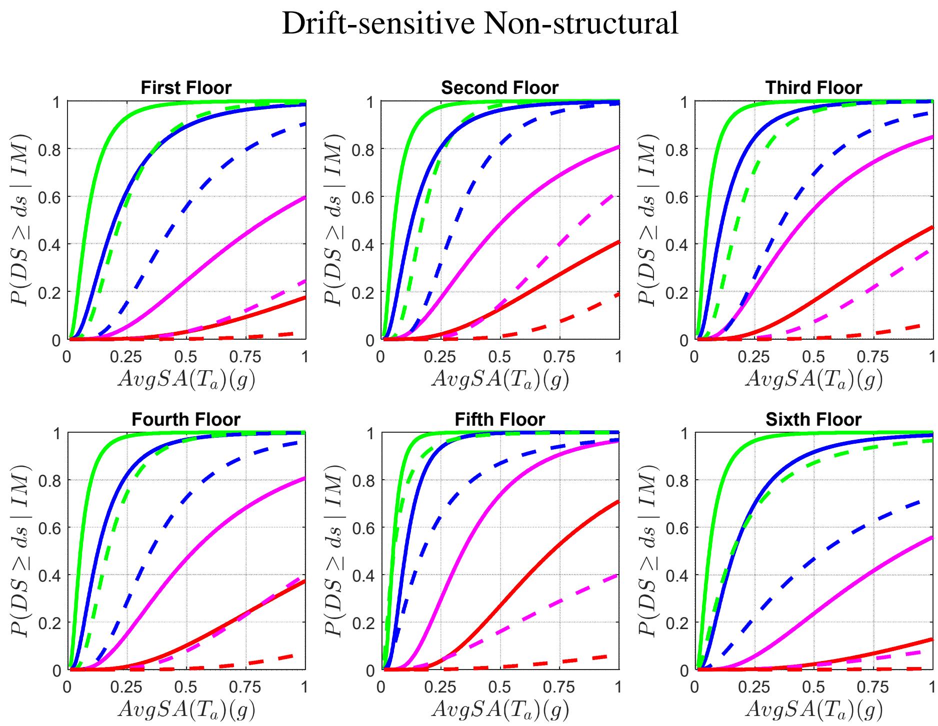

Figure 7-3 Seismic fragility comparison for drift-sensitive non-structural component in Montreal

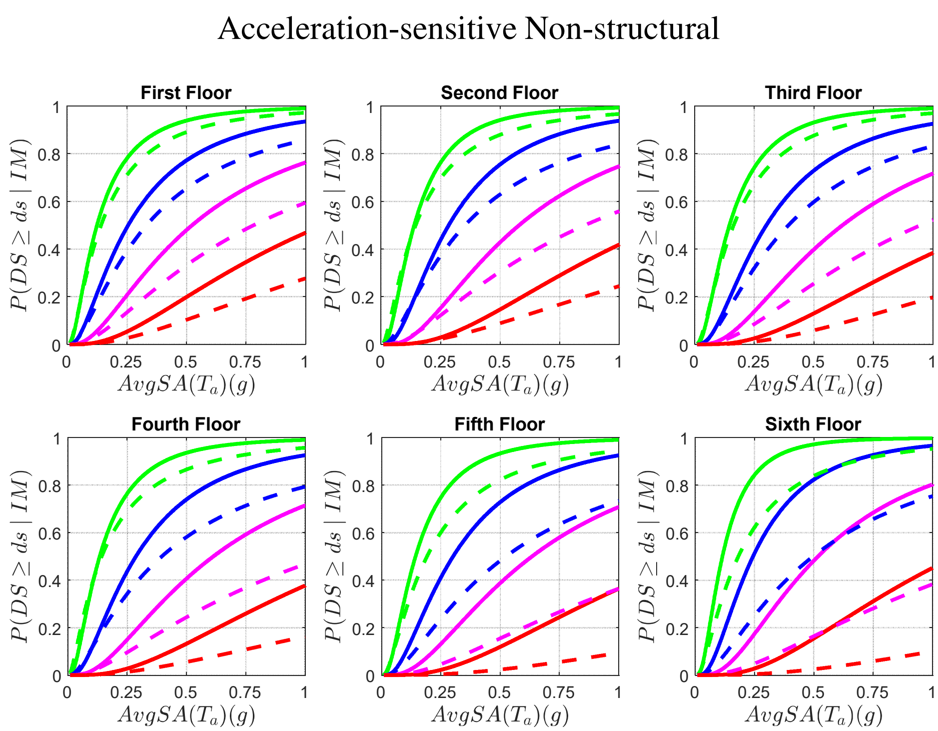

Figure 7-4 Seismic fragility comparison for acceleration-sensitive non-structural component in Montreal

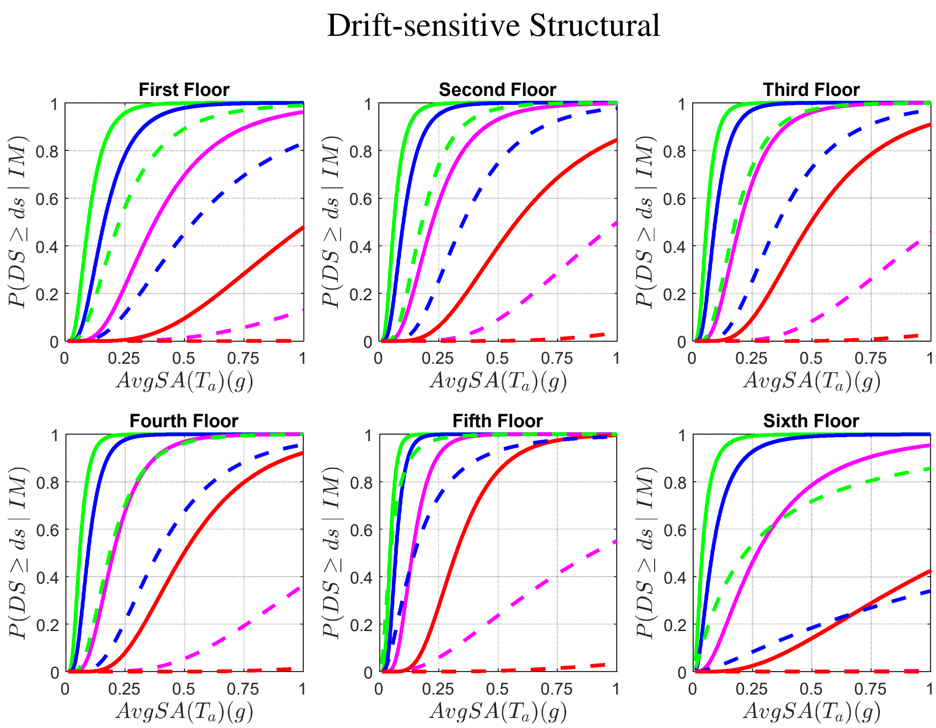

Figure 7-5 Seismic fragility comparison for drift-sensitive structural component in Vancouver

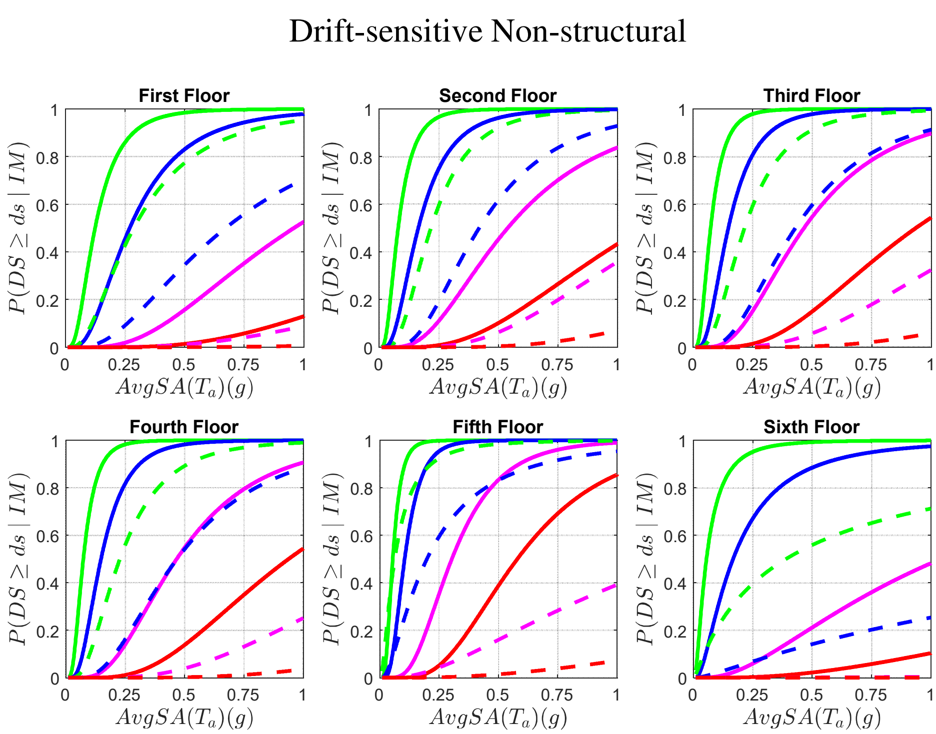

Figure 7-6 Seismic fragility comparison for drift-sensitive non-structural component in Vancouver

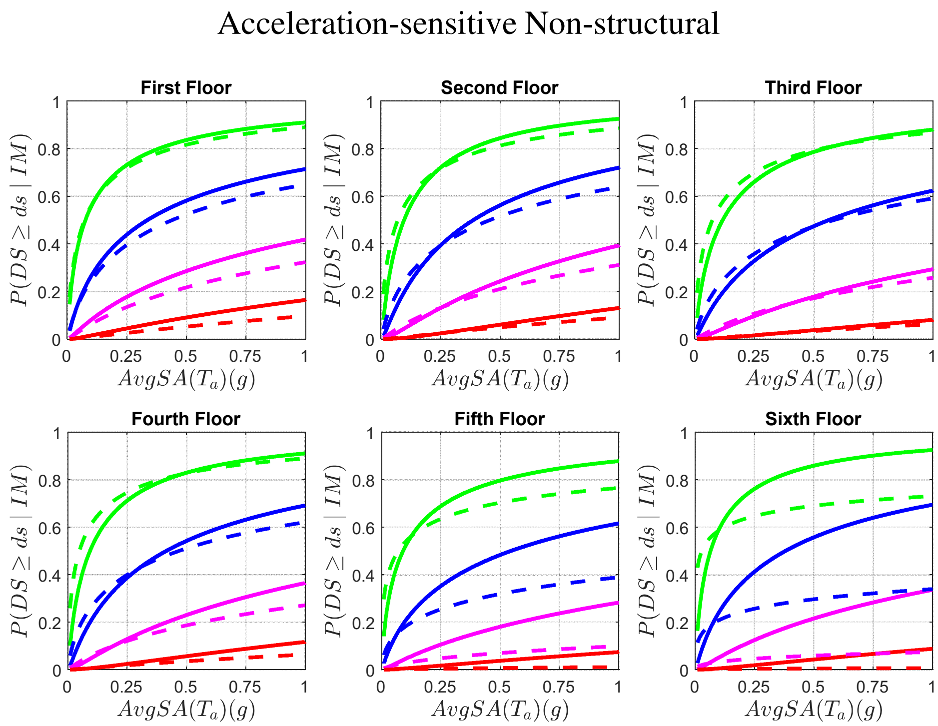

Figure 7-7 Seismic fragility comparison for acceleration-sensitive non-structural component in Vancouver

In the seismic evaluation of frames retrofitted with concentric braces, it is crucial to account for the potential for the probability of brace buckling and the associated replacement costs resulting from strong ground motions. To address this, a PSDM is first developed, where the demand is defined by axial deformation and the seismic capacity is represented by the buckling limit in the numerical model. Fragility curves for brace buckling are then constructed for both cities, with an example for the frame retrofitted with concentric braces in Montreal shown in Figure 7-8. These curves depict the probability of brace buckling at a given level of ground motion intensity, measured in $AvgSA(T_a)$. At a hazard level of 2% in 50 years, the probability of concentric brace buckling exceeds 50% on the first level. Conversely, the probability of brace buckling is lower on the fourth and sixth levels compared to other levels.

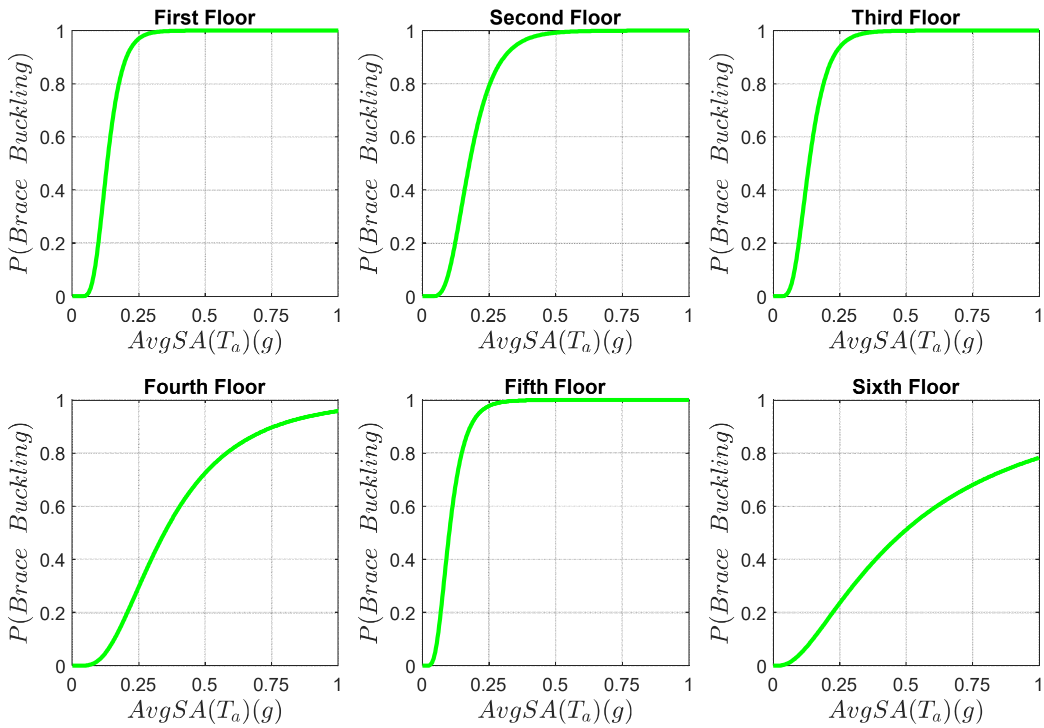

Figure 7-8 Buckling fragility curves of concentric braces in Montreal retrofitted frame

Chapter 8. Life-Cycle Cost-Benefit Analysis

8.1. Expected Annual Seismic Loss

For monetary loss estimates, the HAZUS methodology expands the scope by incorporating both structural and non-structural expenses, along with losses related to building contents, business inventory, business interruption, and rental income loss. This approach reflects a broader impact of building damage on functionality. By estimating the dollar value of damaged or destroyed buildings and factoring in income loss due to disrupted operations, the procedure not only quantifies the direct repair and replacement expenses but also provides insight into consequential losses. It demonstrates an immediate impact on the community in terms of financial strain on businesses, the resources needed for restoration, and potential job and housing challenges. It should be emphasized that while the incorporation of consequential losses represents a substantial expansion beyond the assessment of building damage and loss, the methodology remains constrained in its consideration of economic loss directly derived from building damage. In essence, it focuses solely on estimating direct economic loss, while the broader and more complex socio-economic impacts are not addressed.

The building of analysis is designated as COM4 occupancy within the HAZUS framework, and its seismic losses estimation is related to structural repair cost (STR), non-structural drift-sensitive repair cost (NSD), non-structural acceleration-sensitive repair cost (NSA), contents losses (CON), relocation expenses (REL), income losses (INC), rental income losses (RET), and casualties (CAS).

The losses related to building repair and replacement costs will stem from both structural damage and non-structural damage. The non-structural damage is further categorized into acceleration-sensitive damage (damage to ceilings, mechanical and electrical equipment integrated into the structure, piping, and elevators) and drift-sensitive damage (partitions, exterior walls, ornamentation, and glasses). The repair costs are calculated as follows:

$$STR = BRC \times \sum_{ds=2}^{5} PSTR_{ds} \times RCS_{ds} \quad \text{8-1}$$

$$NSD = BRC \times \sum_{ds=2}^{5} PNSD_{ds} \times RCD_{ds} \quad \text{8-2}$$

$$NSA = BRC \times \sum_{ds=2}^{5} PNSA_{ds} \times RCA_{ds} \quad \text{8-3}$$

where BRC is the building replacement cost; $PSTR_{ds}$, $PNSD_{ds}$, and $PNSA_{ds}$ are the probability of being in the damage state, ds, for structural, drift-sensitive non-structural, and acceleration-sensitive non-structural components; RCS_{ds}, RCD_{ds}, and RCA_{ds} are the repair cost ratio in damage state, ds, for structural, drift-sensitive non-structural, and acceleration-sensitive components.

The building contents include items such as furniture, equipment (those not integrated into the structure), computers, and other supplies. It is considered that most damage to contents, such as overturned cabinets, equipment sliding off tables and counters, is directly related to building accelerations. The cost associated with contents damage is determined as follows:

$$CON = CRV \times \sum_{ds=2}^{5} PNSA_{ds} \times CD_{ds} \tag{8-4}$$

where CRV is the contents replacement value; and CD_{ds} is the contents damage ratio in damage state, ds.

In situations where building damage renders it unusable for a period due to repairs, relocation costs will arise. These costs primarily include expenses related to disruption, such as shifting and transferring operations, and the temporary rental of alternative space. The burden of these relocation expenses is not expected to be borne by the renter. Instead, it is assumed that the building owners will bear the cost of relocating their tenants to a new location. If the damaged property is owner-occupied, the owner will be responsible for both the disruption costs and the rent for temporary accommodation during the repair period. The relocation cost is given by the following expression:

$$REL = FA \begin{bmatrix} (1 - \%FO) \times \sum_{ds=3}^{5} PSTR_{ds} \times DC + \\ \%FO \times \sum_{ds=3}^{5} (PSTR_{ds} \times (DC + RENT \times RT_{ds})) \end{bmatrix} \tag{8-5}$$

where FA is the floor area; FO is the percentage of floor area occupied by the owner; DC is the distribution cost. $RENT$ is the rental cost; and RT_{ds} is the recovery time for the damage state, ds;

Business activities generate incomes, and income losses arise when building damage disrupts economic activities. These losses are calculated as the product of the floor area, the income realized per square foot, and the expected number of days of functionality loss for each damage state. The income losses are expressed as follows:

$$INC = (1 - RF) \times FA \times INCM \times \sum_{ds=2}^{5} PSTR_{ds} \times RT_{ds} \times MOD_{ds} \qquad 8\text{-}6$$

where RF is the recapture factor; $INCM$ is the income generated from business activities; and MOD_{ds} is the construction time modifier for damage state, ds.

The owner of the building receives regular rental payment for the property. However, when the building is damaged, renters will cease paying rent to the owner of the damaged property and will instead pay rent to their new landlord during relocation. Rental income losses are calculated by multiplying the floor area, rental rates per square foot, and the expected number of days of functionality loss for each damage state. Additionally, these losses are based on the percentage of floor area that is being rented, which is represented by $(1 - \%FO)$. The rental income losses are calculated as follows:

$$REN = (1 - \%FO) \times FA \times RENT \times \sum_{ds=3}^{5} PSTR_{ds} \times RT_{ds} \qquad 8\text{-}7$$

Casualties from an earthquake, which can include loss of life or injuries, are evaluated by calculating the fatality rate and multiplying it by the cost per fatality. Casualties are assessed based on the structural damage states of buildings. The losses related to casualties are estimated by (Ghasemof et al., 2021; Zhang et al., 2022):

$$CAS = \sum_{sl=2}^{4} CAS_{sl} \times (OCP \times FA) \times$$

$$\left[\sum_{ds=2}^{4} PSTR_{ds} \times CR_{ds} + \begin{bmatrix} PSTR_{ds=5} \times \left[\left(1 - P_{Collapse}\right) \times CR_{ds=5}\right] \\ +P_{Collapse} \times CR_{\text{collapse}}\end{bmatrix}\right] \tag{8-8}$$

where CAS_{sl} is the cost of casualty for injury severity level, sl; OCP is the average occupancy rate; CR_{ds} is the casualty rate for damage state, ds; $P_{Collapse}$ is the probability of collapse under complete damage state; and CR_{collapse} is the casualty rate when the structure collapses. The damage factors used for estimating losses due to earthquakes for COM4 occupancy are retrieved from HAZUS and are presented in Table 8-1. Additionally, the FO, RF, and OCP are taken as 55%, 0.9%, and 0.2%, respectively. $P_{Collapse}$ is assumed 5%.

Table 8-1 Damage factors for loss estimation

<table>
<tr><th colspan="2" rowspan="2">Damage Factor</th><th colspan="4">Damage State</th><th rowspan="2">Collapse</th></tr>
<tr><th>Slight</th><th>Moderate</th><th>Extensive</th><th>Complete</th></tr>
<tr><td rowspan="4">Repair and Replacement Ratios</td><td>RCS_{ds} (%)</td><td>0.4</td><td>1.9</td><td>9.6</td><td>19.2</td><td rowspan="6">N/A</td></tr>
<tr><td>RCA_{ds} (%)</td><td>0.9</td><td>4.8</td><td>14.4</td><td>47.9</td></tr>
<tr><td>RCD_{ds} (%)</td><td>0.7</td><td>3.3</td><td>16.4</td><td>32.9</td></tr>
<tr><td>CD_{ds} (%)</td><td>1</td><td>5</td><td>25</td><td>50</td></tr>
<tr><td rowspan="2">Building Recovery Time and Service Interruption Time Multiplier</td><td>RT_{ds} (day)</td><td>20</td><td>90</td><td>360</td><td>480</td></tr>
<tr><td>MOD_{ds}</td><td>0.1</td><td>0.1</td><td>0.2</td><td>0.3</td></tr>
<tr><td rowspan="4">Casualty rates CR_{ds} (%)</td><td>Severity level 1</td><td>0.05</td><td>0.2</td><td>1</td><td>5</td><td>40</td></tr>
<tr><td>Severity level 2</td><td>0</td><td>0.025</td><td>0.1</td><td>1</td><td>20</td></tr>
<tr><td>Severity level 3</td><td>0</td><td>0</td><td>0.001</td><td>0.01</td><td>5</td></tr>
<tr><td>Severity level 4</td><td>0</td><td>0</td><td>0.001</td><td>0.01</td><td>10</td></tr>
</table>

The monetary loss estimation parameters in HAZUS were established based on consensus decades ago and may no longer accurately reflect current realistic costs. To update these values for the year 2023, an adjustment for inflation using appropriate indexes is necessary. Note that the cost data related to casualties, which is derived from recent research (Ghasemof et al., 2021) , is based on 2020 figures and has not yet been adjusted for inflation. Table 8-2 provides a summary of the parameters, including both the original values and those adjusted for inflation.

Table 8-2: Monetary loss estimation parameters in HAZUS and reference year

Parameters	Value	Reference Year	Inflation Adjusted Value
BRC ($/sq.ft)	98.96	2002	224.17
CRV ($/sq.ft)	98.96		224.17
$RENT$ ($/sq.ft/month)	1.36	1994	2.24
DC ($/sq.ft)	0.95		1.56
$INCM$ ($/sq.ft/day)	0.923	1985	1.45
$CAS_{sl=2}$($)	2700	2020	2700
$CAS_{sl=3}$ ($)	27000		27000
$CAS_{sl=4}$ ($)	4744000		4744000
Discount Rate	2%	-	2%

As presented in Figure 8-1, Statistics Canada releases three sets of data related to the parameters of building loss estimation (Statistics Canada, 2023): 1. Building construction price index (BCPI), a price index for monitoring fluctuations in construction costs across different types of buildings, including both residential and non-residential structures. It offers insights into the changing expenses associated with materials, labor, equipment, overhead, and profit margins involved in building construction projects 2. Consumer price index (CPI), a gauge reflecting changes in prices faced by Canadian consumers over time. These changes are tracked by comparing the costs of a consistent selection of goods and services. 3. Commercial rent services price index (CRSP), which tracks fluctuations in the net effective rent for occupied commercial building space across Canada over time. This index is updated quarterly and is based on the average rents, measured in price per square foot, for a selection of commercial buildings. All three indexes have demonstrated steady growth over the past decades. Compared to their levels in the 1980s, both the BCPI and the CPI have more than tripled. The CRSPI, despite being a relatively new index, also shows a consistent upward trend, increasing by approximately 2% annually. The building replacement cost (BRC) is adjusted based on BCPI, the business income ($INCM$) is adjusted based on CPI, and the rental cost ($RENT$) and distribution cost (DC) are adjusted based on CRSP.

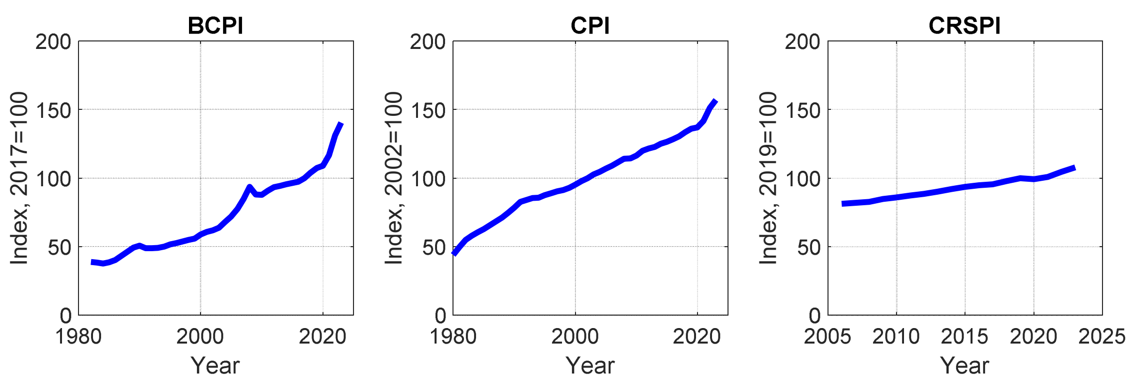

Figure 8-1 Trend of BCPI and CPI between 1980 and 2023, and trend of CSRP between 2005 to 2023

The expected annual losses (EAL) calculated for buildings retrofitted with friction dampers are presented in Figure 8-2 and Figure 8-3. Each figure includes the EAL for the pre-code building and all retrofit design cases with friction dampers, displayed in monetary value, along with percentage breakdowns of the loss components. In Montreal, the retrofit design with $R_d R_o = 7.5$ demonstrates the lowest seismic losses at \$199 per year, representing an 78% reduction compared to the pre-code structure. On the other hand, in Vancouver, the retrofit with $R_d R_o = 12$ achieves the lowest value of $677, also reducing the original loss by around 75%. Analysis of the percentage charts reveals that acceleration-related costs (NSA and CON) contribute more significantly to the overall loss in the retrofitted structures compared to the pre-code structures in both cities. In Montreal, the percentage contribution of acceleration-related costs retrofitted frame remains around 40%, with no notable variation across various $R_d R_o$ combinations. In contrast, the frames in Vancouver show higher percentage contributions, exceeding 50%. Additionally, this percentage decreases as $R_d R_o$ increases. Overall, the examination of the EAL is consistent with the observations from seismic fragility analysis, which indicates that loss reductions are predominantly due to drift-related costs rather than acceleration-related costs. Concentric braces are compared to friction dampers at $R_d R_o = 5.5$ in Figure 8-4. Specifically, the EAL for concentrically braced frames exceeds that of friction damper retrofitted frames in both cities. Additionally, while the contribution of acceleration-related costs to the overall EAL is similar for both retrofitted frames in Montreal and Vancouver, drift-related costs contribute significantly more to the overall EAL in the frame retrofitted with concentric braces compared to that with friction dampers. This further highlights the superior performance of friction dampers.

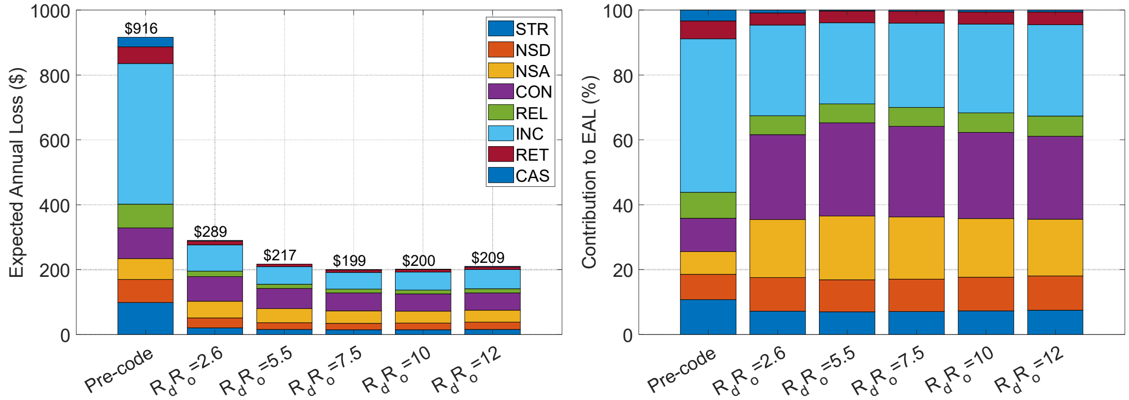

Figure 8-2 EAL of pre-code building and retrofitted buildings with friction devices in Montreal

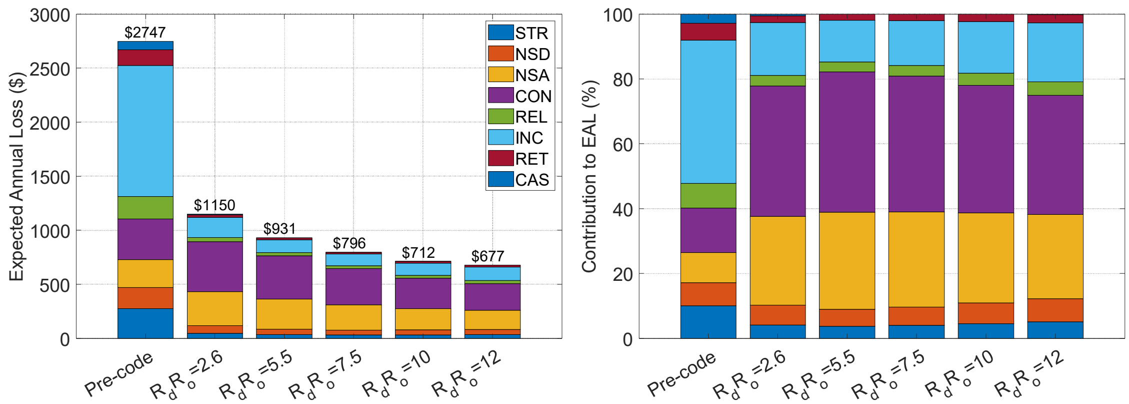

Figure 8-3 EAL of pre-code building and retrofitted buildings with friction devices in Vancouver

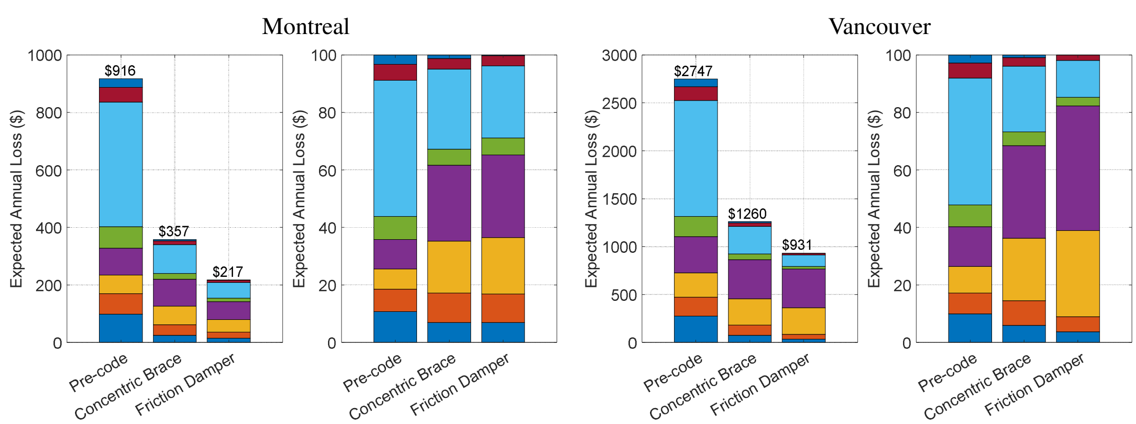

Figure 8-4 Comparison between EALs of retrofitted frames using friction devices and concentric braces

8.2. Life-Cycle Cost-Benefit Analysis

The life-cycle cost of the structure subjected to seismic hazard can subsequently be estimated using the following equation:

$$C_{LC}(t, \boldsymbol{X}) = C_0(\boldsymbol{X}) + C_M(t, \boldsymbol{X}) + C_{LCE}(t, \boldsymbol{X}) \tag{8-9}$$

where the $C_{LC}(t, \boldsymbol{X})$ is the life-cycle cost, $C_0(\boldsymbol{X})$ is the initial construction cost, and $C_M(t, \boldsymbol{X})$ is the life-cycle operation and maintenance cost, and $C_{LCE}(t, \boldsymbol{X})$ is the life-cycle earthquake-induced cost. t is the life span of the building and $\boldsymbol{X}$ is the retrofit design vectors. The life-cycle earthquake-induced cost, $C_{LCE}(t, \boldsymbol{X})$, is calculated by discounting the annual cost to the time of construction with the discount rate r (Ghasemof et al., 2021) as shown in Equation 8-10.

$$C_{LCE}(t, \boldsymbol{X}) = C_{LCE}(1, \boldsymbol{X}) \times \frac{1-(1+r)^{-t}}{r} \tag{8-10}$$

where $C_{LCE}(1, \boldsymbol{X})$ represents the earthquake-induced cost in one year, which is equivalent to the expected annual loss EAL_X calculated in the previous section. Based on Equation 8-10, Figure 8-5 illustrates the life-cycle earthquake-induced cost C_{LCE} plotted against the life-cycle span t. As expected, the C_{LCE}increases as t increases. In Montreal, the C_{LCE} for a pre-code structure over a 100-year lifespan is \$39,478. In contrast, the frame retrofitted with a friction damper with $R_dR_o = 7.5$ has a C_{LCE} of \$8,577, representing an 80% reduction. Additionally, the C_{LCE} for retrofitted frames shows minimal sensitivity to changes in R_dR_o; it is higher when $R_dR_o = 2.6$ but remains relatively consistent for other values of R_dR_o. In Vancouver, the reduction in C_{LCE} is more pronounced. For the pre-code frame, compared to the retrofitted frame with $R_d R_o = 12$, the reduction amounts to \$89,212, or 75%. There is also a clear trend of decreasing C_{LCE} as $R_d R_o$ increases.

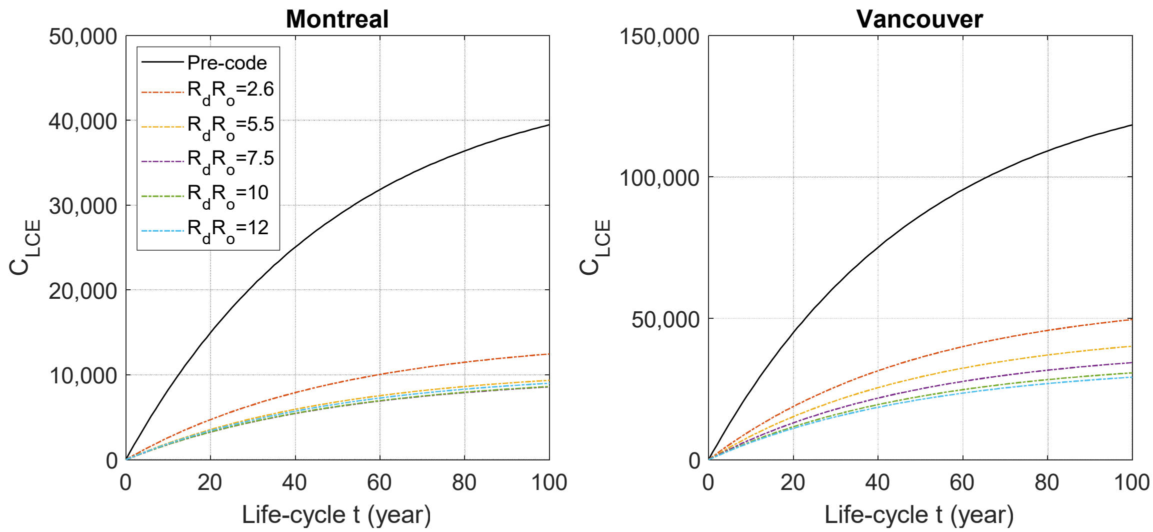

Figure 8-5: Life-cycle Earthquake-induced Cost

The expected annual loss of retrofitted steel structures is lower than that of the original structure, whereas the savings of future seismic losses should be compared with the upfront cost spent on seismic retrofits. Hence, it is necessary to scrutinize the life-cycle cost and economic benefit over the building's life cycle (Cutfield et al., 2016; Dyanati et al., 2017). The anticipated benefit over the life cycle is computed using the following equation:

$$B_{LC} = \Delta C_0(\boldsymbol{X}) + \Delta C_M(t, \boldsymbol{X}) + \Delta C_{LCE}(t, \boldsymbol{X}) \qquad 8\text{-}11$$

where $\Delta C_0(X)$ is the differential of initial retrofit cost, $\Delta C_M(t, \boldsymbol{X})$ is the differential of the life cycle operation and maintenance cost, and $\Delta C_{LCE}(t, \boldsymbol{X})$ is differential of the life-cycle earthquake-induced cost. The operation and maintenance costs are primarily influenced by the occupancy of the building rather than the structural system, so it is assumed that these costs remain constant across the case study buildings. As such, the differential of the life cycle operation and maintenance cost $\Delta C_M(t, \boldsymbol{X})$ is presumed to be zero. To accurately estimate the initial retrofit costs $\Delta C_0(\boldsymbol{X})$, the costs of the braces and friction dampers are analyzed separately. Fang et al. (2021) conducted a market survey on the friction devices in the US and Japanese markets. The material cost of steel HSS sections is estimated at \$4 per kg. Each friction device is priced at \$410, with an additional lump sum cost of \$2400 for transportation and assembly. For the seismic retrofit of a building using friction devices, 12 steel braces and 12 friction devices are required. In contrast, for a frame retrofitted with concentric braces, only 12 steel braces are needed.

The life-cycle cost-benefit analysis (LCCB) of $R_d R_o = 2.6$ friction-retrofitted frame in Vancouver is shown as an example in Figure 8-6: the B_{LC} is obtained by (1) calculating the $\Delta C_{LCE}(t, \boldsymbol{X})$ between the pre-code and retrofitted structure, and (2) moving down the starting point of the curve to a negative value corresponding to $\Delta C_0(\boldsymbol{X})$. The curve demonstrates that while investing in seismic upgrades produces a negative monetary value in the beginning, the B_{LC} will increase toward positive as time t increases because of the lower seismic losses of the $C_{LCE}(t, \boldsymbol{X})$ for retrofitted frames.

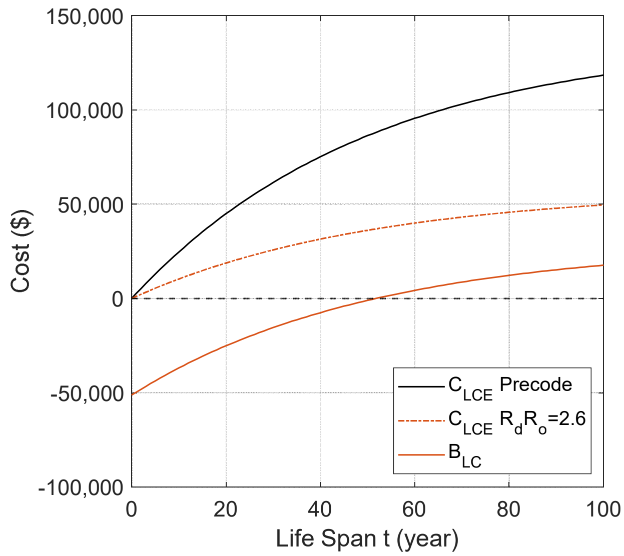

Figure 8-6: Life-cycle cost-benefit analysis (LCCB)

The comparison of B_{LC} across various designs is shown in Figure 8-7. The intersection between the B_{LC} and x axis represents the payback point, at which the net present value (NPV) equals zero. The analysis indicates that the seismic retrofit in Montreal takes approximately 60 years to pay back, whereas in Vancouver, it takes about 40 years. Additionally, consistent with the observations in the C_{LCE}, the B_{LC} shows minimal sensitivity to changes in R_dR_o in Montreal. In contrast, Vancouver exhibits a clear trend where the B_{LC} increases with higher values of R_dR_o.

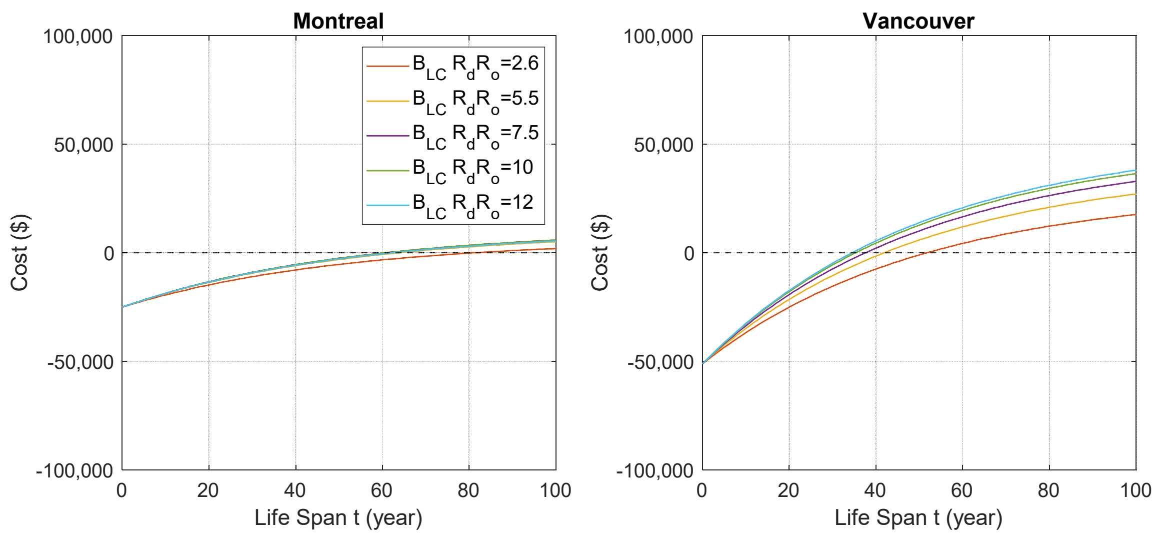

Figure 8-7: Comparison of LCCB of friction devices with different designs

The concentrically braced frames are analyzed in a similar manner. In addition to the EAL, the annual expense for brace replacement is also considered, amounting to approximately \$4 in Montreal and \$15 in Vancouver. These costs are calculated by integrating the previously obtained brace buckling fragility from Chapter 7, the seismic hazard curves detailed in Chapter 4, as well as the costs of changing concentric braces. The comparison between friction devices and concentric braces in terms of life cycle benefits is depicted in Figure 8-8. In Montreal, both retrofit methods result in a similar return period when $R_dR_o = 5.5$, with minimal net benefits observed over a 100-year lifespan. In Vancouver, although friction dampers lead to lower annual seismic losses, their higher initial costs reduce their overall life cycle benefits compared to concentric braces. The payback period for seismic retrofitting with concentric braces is approximately 25 years, while for frames retrofitted with friction dampers, it extends to about 40 years.

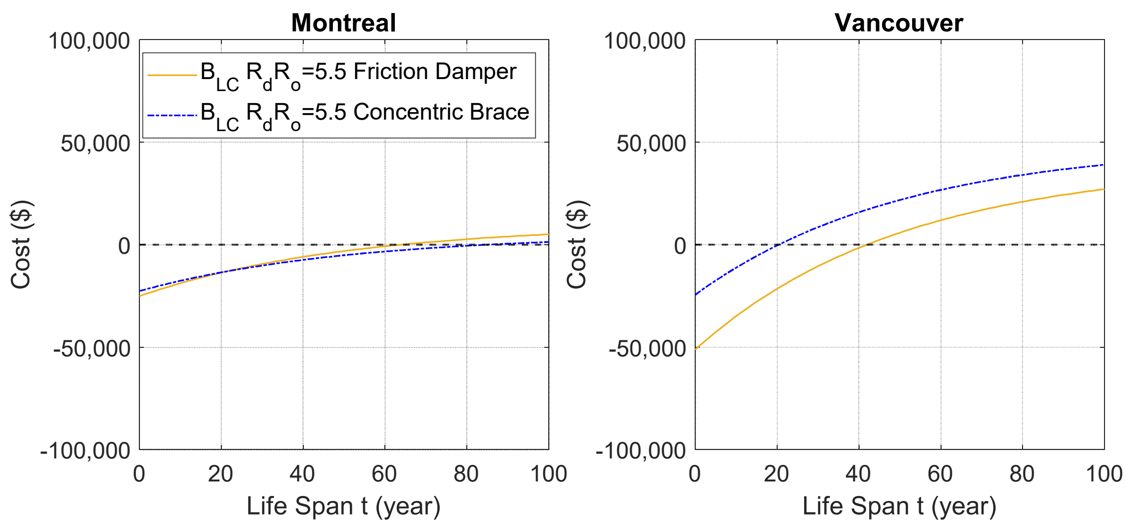

Figure 8-8 Comparison of LCCB between friction devices and concentric brace

To evaluate all design scenarios quantitively, NPV and benefit cost ratio (BCR) are calculated as following:

$$NPV = B_{LC} - \Delta C_0(\boldsymbol{X}) \tag{8-12}$$

$$BCR = \frac{B_{LC}}{\Delta C_0(\boldsymbol{X})} \tag{8-13}$$

The related NPV and BCR under assumption of 100-year are presented in Table 8-3. In Montreal, the BCR for friction device retrofits is approximately 1.20 across different R_dR_o values, indicating that the benefits are nearly equal to or slightly exceed the costs. The optimal retrofit occurs at $R_dR_o = 7.5$, where the NPV reaches its highest value of $5,823. In Vancouver, $NPVs$ are considerably higher than in Montreal, with positive values for all scenarios; for example, at $R_dR_o = 12$, the NPV is $38,004, reflecting a significant net benefit. On the other hand, frame retrofitted with concentric brace shows a low NPV in Montreal, suggesting they are less cost-effective there. However, in

Vancouver, concentric braces yield a substantial positive NPV of $39,000 and an excellent BCR of 2.60, making them a highly attractive retrofit option in that location.

Table 8-3 NPV and BCR of seismic retrofits using friction devices and concentric braces

Retrofit Methods	Location	SR	$R_d R_o$	Net Present Value	Benefit Cost Ratio
Friction Device	Montreal	2	2.6	1945	1.08
			5.5	5048	1.20
			7.5	5823	1.23
			10	5780	1.23
			12	5393	1.22
	Vancouver	2	2.6	17619	1.34
			5.5	27057	1.53
			7.5	33146	1.65
			10	36496	1.71
			12	38004	1.74
Concentric Brace	Montreal	-	5.5	1325	1.06
	Vancouver	-		39000	2.60

8.3. Variation of Steel Brace Design

A significant portion of the seismic retrofit cost comes from steel braces, and this cost can be reduced if smaller brace sections are utilized. Traditionally, brace selection involves choosing a brace stiffness double that of the floor stiffness, as outlined in Chapter 4. To further investigate the impact of reduced brace sections, additional stiffness ratios (SR) are analyzed for the Vancouver structure. The selection process adheres to the original procedure, but with targets set at $SR = 1.0$ and $SR = 1.5$. Such parameter variations are not implemented in Montreal due to its smaller floor stiffness, where lower SR targets would further weaken the structure, making it inadequate to resist wind loads. Alongside these variations, a separate design approach is tailored to withstand wind loads, wherein steel braces are selected to resist 115% of the wind loads without targeting specific SR values. Friction damper slip loads are also determined based on the chosen steel brace sections. Since the wind loadings in Montreal and Vancouver are similar according to the NBCC 2020, a uniform wind design approach is implemented for both cities. The detailed designs for both the SR-based and wind-based scenarios are presented in Table 8-4 and Table 8-5, respectively.

Table 8-4 SR-based designs for Vancouver structure

SR	Type	Level	HSS Section	Brace Area (mm^2)	Ratio
$SR = 1.5$	Roof	6	127.0 ×127.0 × 6.4	2770	1.51
	Floor	5	127.0 × 127.0 × 6.4	2770	1.76
	Floor	4	304.8 × 304.8 × 9.5	10300	1.41
	Floor	3	304.8 × 304.8 × 9.5	10300	1.71
	Floor	2	457.2 × 457.2 × 12.7	21900	1.64
	Floor	1	254.0 × 254.0 × 9.5	8520	1.54
$SR = 1.0$	Roof	6	114.3 × 114.3 × 4.8	1880	1.02
	Floor	5	114.3 × 114.3 × 4.8	1880	1.19
	Floor	4	228.6 × 228.6 × 9.5	7620	1.04
	Floor	3	228.6 × 228.6 × 9.5	7620	1.27
	Floor	2	304.8 × 304.8 × 12.7	13500	1.01
	Floor	1	228.6 × 228.6 × 7.9	5650	1.02

Table 8-5 Wind-based designs for Vancouver structure

Type	Level	Brace Section	Damper Slip Load (kN)
Roof	6	114.3 × 114.3 × 3.2	40
Floor	5	139.7 × 139.7 × 4.8	100
Floor	4	152.4 × 152.4 × 6.4	170
Floor	3	177.8 × 177.8 × 6.4	240
Floor	2	177.8 × 177.8 × 6.4	300
Floor	1	203.2 × 203.2 × 6.4	390

Figure 8-9 compares the EAL across various SR-based designs, it is found that $SR = 2.0$ and $R_d R_o = 12$ still yields the minimum annual seismic loss. Generally, as SR increases, annual losses decrease, indicating that additional stiffness is beneficial for reducing annual losses. However, this reduction in annual losses is accompanied by changes in the cost components: a larger SR typically lowers drift-related costs (e.g., INC) but raises acceleration-related costs (e.g., CON). To determine whether these reductions in annual losses justify the higher initial investment in larger braces, a life cycle cost-benefit (LCCB) analysis must be conducted. Figure 8-10 compares the EAL of the wind-based design. The analysis reveals that the reduction in EAL achieved with the wind-based design is smaller compared to the optimal SR-based designs in both cities. Specifically, the wind-based design shows a less significant reduction in drift-related losses compared to the SR-based design.

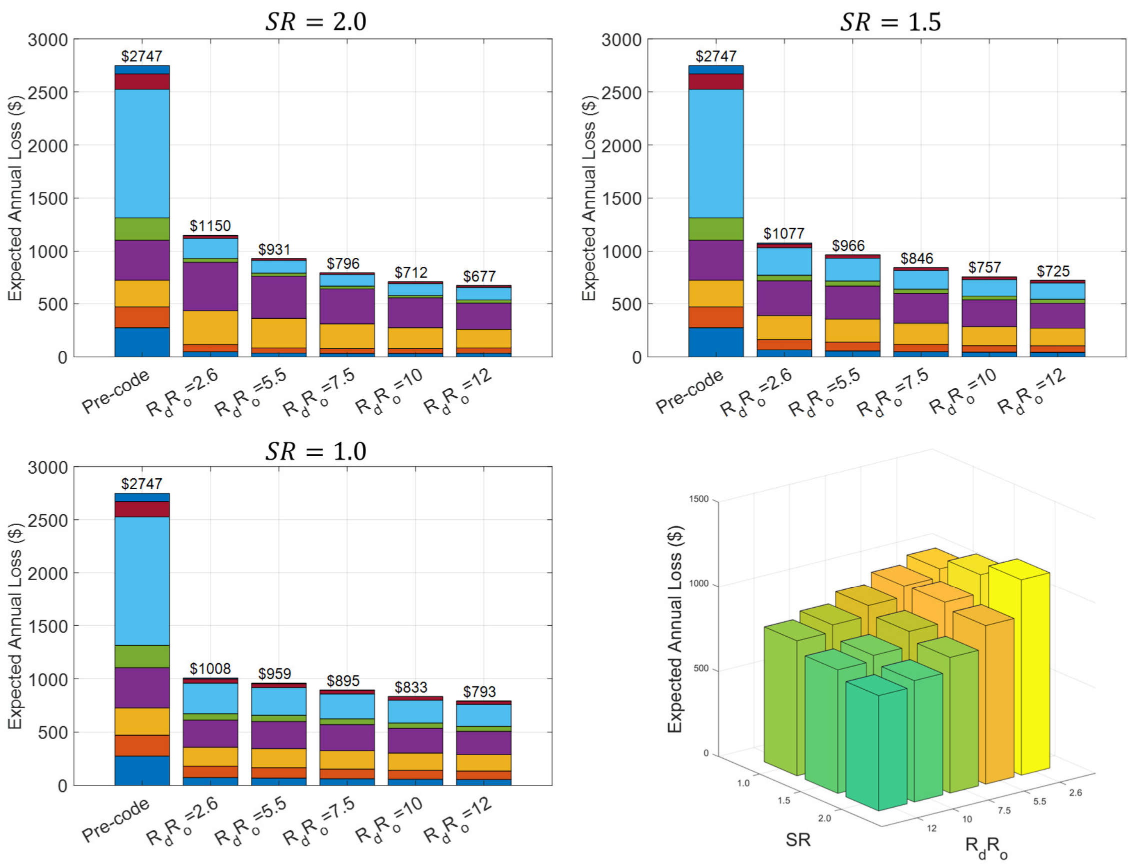

Figure 8-9 EAL of Vancouver structure retrofitted with friction dampers under various design configurations

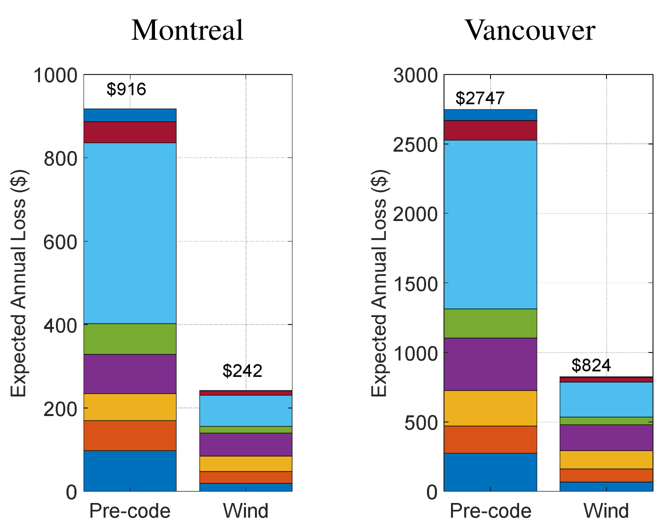

Figure 8-10 EAL of structures retrofitted with friction dampers designed based on wind loads

The LCCB analysis is conducted on the new cases and the results are shown in Figure 8-11. Consistent with previous observations, the payback period of the Vancouver structure decreases as the initial retrofit cost, which is influenced by the SR, decreases. $R_d R_o = 12$ continues to provide the most economical solutions compared to other values, whether SR is 1.5 or 1.0. The design optimized against wind loads demonstrates the best BCR and the shortest return period overall: approximately 12 years in Vancouver and 40 years in Montreal.

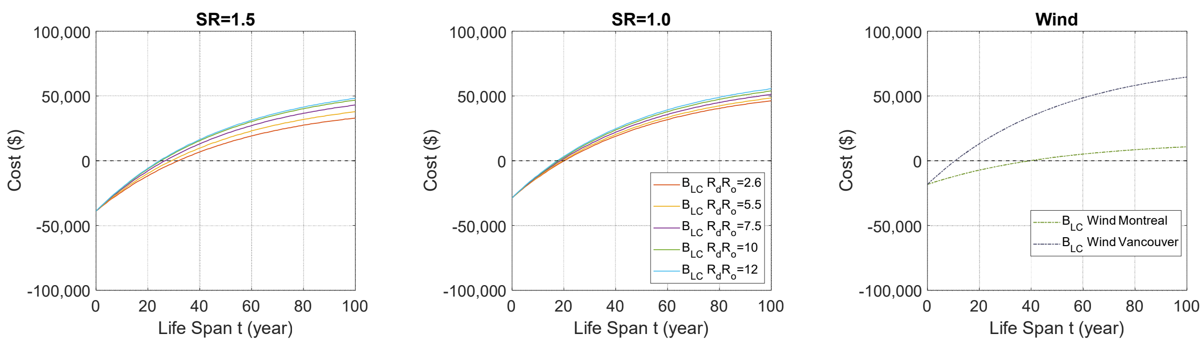

Figure 8-11 LCCB of SR=1.5 and SR=1.0 for Vancouver structure, and LCCB of wind design for both Montreal and Vancouver structures

Table 8-6 and Table 8-7 provides a detailed analysis of the BCR and NPV for all scenarios. The SR-based design demonstrates that both NPV and BCR increase as the SR decreases, highlighting the advantages of lower upfront costs. The optimal SR-based design achieves an NPV of $55,581 with an BCR of 2.94. Moreover, wind retrofits are found to offer the most economical solutions for both cities among all design options. Vancouver wind design has a BCR of 4.54, which is significantly higher than Montreal's, indicating that the wind retrofit in Vancouver is particularly cost-effective, offering substantial benefits relative to its costs.

Table 8-6 NPV and BCR for SR-based designs

Location	SR	$R_d R_o$	Net Present Value	Benefit Cost Ratio
Vancouver	1.5	2.6	33053	1.85
		5.5	37837	1.97
		7.5	43009	2.11
		10	46845	2.20
		12	48224	2.24
	1	2.6	46315	2.62
		5.5	48427	2.69
		7.5	51185	2.79
		10	53857	2.88
		12	55581	2.94

Table 8-7 NPV and BCR for wind-based designs

Location	Net Present Value	Benefit Cost Ratio
Montreal	10780	1.59
Vancouver	64609	4.54

8.4. Discussions

The cost-effectiveness of seismic retrofits is significantly influenced by initial construction costs. Traditional seismic upgrade approaches using friction devices typically select connecting braces to double floor stiffness, effectively minimizing annual losses but often at considerable additional steel material expense. Alternatively, employing smaller steel HSS sections, despite slightly higher annual losses, offers a shorter payback period due to lower upfront costs. This highlights the inefficiency of the conventional approach in maximizing life-cycle benefits. Comparative analysis using NPV and BCR highlights wind design as the most advantageous solution. However, it is essential to recognize that directly correlating code-prescribed wind forces with earthquake resistance is impractical due to fundamentally different physical natures and underlying design philosophies (Nordenson, 1989). The base shear derived from the wind design can be compared to that of the seismic design. For instance, assuming $R_d R_o = 5.5$, a design wind base shear of approximately 340 kN is roughly equivalent to seismic base shears of 5% in 50 years in Montreal and 20% in 50 years in Vancouver. This observation underscores that seismic retrofit designs aimed at maximizing life-cycle benefits may not optimally align with the current code's earthquake resistance design target of 2% in 50 years. Exploring alternative design levels, such as 10% in 50 years seismic hazard, could offer valuable insights into these effects.

Chapter 9. Conclusions

This study assesses the economic benefits of seismically retrofitting steel frames in Canada using friction devices. Following the proposed displacement-based retrofit design, the PBEE framework is employed and extended to conduct a comprehensive LCCB analysis on retrofitting representative frames in both eastern and western Canada. The study further evaluates the initial retrofit costs and seismic life-cycle costs across various design scenarios. The main findings and conclusions are as follows:

1. Buildings in western Canada experience higher seismic losses compared to those in the eastern region due to higher seismicity. The percentage reduction in annual seismic losses is similar between the two regions under typical seismic retrofits with $R_d R_o = 5.5$ and $SR = 2.0$.

2. Displacement-based design strategies for seismic upgrades effectively mitigate the seismic risks of the benchmark buildings. However, they may not always offer the most economical solution.

3. Friction devices demonstrate superior performance in controlling seismic responses compared to concentric braces when utilizing the same design parameters. However, the higher initial costs associated with friction devices diminish their advantage when considering life-cycle benefits. Ultimately, both friction devices and concentric braces achieve comparable levels of life-cycle benefits under seismic designs.

4. Acceleration-related seismic losses contribute a higher percentage to the total annual seismic losses for retrofitted structures compared to original structures. This underscores the importance of controlling acceleration responses in frames to further reduce seismic losses.

5. The benefit of seismic retrofit is closely related to the initial construction costs. It is found that the designs against wind loads, adopting the least amount of steel material and lowest costs among design options, offer the most economic retrofit solutions.

This thesis exclusively examined steel MRFs. Potential future work includes extending the presented LCCB framework to other structural types such as reinforced concrete frames, shear walls, and wood frames. Additionally, while this thesis concentrated on seismic assessment in Montreal and Vancouver, future studies could explore other seismic zones in Canada using a similar approach. The six-story steel MRF analyzed in this study is a medium-height building where the response is primarily governed by the first mode. However, for taller buildings, higher modes become more significant. Therefore, it is recommended to investigate buildings of varying heights and configurations to gain insights into the cost-effectiveness of seismic retrofitting using friction dampers across different building profiles. Finally, this thesis adopts the current code's earthquake level of 2% in 50 years for retrofit design. However, it is recommended to explore other design levels of earthquake loads for a more comprehensive analysis of life-cycle cost-benefits for seismic retrofits.

Reference

Ahdi, S. K., Ancheta, T. D., Contreras, V., Kishida, T., Kwak, D. Y., Kwok, A. O., Parker, G. A., Bozorgnia, Y., & Stewart, J. P. (2017). NGA-SUBDUCTION SITE DATABASE. *16th World Conference on Earthquake Engineering*. http://www.eq.

Aiken, L. D., Kelly, J. M., & Pall, A. S. (1988). *SEISMIC RESPONSE OF A NINE-STORY STEEL FRAME WITH FRICTION DAMPED CROSS-BRACING*.

Almajhali, K. Y. M. (2023). Review on passive energy dissipation devices and techniques of installation for high rise building structures. *Structures*, *51*, 1019–1029. https://doi.org/10.1016/j.istruc.2023.03.025

Anastasiadis, A. (2024). Behavior of steel building structures subjected to strong and benchmark seismic actions: An overview of damage from the observations of the last 40 years. *Engineering Seismology and Earthquake Engineering*, *1*(6).

Ancheta, T. D., Darragh, R. B., Stewart, J. P., Seyhan, E., Silva, W. J., Chiou, B. S. J., Wooddell, K. E., Graves, R. W., Kottke, A. R., Boore, D. M., Kishida, T., & Donahue, J. L. (2014). NGA-West2 Database. *Earthquake Spectra*, *30*(3), 989–1005. https://doi.org/10.1193/070913EQS197M

Anderson, D., DeVall, R., Loeffler, R., & Ventura, C. (1999). *PRELIMINARY "GUIDELINES" FOR THE NON-LINEAR ANALYSIS AND DESIGN OF HYSTERETIC (DISPLACEMENT DEPENDENT) ENERGY DISSIPATION DEVICES IN BUILDINGS*.

Annan, C. D., Youssef, M. A., El Naggar, M. H., & Candidate, P. D. (2008). Assessment of Overstrength and Ductility of a Four-story Modular Steel Building Braced frame. *2nd Canadian Conference on Effective Design of Structures*.

Applications - Quaketek | Earthquake protection. (n.d.). Retrieved June 17, 2024, from https://quaketek.com/applications/

Applied Technology Council. (2017). *Guidelines for nonlinear structural analysis and design of buildings. part IIa - steel moment frames*. https://doi.org/10.6028/NIST.GCR.17-917-46v2

Armali, M., Damerji, H., Hallal, J., & Fakih, M. (2019). Effectiveness of friction dampers on the seismic behavior of high rise building VS shear wall system. *Engineering Reports*, *1*(5). https://doi.org/10.1002/eng2.12075

ATC-40, Seismic Evaluation and Retrofit of Concrete Buildings. (1996).

Atkinson, G. M. (2009). Earthquake Time Histories Compatible with the 2005 National Building Code of Canada Uniform Hazard Spectrum. *Canadian Journal of Civil Engineering*, *36*(6), 991–1000. https://doi.org/10.1139/L09-044

Atkinson, G. M., & Boore, D. M. (2006). Earthquake ground-motion prediction equations for eastern North America. *Bulletin of the Seismological Society of America*, *96*(6), 2181–2205. https://doi.org/10.1785/0120050245

Avtar Pall, & Rashmi Pall. (1996). Friction-dampers for Seismic Control of Buildings "A Canadian Experience." *11th World Conference on Earthquake Engineering*.

Aye, S. M., Kyaw, D. R., & Aung, M. (2014). *Comparative Study on Seismic Response of RC Structure Using Viscous Dampers and Viscoelastic Dampers*. www.semargroup.org,

Baker, J. W. (2011). Conditional Mean Spectrum: Tool for Ground-Motion Selection. *Journal of Structural Engineering*, *137*(3), 322–331. https://doi.org/10.1061/(asce)st.1943-541x.0000215

Baker, J. W., & Cornell, C. A. (2005). A vector-valued ground motion intensity measure consisting of spectral acceleration and epsilon. *Earthquake Engineering and Structural Dynamics*, *34*(10), 1193–1217. https://doi.org/10.1002/eqe.474

Baker, J. W., & Cornell, C. A. (2008). Uncertainty propagation in probabilistic seismic loss estimation. *Structural Safety*, *30*(3), 236–252. https://doi.org/10.1016/j.strusafe.2006.11.003

Balazadeh-Minouei, Y., Koboevic, S., & Tremblay, R. (2018). Seismic Assessment of Existing Steel Chevron Braced Frames. *Journal of Structural Engineering*, *144*(6). https://doi.org/10.1061/(asce)st.1943-541x.0002037

Biddah, A., & Heidebrecht, A. (1998). Seismic Performance of Moment- Resisting Steel Frame Structures Designed for Different Levels of Seismic Hazard. *Earthquake Spectra*, *14*(4).

Biddah, A., & Heidebrecht, A. C. (1999). Evaluation of the seismic level of protection afforded to steel moment resisting frame structures designed for different design philosophies. *Canadian Journal of Civil Engineering*, *26*, 35–54.

Boore, D. M., Stewart, J. P., Eeri, M., Seyhan, E., Atkinson, G. M., & Eeri, M. (2014). *NGA-West 2 Equations for Predicting PGA, PGV, and 5%-Damped PSA for Shallow Crustal Earthquakes*. http://peer.berkeley.edu

Bradley, B. A., Dhakal, R. P., Cubrinovski, M., Macrae, G. A., & Lee, D. S. (2009). SEISMIC LOSS ESTIMATION FOR EFFICIENT DECISION MAKING. *New Zealand Society for Earthquake Engineering (NZSEE) Conference*.

Bradley, B. A., Dhakal, R. P., Cubrinovski, M., Mander, J. B., & MacRae, G. A. (2007). Improved seismic hazard model with application to probabilistic seismic demand analysis. *Earthquake Engineering and Structural Dynamics*, *36*(14), 2211–2225. https://doi.org/10.1002/eqe.727

Bruneau, M., Engelhardt, M., Filiatrault, A., Goel, S. C., Itani, A., Hajjar, J., Leon, R., Ricles, J., Stojadinovic, B., & Uang, C. M. (2005). Review of selected recent research on US seismic design and retrofit strategies for steel structures. In *Progress in Structural Engineering and Materials* (Vol. 7, Issue 3, pp. 103–114). https://doi.org/10.1002/pse.192

Building construction price indexes, percentage change, quarterly. (n.d.). Retrieved June 17, 2024, from https://www150.statcan.gc.ca/t1/tbl1/en/tv.action?pid=1810027602

Canadian Commission on Building and Fire Codes. (2022). *National Building Code of Canada 2020*.

Carofilis, W., Perrone, D., O'Reilly, G. J., Monteiro, R., & Filiatrault, A. (2020). Seismic retrofit of existing school buildings in Italy: Performance evaluation and loss estimation. *Engineering Structures*, *225*. https://doi.org/10.1016/j.engstruct.2020.111243

Choun, Y. S., & Elnashai, A. S. (2010). A simplified framework for probabilistic earthquake loss estimation. *Probabilistic Engineering Mechanics*, *25*(4), 355–364. https://doi.org/10.1016/j.probengmech.2010.04.001

Commercial rents services price index, monthly. (n.d.). Retrieved June 17, 2024, from https://www150.statcan.gc.ca/t1/tbl1/en/tv.action?pid=1810025501

Constantinou, M. C., Whittaker, A. S., Kalpakidis, Y., Fenz, D. M., & Warn, G. P. (2007). *Performance of Seismic Isolation Hardware under Service and Seismic Loading*. http://mceer.buffalo.edu

Consumer Price Index, monthly, not seasonally adjusted. (n.d.). Retrieved June 17, 2024, from https://www150.statcan.gc.ca/t1/tbl1/en/tv.action?pid=1810000401

Crowley, H., Bommer, J. J., Pinho, R., & Bird, J. (2005). The impact of epistemic uncertainty on an earthquake loss model. *Earthquake Engineering and Structural Dynamics*, *34*(14), 1653–1685. https://doi.org/10.1002/eqe.498

Cutfield, M., Ryan, K., & Ma, Q. (2016). Comparative life cycle analysis of conventional and base-isolated buildings. *Earthquake Spectra*, *32*(1), 323–343. https://doi.org/10.1193/032414EQS040M

De Domenico, D., & Ricciardi, G. (2019). Earthquake protection of structures with nonlinear viscous dampers optimized through an energy-based stochastic approach. *Engineering Structures*, *179*, 523–539. https://doi.org/10.1016/j.engstruct.2018.09.076

De Domenico, D., Ricciardi, G., & Takewaki, I. (2019). Design strategies of viscous dampers for seismic protection of building structures: A review. In *Soil Dynamics and Earthquake Engineering* (Vol. 118, pp. 144–165). Elsevier Ltd. https://doi.org/10.1016/j.soildyn.2018.12.024

Deierlein, G., Andrei M, R., & Michael R, W. (2010). *Nonlinear Structural Analysis For Seismic Design A Guide for Practicing Engineers*. www.curee.org

Dong, Y., & Frangopol, D. M. (2016). Performance-based seismic assessment of conventional and base-isolated steel buildings including environmental impact and resilience. *Earthquake Engineering and Structural Dynamics*, *45*(5), 739–756. https://doi.org/10.1002/eqe.2682

Dyanati, M., Huang, Q., & Roke, D. (2017). Cost-benefit evaluation of self-centring concentrically braced frames considering uncertainties. *Structure and Infrastructure Engineering*, *13*(5), 537–553. https://doi.org/10.1080/15732479.2016.1173070

Eads, L., Miranda, E., & Lignos, D. G. (2015). Average spectral acceleration as an intensity measure for collapse risk assessment. *Earthquake Engineering and Structural Dynamics*, *44*(12), 2057–2073. https://doi.org/10.1002/eqe.2575

Earthquake Canada. (n.d.). *Seismic zones in Western Canada*. Retrieved June 17, 2024, from https://www.earthquakescanada.nrcan.gc.ca/zones/westcan-en.php

Earthquake Canada. (2021). *2020 National Building Code of Canada Seismic Hazard Tool*.

Egbelakin, T., Wilkinson, S., & Ingham, J. (2014). Economic impediments to successful seismic retrofitting decisions. *Structural Survey*, *32*(5), 449–466. https://doi.org/10.1108/SS-01-2014-0002

Egbelakin, T., Wilkinson, S., Potangaroa, R., & Ingham, J. (2011). Challenges to successful seismic retrofit implementation: A socio-behavioural perspective. *Building Research and Information*, *39*(3), 286–300. https://doi.org/10.1080/09613218.2011.552264

Fang, C., Ping, Y., Zheng, Y., & Chen, Y. (2021). Probabilistic economic seismic loss estimation of steel braced frames incorporating emerging self-centering technologies. *Engineering Structures*, *241*. https://doi.org/10.1016/j.engstruct.2021.112486

Federal Emergency Management Agency (FEMA). (2012). *Hazus ®-MH 2.1 Technical Manual*. www.msc.fema.gov

Federal Emergency Management Agency (FEMA). (2022). *Hazus Earthquake Model Technical Manual*. https://www.fema.gov/sites/default/files/documents/fema_hazus-earthquake-model-technical-manual-5-1.pdf

FEMA-273 NEHRP Guidelines for the Seismic Rehabilitation of Buildings. (1997).

FEMA-356, Prestandard and Commentary for the Seismic Rehabilitation of Buildings. (2000).

Filiatrault, A., & Cherry, S. (1987). Experimental Studies of Friction Damped Braced Steel Frames. *5th Canadian Conference of Earthquake Engineering*.

Filiatrault, A., & Cherry, S. (1990). SEISMIC DESIGN SPECTRA FOR FRICTION-DAMPED STRUCTURES. *Journal of Structural Engineering*, *116*(5).

Freddi, F., Ghosh, J., Raghunandan, M., & Kotoky, N. (2020). SEISMIC LIFE-CYCLE COST-BENEFIT ANALYSIS OF BRBs RETROFITTED FRAME. *17th World Conference on Earthquake Engineering*.

Fung, J. F., Zhang, Y., Johnson, K. J., Cook, D., & Sattar, S. (2022). *A framework to evaluate the cost-effectiveness of recovery-based design*. https://doi.org/10.6028/NIST.SP.1277

Gasim, B., & Lakshmi, T. V. S. V. (2016). Effect of Discontinuous Load Path on Seismic Performance of Building Using SAP2000. *International Journal of Scientific Engineering and Technology Research*. www.ijsetr.com

Geschwindner, L. F., & Disque, R. O. (2005). Flexible Moment Connections for Unbraced Frames Subject to Lateral Forces-A Return to Simplicity. *Engineering Journal*, *42*.

Ghasemof, A., Mirtaheri, M., Karami Mohammadi, R., & Mashayekhi, M. R. (2021). Multi-objective optimal design of steel MRF buildings based on life-cycle cost using a swift algorithm. *Structures*, *34*, 4041–4059. https://doi.org/10.1016/j.istruc.2021.09.088

Gibson, J. D. (1954). Post-War Economic Development and Policy in Canada. *Canadian Journal of Economics and Political Science*, *20*(4), 439–455. https://doi.org/10.2307/138554

Gómez, L. V. D. (2014). *Seismic Fragility Analysis of Steel Moment-Resisting Frames (MRF) Designed in Canada in the*.

Gómez, L. V. D., Kwon, O. S., & Dabirvaziri, M. R. (2015). Seismic fragility of steel moment-resisting frames in vancouver and montreal designed in the 1960s, 1980s, and 2010. *Canadian Journal of Civil Engineering*, *42*(11), 919–929. https://doi.org/10.1139/cjce-2014-0492

Günay, S., & Mosalam, K. M. (2013). PEER performance-based earthquake engineering methodology, revisited. *Journal of Earthquake Engineering*, *17*(6), 829–858. https://doi.org/10.1080/13632469.2013.787377

Halchuk, S., Adams, J., Kolaj, M., & Allen, T. (2019). Deaggregation of NBCC 2015 Seismic Hazard for Selected Canadian Cities. *12th Canadian Conference on Earthquake Engineering*.

Hamburger, R. O., & Malley, J. O. (2019, February). Welded Steel Moment Resisting Frames The Earthquake-Resisting System that Surprised the Profession. *Structurer Magazine*. www.STRUCTUREmag.org.

Harrington, C. C., & Liel, A. B. (2021). Indicators of improvements in seismic performance possible through retrofit of reinforced concrete frame buildings. *Earthquake Spectra*, *37*(1), 262–283. https://doi.org/10.1177/8755293020936707

Historical statistics of Canada: Section R: Manufactures. (n.d.). Retrieved June 17, 2024, from https://www150.statcan.gc.ca/n1/pub/11-516-x/sectionr/4147443-eng.htm

Historical statistics of Canada: Section S: Construction and Housing. (n.d.). Retrieved June 17, 2024, from https://www150.statcan.gc.ca/n1/pub/11-516-x/sections/4057757-eng.htm

Hodgson, E. (1946). British Columbia Earthquake. *The Journal of The Royal Astronomical Society of Canada*, *8*.

Horwich, G. (2000). Economic Lessons of the Kobe Earthquake*. *Economic Development and Cultural Change*, *48*(3).

Hutt, C., Almufti, I., Willford, M., & Deierlein, G. (2016). Seismic Loss and Downtime Assessment of Existing Tall Steel-Framed Buildings and Strategies for Increased Resilience. *Journal of Structural Engineering*, *142*(8). https://doi.org/10.1061/(asce)st.1943-541x.0001314

Ibarra, L. F., Medina, R. A., & Krawinkler, H. (2005). Hysteretic models that incorporate strength and stiffness deterioration. *Earthquake Engineering and Structural Dynamics*, *34*(12), 1489–1511. https://doi.org/10.1002/eqe.495

Jaaz, H. A. G., Naser, A. F., Mohammed, H. A., & Mohammed, A. A. (2021). Earthquake Resistance Optimization and Evaluation of Bridge Piers Structural Form and Dimensions Based on Demand to Capacity Ratio and Yielding Points of Force-Displacement.

Mathematical Modelling of Engineering Problems, *8*(6), 945–954. https://doi.org/10.18280/mmep.080614

Jaisee, S., Yue, F., & Ooi, Y. H. (2021). A state-of-the-art review on passive friction dampers and their applications. In *Engineering Structures* (Vol. 235). Elsevier Ltd. https://doi.org/10.1016/j.engstruct.2021.112022

Jalayer, F., Elefante, L., De Risi, R., & Manfredi, G. (2014). CLOUD ANALYSIS REVISITED: EFFICIENT FRAGILITY CALCULATION AND UNCERTAINTY PROPAGATION USING SIMPLE LINEAR REGRESSION. *The U.S. National Conference on Earthquake Engineering*.

Javanmardi, A., Ibrahim, Z., Ghaedi, K., Benisi Ghadim, H., & Hanif, M. U. (2020). State-of-the-Art Review of Metallic Dampers: Testing, Development and Implementation. *Archives of Computational Methods in Engineering*, *27*(2), 455–478. https://doi.org/10.1007/s11831-019-09329-9

Jayaram, N., Lin, T., & Baker, J. W. (2011). A Computationally efficient ground-motion selection algorithm for matching a target response spectrum mean and variance. *Earthquake Spectra*, *27*(3), 797–815. https://doi.org/10.1193/1.3608002

Kam, W., & Jury, R. (2017). PERFORMANCE-BASED SEISMIC ASSESSMENT: SIMPLIFIED METHODS AND COLLAPSE INDICATORS. *16th World Conference on Earthquake Engineering*.

Kerboua, M., Benguediab, M., Megnounif, A., Benrahou, K. H., & Kaoulala, F. (2014). Semi active control of civil structures, analytical and numerical studies. *Physics Procedia*, *55*, 301–306. https://doi.org/10.1016/j.phpro.2014.07.044

Kircher, C. A., Robert, V., Whitman, V., & Holmes, W. T. (2006). HAZUS Earthquake Loss Estimation Methods. *Natural Hazards Review*, *7*(2). https://doi.org/10.1061/ASCE1527-698820067:245

Kolaj, M., Adams, J., & Halchuk, S. (2020a). SEISMIC HAZARD IN SOUTHEASTERN CANADA: UNCERTAINTY AND CONTROLS ON SEISMIC HAZARD IN A REGION OF LOW-TO-MODERATE SEISMICITY. *The 17th World Conference on Earthquake Engineering*.

Kolaj, M., Adams, J., & Halchuk, S. (2020b). THE 6th GENERATION SEISMIC HAZARD MODEL OF CANADA. *The 17th World Conference on Earthquake Engineering*.

Kolaj, M., Halchuk, S., & Adams, J. (2023a). *Sixth Generation seismic hazard model of Canada: final input files used to generate the 2020 National Building Code of Canada seismic hazard values*. https://doi.org/10.4095/331387

Kolaj, M., Halchuk, S., & Adams, J. (2023b). *Sixth-generation seismic hazard model of Canada: grid values of mean hazard to be used with the 2020 National Building Code of Canada*. https://doi.org/10.4095/331497

Kyriakopoulos, N. (2012). *Upgrade of Seismically Deficient Steel Frame Structures Built in Canada Between the 1960s and 1980s Using Passive Supplemental Damping*. University of Toronto.

Kyriakopoulos, N., & Christopoulos, C. (2013). Seismic assessment and upgrade of Type 2 construction steel moment-resisting frames built in Canada between the 1960s and 1980s using passive supplemental damping. *Canadian Journal of Civil Engineering*, *40*(7), 644–654. https://doi.org/10.1139/cjce-2012-0404

Lamontagne, M., Halchuk, S., Cassidy, J. F., & Rogers, G. C. (2008). Significant Canadian earthquakes of the period 1600-2006. *Seismological Research Letters*, *79*(2), 211–223. https://doi.org/10.1785/gssrl.79.2.211

Lamontagne, M., & Ranalli, G. (2012). Earthquakes and geological structures of the st. lawrence rift system. In *Intraplate Earthquakes* (pp. 72–96). Cambridge University Press. https://doi.org/10.1017/CBO9781139628921.005

Latour, M., Rizzano, G., Santiago, A., & Simões da Silva, L. (2019). Experimental response of a low-yielding, self-centering, rocking column base joint with friction dampers. *Soil Dynamics and Earthquake Engineering*, *116*, 580–592. https://doi.org/10.1016/j.soildyn.2018.10.011

Lee, S. H., Park, J. H., Lee, S. K., & Min, K. W. (2008). Allocation and slip load of friction dampers for a seismically excited building structure based on storey shear force distribution. *Engineering Structures*, *30*(4), 930–940. https://doi.org/10.1016/j.engstruct.2007.03.020

Lee, S. K., Park, J. H., Moon, B. W., Min, K. W., Lee, S. H., & Kim, J. (2008). Design of a bracing-friction damper system for seismic retrofitting. *Smart Structures and Systems*, *4*(5), 685–696. https://doi.org/10.12989/sss.2008.4.5.685

Lee, T., & Mosalam, K. (2006). *Probabilistic Seismic Evaluation of Reinforced Concrete Structural Components and Systems*.

Lignos, D. G., & Krawinkler, H. (2011). Deterioration Modeling of Steel Components in Support of Collapse Prediction of Steel Moment Frames under Earthquake Loading. *Journal of Structural Engineering*, *137*(11), 1291–1302. https://doi.org/10.1061/(asce)st.1943-541x.0000376

Lin, K., Zheng, J., Wu, Z., Lu, X., & Li, Y. (2024). Risk-based life cycle cost–benefit analysis for progressive collapse design of RC frame structures. *Structures*, *63*. https://doi.org/10.1016/j.istruc.2024.106468

Lin, T., Haselton, C. B., & Baker, J. W. (2013). Conditional spectrum-based ground motion selection. Part I: Hazard consistency for risk-based assessments. *Earthquake Engineering and Structural Dynamics*, *42*(12), 1847–1865. https://doi.org/10.1002/eqe.2301

Lu, D.-G., Yu, X.-H., Pan, F., & Wang, G.-Y. (2008). PROBABILISTIC SEISMIC DEMAND ANALYSIS CONSIDERING RANDOM SYSTEM PROPERTIES BY AN IMPROVED CLOUD METHOD. *The 14th World Conference on Earthquake Engineering*.

Massarelli, R. (2010). *DYNAMIC BEHAVIOUR AND INELASTIC PERFORMANCE OF STEEL ROOF DECK DIAPHRAGMS*. McGill University.

McKenna, F. (2011). OpenSees: A Framework for Earthquake Engineering Simulation. *Computing in Science & Engineering*, *13*(4).

Miguel, L. F. F., Fadel Miguel, L. F., & Lopez, R. H. (2015). A firefly algorithm for the design of force and placement of friction dampers for control of man-induced vibrations in footbridges. *Optimization and Engineering*, *16*(3), 633–661. https://doi.org/10.1007/s11081-014-9269-3

Miguel, L. F. F., Miguel, L. F. F., & Lopez, R. H. (2014). Robust design optimization of friction dampers for structural response control. *Structural Control and Health Monitoring*, *21*(9), 1240–1251. https://doi.org/10.1002/stc.1642

Miguel, L. F. F., Miguel, L. F. F., & Lopez, R. H. (2016a). Failure probability minimization of buildings through passive friction dampers. *Structural Design of Tall and Special Buildings*, *25*(17), 869–885. https://doi.org/10.1002/tal.1287

Miguel, L. F. F., Miguel, L. F. F., & Lopez, R. H. (2016b). Simultaneous optimization of force and placement of friction dampers under seismic loading. *Engineering Optimization*, *48*(4), 582–602. https://doi.org/10.1080/0305215X.2015.1025774

Miguel, L. F. F., Miguel, L. F. F., & Lopez, R. H. (2018). Methodology for the simultaneous optimization of location and parameters of friction dampers in the frequency domain. *Engineering Optimization*, *50*(12), 2108–2122. https://doi.org/10.1080/0305215X.2018.1428318

Miller, M. M. (2001). *The February 28, 2001 Nisqually earthquake: GPS Geodesy and quantifying seismic hazard.* http://www.geodesy.cwu.edu/

Min, K. W., Seong, J. Y., & Kim, J. (2010). Simple design procedure of a friction damper for reducing seismic responses of a single-story structure. *Engineering Structures*, *32*(11), 3539–3547. https://doi.org/10.1016/j.engstruct.2010.07.022

Minimum design loads and associated criteria for buildings and other structures. (2017). In *Minimum Design Loads and Associated Criteria for Buildings and Other Structures*. American Society of Civil Engineers (ASCE). https://doi.org/10.1061/9780784414248

Mitchell, D., Paultre, P., Tinawi, R., Saatcioglu, M., Tremblay, R., Elwood, K., Adams, J., & DeVall, R. (2010). Evolution of seismic design provisions in the National building code of Canada. *Canadian Journal of Civil Engineering*, *37*(9), 1157–1170. https://doi.org/10.1139/L10-054

Moehle, J., & Deierlein, G. (2004). A framework methodology for performance-based earthquake engineering. *13th World Conference on Earthquake Engineering*. https://www.researchgate.net/publication/228706335

Moghaddam, H., Afzalinia, F., & Hajirasouliha, I. (2022). Optimal distribution of friction dampers to improve the seismic performance of steel moment resisting frames. *Structures*, *37*, 624–644. https://doi.org/10.1016/j.istruc.2022.01.007

Moreschi, L. M., & Singh, M. P. (2003). Design of yielding metallic and friction dampers for optimal seismic performance. *Earthquake Engineering and Structural Dynamics*, *32*(8), 1291–1311. https://doi.org/10.1002/eqe.275

Nabid, N., Hajirasouliha, I., & Petkovski, M. (2018). Performance-based optimisation of RC frames with friction wall dampers using a low-cost optimisation method. *Bulletin of Earthquake Engineering*, *16*(10), 5017–5040. https://doi.org/10.1007/s10518-018-0380-2

Nakashima, M., Inoue, K., & Tada, M. (1998). Classification of damage to steel buildings observed in the 1995 Hyogoken-Nanbu earthquake. *Engineering Structures*, *20*, 271–281.

National Research Council of Canada. (1967). *NATIONAL BUILDING CODE OF CANADA 1965*.

Ning, C., & Xie, Y. (2022). Risk-Based Optimal Design of Seismic Protective Devices for a Multicomponent Bridge System Using Parameterized Annual Repair Cost Ratio. *Journal of Structural Engineering*, *148*(5). https://doi.org/10.1061/(asce)st.1943-541x.0003330

Nordenson, G. J. P. (1989). *Wind versus Seismic Design*.

NourEldin, M., Naeem, A., & Kim, J. (2019). Life-cycle cost evaluation of steel structures retrofitted with steel slit damper and shape memory alloy–based hybrid damper. *Advances in Structural Engineering*, *22*(1), 3–16. https://doi.org/10.1177/1369433218773487

Nuti, C., & Vanzi, I. (2003). To retrofit or not to retrofit? *Engineering Structures*, *25*(6), 701–711. https://doi.org/10.1016/S0141-0296(02)00190-6

Ontiveros-Pérez, S. P., Miguel, L. F. F., & Riera, J. D. (2019). Reliability-based optimum design of passive friction dampers in buildings in seismic regions. *Engineering Structures*, *190*, 276–284. https://doi.org/10.1016/j.engstruct.2019.04.021

Padgett, J. E., Dennemann, K., & Ghosh, J. (2010). Risk-based seismic life-cycle cost-benefit (LCC-B) analysis for bridge retrofit assessment. *Structural Safety*, *32*(3), 165–173. https://doi.org/10.1016/j.strusafe.2009.10.003

Padgett, J. E., Nielson, B. G., & DesRoches, R. (2008). Selection of optimal intensity measures in probabilistic seismic demand models of highway bridge portfolios. *Earthquake Engineering and Structural Dynamics*, *37*(5), 711–725. https://doi.org/10.1002/eqe.782

Padilla-Llano, D. A., Moen, C. D., & Eatherton, M. R. (2015). OpenSees simulation of steel column axial cyclic response including local buckling. *Annual Stability Conference*.

Pagani, M., Monelli, D., Weatherill, G., Danciu, L., Crowley, H., Silva, V., Henshaw, P., Butler, L., Nastasi, M., Panzeri, L., Simionato, M., & Vigano, D. (2014). Openquake engine: An open hazard (and risk) software for the global earthquake model. *Seismological Research Letters*, *85*(3), 692–702. https://doi.org/10.1785/0220130087

Pall, A. S., Marsh, C. C., & Fazio, P. (1980). Friction Joints for Seismic Control of Large Panel Structures. *PCI Journal*, *25*(6).

Parker, G. A., Stewart, J. P., Boore, D. M., Atkinson, G. M., & Hassani, B. (2022). NGA-subduction global ground motion models with regional adjustment factors. *Earthquake Spectra*, *38*(1), 456–493. https://doi.org/10.1177/87552930211034889

Pasquin, C., Leboeuf, N., Tina PALL, R., & Pall, A. (2004). FRICTION DAMPERS FOR SEISMIC REHABILITATION OF EATON'S BUILDING, MONTREAL. *13th World Conference on Earthquake Engineering*. www.palldynamics.com.

Patro, S., & Sinha, R. (2010). Seismic performance of dry-friction energy dissipation devices in shear-frame buildings. *Journal of Civil Engineering and Architecture*. https://www.researchgate.net/publication/297253918_Seismic_performance_of_dry-friction_energy_dissipation_devices_in_shear-frame_buildings

Popov, P., Yang, T.-S., & Chang, S.-P. (1998). Design of steel MRF connections before and after 1994 Northridge earthquake*. *Engineering Structures*, *20*(12), 1030–1038.

Porter, K. A. (2003). *An Overview of PEER's Performance-Based Earthquake Engineering Methodology*.

Priya, S. D., K, U. P., & Iyer, N. R. (2014). Enhancing the Seismic Response of Buildings with Energy Dissipation Methods-An Overview. *Journal of Civil Engineering Research*, *2014*(2A), 17–22. https://doi.org/10.5923/c.jce.201401.04

Reis, E., & Bonowitz, D. (2000). *SAC Joint Venture: State of the Art Report on Past Performance of Steel Moment-Frame Buildings in Earthquakes*.

Roeder, C. (2000). *SAC Joint Venture: State of the Art Report on Connection Performance*.

Rogers, G., Halchuk, S., Adams, J., & Allen, T. (2015). 5 TH GENERATION (2015) SEISMIC HAZARD MODEL FOR SOUTHWEST BRITISH COLUMBIA. *The 11th Canadian Conference on Earthquake Engineering*.

Roh, J. E., Hur, M. W., Choi, H. H., & Lee, S. H. (2018). Development of a Multiaction Hybrid Damper for Passive Energy Dissipation. *Shock and Vibration*, *2018*. https://doi.org/10.1155/2018/5630746

Ross, A. E. (1995). The Northridge Earthquake Steel Moment Frame Failures: Results of Phase One of the S.A.C. Joint Venture Research Program. *7th Canadian Conference on Earthquake Engineering*.

SAC Joint Venture. (1997). *Protocol for Fabrication, Inspection, Testing, and Documentation of Beam-Column Connection Tests and Other Experimental Specimens.*

Sarno, L. DI, & Elnashai, A. S. (2004). BRACING SYSTEMS FOR SEISMIC RETROFITTING OF STEEL FRAMES. *13th World Conference on Earthquake Engineering*.

Shen, J., Seker, O., Akbas, B., Seker, P., Momenzadeh, S., & Faytarouni, M. (2017). Seismic performance of concentrically braced frames with and without brace buckling. *Engineering Structures*, *141*, 461–481. https://doi.org/10.1016/j.engstruct.2017.03.043

Shu, Z., You, R., & Zhou, Y. (2022). Viscoelastic Materials for Structural Dampers: A Review. In *Construction and Building Materials* (Vol. 342). Elsevier Ltd. https://doi.org/10.1016/j.conbuildmat.2022.127955

Solberg, C., Rossetto, T., & Joffe, H. (2010). The social psychology of seismic hazard adjustment: Re-evaluating the international literature. *Natural Hazards and Earth System Science*, *10*(8), 1663–1677. https://doi.org/10.5194/nhess-10-1663-2010

Soong, T. T., & Spencer, B. F. (2002). Supplemental energy dissipation: state-of-the-art and state-of-the-practice. In *Engineering Structures* (Vol. 24). www.elsevier.com/locate/engstruct

Spence, R., & Coburn, A. (2008). *Earthquake Risk and Insurance. In: Assessing and Managing Earthquake Risk. Geotechnical, Geological And Earthquake Engineering, vol 2* (C. S. Oliveira, A. ROCA, & X. Goula, Eds.). Springer.

Symans, M. D., Charney, F. A., Whittaker, A. S., Constantinou, M. C., Kircher, C. A., Johnson, M. W., & Mcnamara, R. J. (2008). Energy Dissipation Systems for Seismic Applications: Current Practice and Recent Developments. *Journal of Structural Engineering*, *134*(1). https://doi.org/10.1061/ASCE0733-94452008134:13

Taiyari, F., Mazzolani, F. M., & Bagheri, S. (2019). Damage-based optimal design of friction dampers in multistory chevron braced steel frames. *Soil Dynamics and Earthquake Engineering*, *119*, 11–20. https://doi.org/10.1016/j.soildyn.2019.01.004

Tesfamariam, S., & Saatcioglu, M. (2008). Risk-based seismic evaluation of reinforced concrete buildings. *Earthquake Spectra*, *24*(3), 795–821. https://doi.org/10.1193/1.2952767

Thorsen, G. (1986). *THE PUGET LOWLAND EARTHQUAKES OF 1949 AND 1965 REPRODUCTIONS OF SELECTED ARTICLES DESCRIBING DAMAGE*.

Tierney, K. J. (1997). Business impacts of the Northridge earthquake. *Journal of Contingencies and Crisis Management*, *5*(2), 87–97. https://doi.org/10.1111/1468-5973.00040

Tremblay, A., Long, B., & Massé, M. (2003). Supracrustal faults of the St. Lawrence rift system, Québec: Kinematics and geometry as revealed by field mapping and marine seismic reflection data. *Tectonophysics*, *369*(3–4), 231–252. https://doi.org/10.1016/S0040-1951(03)00227-0

Tremblay, R. (2015). Advances in Seismic Evaluation and Retrofit of Steel Building Structures under the Canadian Seismic Research Network. *The 11th Canadian Conference on Earthquake Engineering*.

Tremblay, R., Bruneau, M., Nakashima, M., Prion, H. G. L., Filiatrault, A., & Devall, R. (1996). Seismic design of steel buildings: lessons from the 1995 Hyogo-ken Nanbu earthquake. *Canadian Journal of Civil Engineering*, *23*(3).

Tremblay, R., Timler, P., Bruneau, M., & Filiatrault, A. (1995). Performance of steel structures during the 1994 Northridge earthquake. *Canadian Journal of Civil Engineering*, *22*.

Tsai, K. C., Wu, S., & Popov, E. P. (1995). EXPERIMENTAL PERFORMANCE OF SEISMIC STEEL BEAM-COLUMN MOMENT JOINTS. *Journal of Structural Engineering*, *121*(6).

Uribe, R., Sattar, S., Speicher, M. S., & Ibarra, L. (2018). *Impact of ground motion selection methods on the seismic assessment of steel special moment frames*. https://doi.org/10.6028/NIST.TN.1992

Veismoradi, S., Yousef-beik, S. M. M., Zarnani, P., & Quenneville, P. (2021). Development and parametric study of a new self-centering rotational friction damper. *Engineering Structures*, *235*. https://doi.org/10.1016/j.engstruct.2021.112097

Vitiello, U., Asprone, D., Di Ludovico, M., & Prota, A. (2017). Life-cycle cost optimization of the seismic retrofit of existing RC structures. *Bulletin of Earthquake Engineering*, *15*(5), 2245–2271. https://doi.org/10.1007/s10518-016-0046-x

Wang, P. (2012). *Rupture Models of the Great 1700 Cascadia Earthquake Based on Microfossil Paleoseismic Observations*. University of Victoria.

Wang, Y., Zhou, Z., Xie, Q., & Huang, L. (2020). Theoretical analysis and experimental investigation of hysteretic performance of self-centering variable friction damper braces. *Engineering Structures*, *217*. https://doi.org/10.1016/j.engstruct.2020.110779

Weber, F., Høgsberg, J., & Krenk, S. (2010). Optimal Tuning of Amplitude Proportional Coulomb Friction Damper for Maximum Cable Damping. *Journal of Structural Engineering*, *136*(2). https://doi.org/10.1061/ASCE0733-94452010136:2123

Westenenk, B., Edwards, J. J., de la Llera, J. C., & Jünemann, R. (2019). Self-Centering Frictional Damper (SCFD). *Engineering Structures*, *197*. https://doi.org/10.1016/j.engstruct.2019.109425

Whittle, J., Williams, M. S., & Blakeborough, A. (2010). PRELIMINARY STUDY OF OPTIMAL PLACEMENT OF VISCOUS DAMPERS IN BUILDINGS. *Canadian Conference on Earthquake Engineering*.

William McGuire. (1988). Introduction. *Journal of Construction Steel Research*, *10*.

Xie, Y., & Zhang, J. (2017). Optimal Design of Seismic Protective Devices for Highway Bridges Using Performance-Based Methodology and Multiobjective Genetic Optimization. *Journal of Bridge Engineering*, *22*(3). https://doi.org/10.1061/(asce)be.1943-5592.0001009

Xu, L. H., Xie, X. S., & Li, Z. X. (2018). Development and experimental study of a self-centering variable damping energy dissipation brace. *Engineering Structures*, *160*, 270–280. https://doi.org/10.1016/j.engstruct.2018.01.051

Yan, J., & Tremblay, R. (2012). *Seismic assessment of deficient steel braced frames with built-up back-to-back double angle brace sections using OpenSees modelling*.

Zhang, R., Wang, W., & Alam, M. S. (2022). Seismic evaluation of friction spring-based self-centering braced frames based on life-cycle cost. *Earthquake Engineering and Structural Dynamics*. https://doi.org/10.1002/eqe.3728

Zhang, Y., Fung, J. F., Cook, D., Johnson, K. J., & Sattar, S. (2024). Benefit–Cost Analysis for Earthquake-Resilient Building Design and Retrofit: State of the Art and Future Research Needs. *Natural Hazards Review*, *25*(3). https://doi.org/10.1061/NHREFO.NHENG-1910

Zhu, S., & Zhang, Y. (2008). Seismic Analysis of Concentrically Braced Frame Systems with Self-Centering Friction Damping Braces. *Journal of Structural Engineering*, *134*(1). https://doi.org/10.1061/ASCE0733-94452008134:1121

Appendix A. Seismic Retrofit Design of the Friction Damper-Bracing System and Concentric Braces

Table A-9-1 Importance factors in NBCC 2020

Importance Category	Importance Factor	
	ULS	SLS
Low	0.8	0.9
Normal	1	0.9
High	1.15	0.9
Post-disaster	1.25	0.9

To prevent unexpected slippage, the slip loads of the friction damper must be at least 115% of the wind loads. Therefore, calculating the wind loads is the initial step. According to the NBCC 2020, the wind pressures are 0.44 kPa for Montreal and 0.45 kPa for Vancouver. The wind loads are determined as follows:

$$P = I_W q C_e C_t C_g C_p \qquad A-1$$

where I_W is the importance factor (Table A-9-1), q is the reference velocity pressure, C_e is the exposure factor, C_t is the topographic factor, C_g is the gust effect factor, and C_p is the external pressure coefficient. The exposure factor, C_e, is determined based on the reference height h, which is the building height in the windward direction and the mid-height in the leeward directions. As such, the windward and leeward exposure factors are calculated as follows:

$$C_{ew} = 0.7\left(\frac{h}{12}\right)^{0.3} = 0.7\left(\frac{22.5}{12}\right)^{0.3} = 0.845 \qquad A-2$$

$$C_{el} = 0.7\left(\frac{h}{12}\right)^{0.3} = 0.7\left(\frac{\frac{22.5}{2}}{12}\right)^{0.3} = 0.687\ (not\ less\ than\ 0.7) \qquad A-3$$

The topographic factor, C_g, is taken as 1.0 for the building located on a flat surface, and the gust effect is taken as 2.0 for the building as a whole and main structural members. In determining the wind load of the lateral force resisting system, the C_p value is determined based on the value of H/D, where H represents the building's height and D denotes the width of the building parallel to the direction of the wind.

$$0.25 \leq H/D = \frac{22.5}{24} < 1.0 \qquad A-4$$

The windward and leeward external pressure coefficients subsequently are calculated as follows:

$$C_{pw} = 0.27(H/D + 2) = 0.793 \qquad A-5$$

$$C_{pl} = -0.27(H/D + 0.88) = -0.491 \qquad A-6$$

The wind loads in Montreal, for example, can then be computed:

$$P_w = 1.0 \times 0.44kPa \times 0.845 \times 1.0 \times 2.0 \times 0.793 = 0.59kPa$$

$$P_l = 1.0 \times 0.44kPa \times 0.7 \times 1.0 \times 2.0 \times -0.491 = -0.30kPa$$

The wind loads, wind shear loads, and minimum seismic brace capacity are shown in Table A-9-2

Table A-9-2 Wind loads and minimum seismic brace capacity requirements

City	Level	Wind Force (kN)	Wind Shear (kN)	115% Wind Shear (kN)	Seismic Brace Force (kN)
Montreal	6	26	26	29	32
	5	51	77	88	97
	4	51	128	147	162
	3	51	179	206	226
	2	51	231	265	291
	1	58	288	332	381
Vancouver	6	26	26	30	33
	5	52	79	90	99
	4	52	131	151	165
	3	52	183	211	232
	2	52	236	271	298
	1	59	295	339	389

The connecting steel braces are subsequently selected. They consist of steel HSS sections and are selected based on SR, an example of selection with $SR = 2$ in Vancouver is shown in Table A-9-3.

Table A-9-3 Selection of steel HSS sections based on stiffness for Vancouver structures

Level	HSS Section	Brace Lateral Stiffness (kN/m)	Floor Lateral Stiffness (kN/m)	Ratio
6	177.8 × 177.8 × 6.4	82399	38109	2.16
5	177.8 × 177.8 × 6.4	82399	32711	2.52
4	355.6 × 355.6 × 12.7	330011	152101	2.17
3	355.6 × 355.6 × 12.7	330011	124954	2.64
2	457.2 × 457.2 × 15.9	554169	276613	2.00
1	355.6 × 355.6 × 9.5	229731	104725	2.19

After selecting the HSS sections, their ability to withstand previously calculated wind loads must be verified. For instance, the capacity of the HSS section 177.8×177.8 × 6.4 adopted in the top two levels is calculated using the Equation $A - 7$ to $A - 11$.

Elastic Local Buckling Limit

$$\frac{b-4t}{t} \leq \frac{670}{\sqrt{F_y}} \qquad A-7$$

$$\frac{b-4t}{t} = \frac{177.8 - 4 \times 5.9}{5.9} = 26.1356 \leq \frac{670}{\sqrt{F_y}} = \frac{670}{\sqrt{345}} = 36.072$$

Slenderness Limit

$$\frac{kL}{r} = \frac{1.0 \times 8780}{69.8} = 125.7879 < 200 \qquad A-8$$

Determine λ

$$\frac{kL}{r}\sqrt{\frac{F_y}{\pi^2 E}} = 125.7879\sqrt{\frac{345}{\pi^2 200000}} = 1.6630 \qquad A-9$$

Determine C_r

$$C_r = \emptyset A F_y (1 + \lambda^{2n})^{-\frac{1}{n}} = 376kN \qquad A-10$$

Determine T_r

$$T_r = \phi A_g F_y = 1232kN \qquad A-11$$

The calculated compression capacity, C_r, will limit the maximum allowable slip loads of the friction damper. The slip loads of the friction dampers, adjusted for wind loads and brace capacities, are shown in Table A-9-4.

Table A-9-4 Slip loads of friction dampers in Vancouver structures

Friction Damper Slip Loads (kN)					
Level	$R_d R_o$				
	$\mathbf{2.6}$	$\mathbf{5.5}$	$\mathbf{7.5}$	$\mathbf{10}$	$\mathbf{12}$
6	370	340	250	190	160
5	370	370	370	340	280
4	1750	830	610	460	380
3	2070	980	720	530	450
2	2380	1130	830	620	520
4	2450	1160	850	640	530

To adopt concentric braces as an alternative solution to friction dampers, the HSS sections are selected based on the linear elastic seismic brace forces obtained from the pushover analysis, as illustrated in Table A-9-5. These linear elastic seismic forces are also utilized to determine the slip loads for the friction devices. Essentially, the concentric braces are chosen to match the capacity required for the slip loads of the friction dampers.

Table A-9-5 Selected HSS concentric brace sections when $R_d R_o = 5.5$

Level	Seismic Brace Force (kN)	HSS Section	Compression Capacity (kN)
6	340	177.8 × 177.8 × 6.4	376
5	610	203.2 × 203.2 × 7.9	652
4	830	228.6 × 228.6 × 7.9	879
3	980	228.6 × 228.6 × 9.5	1034
5	1130	254.0 × 254.0 × 7.9	1125
1	1160	254.0 × 254.0 × 9.5	1258